

BROKEN ROTATIONAL SYMMETRY IN
IRON BASED SUPERCONDUCTORS

A DISSERTATION
SUBMITTED TO THE DEPARTMENT OF APPLIED PHYSICS
AND THE COMMITTEE ON GRADUATE STUDIES
OF STANFORD UNIVERSITY
IN PARTIAL FULFILLMENT OF THE REQUIREMENTS
FOR THE DEGREE OF
DOCTOR OF PHILOSOPHY

Jiun-Haw Chu

March 2012

© 2012 by Jiun-Haw Chu. All Rights Reserved.

Re-distributed by Stanford University under license with the author.



This work is licensed under a Creative Commons Attribution-Noncommercial 3.0 United States License.

<http://creativecommons.org/licenses/by-nc/3.0/us/>

This dissertation is online at: <http://purl.stanford.edu/vm701mj2739>

I certify that I have read this dissertation and that, in my opinion, it is fully adequate in scope and quality as a dissertation for the degree of Doctor of Philosophy.

Ian Fisher, Primary Adviser

I certify that I have read this dissertation and that, in my opinion, it is fully adequate in scope and quality as a dissertation for the degree of Doctor of Philosophy.

Steven Kivelson

I certify that I have read this dissertation and that, in my opinion, it is fully adequate in scope and quality as a dissertation for the degree of Doctor of Philosophy.

Zhi-Xun Shen

Approved for the Stanford University Committee on Graduate Studies.

Patricia J. Gumport, Vice Provost Graduate Education

This signature page was generated electronically upon submission of this dissertation in electronic format. An original signed hard copy of the signature page is on file in University Archives.

Abstract

High-temperature superconductivity often emerges in the proximity of a symmetry-breaking ground state in strongly interacting electronic materials. In the case of the superconducting iron pnictides, in addition to the antiferromagnetic ground state of the parent compounds, a ubiquitous but small structural distortion breaks the crystal C_4 rotational symmetry in the underdoped part of the phase diagram. It has been proposed that this structural transition is driven by an electronic nematic phase transition, below which the electronic system spontaneously organizes with an orientational order without developing additional spatial periodic order. In this thesis I show how the effects of this electronic nematic order can be explicitly revealed by observing the response of the system to in-plane uniaxial stress.

I present transport measurements of single crystal samples of various iron-based superconductors held under an in-situ tunable strain at temperatures above the phase transition, which explicitly confirm that the structural transition is fundamentally driven by a thermodynamic instability in the electronic part of the free energy. I will also discuss the nematic fluctuations prevailing throughout the overdoped part of the phase diagram, which suggests that a quantum phase transition occurs at the optimal doped composition. Finally, I will describe the in-plane resistivity anisotropy measurements of detwinned samples at temperatures below phase transition, which potentially reveals an intriguing interplay between topological protected Dirac pockets and spin/orbital ordering.

Acknowledgements

I would like to express my sincere gratitude to people for helping and supporting me during my PhD study.

First I would like to thank my advisor, Ian Fisher, for his patience and kindness. From him I learned how to discover excitement and fun in every aspect of research, and how to approach the problem in a creative way. He is a great role model to me in academic career. I will always remember the exciting discussions we had.

I would also like to thank the members of my thesis defense committee: Tom Devereaux, Steven Kivelson, Kathryn Moler and Zhi-Xun Shen. I learned so much from them; not only from their insightful comments but also from our collaboration and discussion in the past few years.

James (Jim) Analytis and I first met in High Magnet Field Lab, Nijmegen. Although the results of that experiment never got published, we began our beautiful friendship and collaboration. We spent so many hours/days in Stanford and high field labs around the world, doing the most exciting experiments on the most exotic materials. It has been a pleasure and honor to work with Jim.

The Fisher group members are wonderful. Nancy handed me my first project, rare earth tri-telluride, and taught me almost all the basic experiment skills. Eric is always the first person I go to when I have questions. Ann has grown the first single crystal of iron pnictides, which was a great start for Jim and I to follow. Hsueh-Hui joined the lab after me, and we worked closely on many iron pnictides projects. Scott was initially our best user support at high field lab, and then became a member of Fisher group. Chris was the undergrad student I worked with, he has been always enthusiastic about the experiments. K-Yun, Felipe, Max, Paula, Hanoh are all very

fun to work with. We had so many good time in conferences, baseball game, ski trip, and perhaps filling liquid helium and nitrogen.

I want to thank my friends and colleagues in GLAM. We navigate through the storms of iron pnictides and topological insulators as a team. I thank Ming, Donghui, Yulin and Wei-Sheng from ZX group, they are our best ARPES collaborators. I also thank Zhanybek, Cliff, Lan, Beena and Tom, from them I learned amazing local properties of our samples. Finally I especially want to thank Cheng-Chien Chen and Joseph Maciejko, the honorable chairmen of Chen-Maciejko Institute of Theoretical Physics. They are the best theorists, and my best friends in Stanford. We had a lot of good time eating, drinking and discussing physics and things beyond physics.

GLAM is such a friendly and warm place to work in. Mark Gibson helped me a lot with shipping out the samples. Corrina Peng, Catherine Meng and Yo Wackeman, helped me a lot for travel reimbursements and purchases. I also thank Alison Veith, Ellie Lwin and Paula Perron and Claire Nicholas of Applied Physics department. They are all very nice and helpful.

During my thesis research, I was very fortunate to have many external collaborators. The polarized optical images presented in chapter 3 were taken in Yamamotos lab on campus. I thank Kristiaan, David, Leo and Peter for their help and efforts. I also want to thank Mike Toney and Cathie Condro, who helped me during the beamtime in SSRL. I worked with Zahir Islam, Jacob Ruff and Ritesh Das in APS, Argonne. I am still amazed by their incredible pulsed field x-ray diffraction measurements. Ross McDonald is our best host in Los Alamos National Lab. I also thank Stephen Hayden, Tony Carrington and Amalia Coldea from University of Bristol and Leonardo Degiorgi from ETH Zurich. We had cheerful conversations in March meeting and published a lot of beautiful papers.

Finally I would like to thank my family, my parents, my sister and my wife. My parents obtained their PhD approximately twenty-five years ago. They always encourage and support my pursuit of science. My wife Eunice started her PhD at the same time as I did, and passed her defense one month ago. Along the road she shared my joy and excitement, and supported me with her love and care. I feel truly happy and honor to become the forth (but not the last) doctor in my family.

Contents

Abstract	v
Acknowledgements	vii
1 Introduction	1
2 Materials Synthesis and Phase Diagram of $\text{Ba}(\text{Fe}_{1-x}\text{Co}_x)_2\text{As}_2$	7
2.1 Introduction	7
2.2 Single Crystal Growth	9
2.3 Transport and Thermodynamic Measurements	10
2.4 Phase Diagram	13
2.5 Discussion	21
3 In-Plane Resistivity Anisotropy of $\text{Ba}(\text{Fe}_{1-x}\text{Co}_x)_2\text{As}_2$	25
3.1 Introduction and Motivation	25
3.2 Detwinning Single Crystals by a In-plane Magnetic Field	26
3.2.1 Motivation	26
3.2.2 Experimental Methods	26
3.2.3 Results	27
3.2.4 Discussion	35
3.3 Detwinning Single Crystals by a Uni-axial Stress	36
3.3.1 Cantilever Detwinning Device	36
3.3.2 Efficacy of the Detwinning Device	37
3.4 Stress Dependence Measurement	39

3.5	Results of In-Plane Resistivity Anisotropy	41
3.6	c-axis Resistivity	45
4	Divergent Nematic Susceptibility Measured by a Tunable Strain	49
4.1	Introduction and Motivation	49
4.2	Methodology	50
4.2.1	In-situ Tunable Strain Applied by Piezo Device	50
4.2.2	Resistivity Anisotropy and Nematic Order	52
4.3	Ginzburg-Landau Theory of Electronic Nematic Phase	53
4.4	Experimental Results and Analysis	57
4.5	Control Experiment for Different Orientations	64
5	Non-monotonic Doping Dependence of Resistivity Anisotropy	67
5.1	Introduction and Motivation	67
5.2	Magnetoresistance and Hall measurements	69
5.3	Analysis of Magnetoresistance	73
5.4	Discussion	79
6	Summary and Outlook	81
	Bibliography	85

List of Tables

List of Figures

1.1	Schematic diagram illustrates the crystal structure of BaFe_2As_2 in the tetragonal state. Lattice vectors are shown by red arrows.	2
1.2	Fermi surfaces of LaFeAsO based on density functional theory calculation. Two concentric hole pockets are found at the Γ point and two electron pockets at the M point of the Brillouin zone. (Reproduced from ref[1].)	3
1.3	Generic phase diagram of the iron arsenide superconductors as a function of tuning parameter (composition, x , or pressure, P). In underdoped regime at high temperature the system is four-fold symmetric. As temperature decreases the crystal structure first breaks into a two-fold symmetry, and at lower temperature antiferromagnetic order further breaks the translational symmetry. For some materials the structural and magnetic transitions occur simultaneously, whereas for other they are separated in temperature (as shown here). For the specific case of $\text{Ba}(\text{Fe}_{1-x}\text{Co}_x)_2\text{As}_2$ studied in this thesis, the structural transition is 2nd order for all compositions, whereas the magnetic transition is first order for low Co concentration and second order for higher Co concentration.	4
2.1	The Co concentration measured by electron microprobe analysis (EMPA) verses the nominal melt composition.	9

2.2	Temperature dependence of the in-plane (ρ_{ab}) resistivity of $\text{Ba}(\text{Fe}_{1-x}\text{Co}_x)_2\text{As}_2$. Data are shown normalized by the room temperature resistivity, $\rho_{ab}(300\text{K})$, to remove uncertainty in estimates of the absolute value due to geometric factors. Successive data sets are offset vertically by 0.1 for clarity (except for $x = 0$ data, which is offset by 1.4).	11
2.3	(a) Heat capacity data for four representative Co concentrations ($x = 0, 0.016, 0.025, 0.036$ and 0.061) showing the suppression of the structural/magnetic phase transitions with increasing Co concentration. (b) Superconducting anomaly for the sample with $x = 0.061$ shown as $\Delta C/T$ vs. T , where $\Delta C = C_S - C_N$ and C_N is estimated as described in the text from the heat capacity measured in an applied field of 14 T. Data are shown for zero field, and for applied fields of 1, 3 and 5 T along the c -axis.	12
2.4	Resistivity (panels a-c) and heat capacity (panels d-f) data for samples with $x = 0, 0.016$ and 0.025 over a narrower temperature interval, showing the splitting of the single phase transition observed for $x = 0$ in to two distinct phase transitions for $x > 0$	13
2.5	Comparison of heat capacity, susceptibility, resistivity and Hall coefficient data for samples with (a) $x = 0$, (b) $x = 0.016$ and (c) $x = 0.025$. In the upper panels, the heat capacity (right axis) is shown as ΔC , having subtracted the background phonon contribution as described in the main text, together with the in-plane susceptibility χ_{ab} (left axis) and the derivative $d(\chi T)/dT$ (arb. units). In the lower panels, absolute values of the in-plane resistivity ρ_{ab} (left axis) are shown together with the Hall coefficient R_H (right axis) and the derivative $-d\rho/dT$ (arb units). Vertical dotted lines mark successive phase transitions, evident in all four physical properties.	14

2.6	Progression of the two successive phase transitions, marked as α and β , as a function of Co concentration as observed in (a) heat capacity and (b) the derivative of the resistivity $-d\rho/dT$. Heat capacity data are shown as ΔC , having subtracted the background phonon contribution as described in the main text. Data for $x = 0.025$ and 0.036 have been multiplied by factors of 3 and 5 respectively for clarity.	15
2.7	Phase diagram for $\text{Ba}(\text{Fe}_{1-x}\text{Co}_x)_2\text{As}_2$ showing the suppression of the two successive phase transitions α and β with increasing Co concentration, and the eventual superconducting (SC) "dome". Data points for T_α and T_β were obtained from heat capacity, resistivity, Hall coefficient and susceptibility data for $x = 0, 0.016, 0.025$ and 0.036 , and from resistivity data alone for $x = 0.045$ and 0.051 . Superconducting T_c values were obtained from resistivity data. Error bars indicate 10 and 90% of the resistive transition. Uncertainty in the Co concentration corresponds to less than the width of the data markers.	17
2.8	Identification of the phase transitions in $\text{Ba}(\text{Fe}_{1-x}\text{Co}_x)_2\text{As}_2$ ($x = 0.025$) (a) T dependence of the $[1\ 1\ 2]_T$ powder line determined from x-ray diffraction. (b) T dependence of integrated intensity (blue circles) of the $[1\ 1\ 2]_T$ nuclear peak determined from $\omega - 2\theta$ scans. Inset shows the Bragg profile $T = 10K$ and $120K$. The solid black line is the heat capacity. (c) T dependence of the integrated intensity (red circles) of the magnetic $[1/2\ 1/2\ 1]_T$ Bragg peak. Solid line is $-d\rho/dT$ (Figure reproduced from ref.[2])	18
2.9	Temperature dependence of susceptibility following zero-field cooling (zfc) and field cooling (fc) cycles, for both single crystal and powdered samples for three representative Co concentrations corresponding to $x = 0.045$ (underdoped), $x = 0.061$ (optimally doped) and $x = 0.109$ (overdoped). Measurements were made in a field of 50 Oe applied parallel to the ab -plane of the single crystals.	20

- 3.1 The in-plane magnetoresistance $\Delta\rho_{ab}/\rho_{ab}$ (%) of $\text{Ba}(\text{Fe}_{1-x}\text{Co}_x)_2\text{As}_2$ for $x = 2.5\%$ for two specific current orientations (sample A and B). The angle independent part of the magnetoresistance for sample B has been subtracted for clarity. The data were taken at 84K, below both T_S and T_N for this cobalt concentration. The geometry of the measurement is indicated below each panel. Both current and field are in the ab-plane, and the angle of the magnetic field is measured relative to the current direction. For sample A current is applied parallel to the orthorhombic a/b axis, whereas for sample B current is applied at 45 degree to the orthorhombic a/b axis. 28
- 3.2 (Color online) The angle dependent magnetoresistance $(\rho_{ab}(\theta, 14T) - \overline{\rho_{ab}})/\overline{\rho_{ab}}$ (where $\overline{\rho_{ab}}$ is the average of $\rho_{ab}(\theta, 14T)$ over θ) as a function of angle and temperature of $\text{Ba}(\text{Fe}_{1-x}\text{Co}_x)_2\text{As}_2$ for (a) $x = 3.6\%$ and (b) $x = 2.5\%$. The magnitude of MR is indicated by the color scale. Vertical lines indicate T_S and T_N as determined for these samples by the derivative of the resistivity (shown above each panel). 29
- 3.3 Representative magnetoresistance data for $\text{Ba}(\text{Fe}_{1-x}\text{Co}_x)_2\text{As}_2$ as a function of field and angle for $x = 1.6\%$ at $T = 80\text{K}$ (panels (a) and (b)) and $T = 20\text{K}$ (panels (c) and (d)). For all cases the current is aligned parallel to orthorhombic a/b axes and field is applied parallel to the ab plane (i.e. sample A configuration). For field sweeps, the magnetic field was swept from 0 to 14T, then 14 to -14T, then back to 0T following an initial zero-field cool. Data were taken for fields aligned parallel (red) and perpendicular (green) to the current. Angle sweeps were performed in a field of 14T following an initial zero-field cool. Data were taken continuously as the angle was increased from 0 to 360 degrees and then back to zero. The nonzero offset in (c) and (d) results from a slight mixing of out of plane field component due to a small sample misalignment. 30

3.4 Time dependence of the resistivity for a representative sample with $x = 1.6\%$, revealing thermal relaxation of the field-induced changes in the resistivity. The sample was initially cooled to 2 K in 14 T, before the field was cycled to zero. The sample was then warmed to (a) 5 K and (b) 10 K, and the resistivity measured as a function of time after the temperature had stabilized. Data are fit by an exponential relaxation, with resulting time constants of $3.3 \pm 1.8 \times 10^3$ and $1.8 \pm 0.4 \times 10^3$ s respectively. 32

3.5 Temperature dependence of the resistivity for representative samples with $x = 1.6\%$ (panels (a) and (b)) and $x = 2.5\%$ (panels (c) and (d)). Data were taken during an initial field cool (FC) in 14T, after which the field was cycled to zero and the resistivity measured in zero field while warming (ZFW). The current is aligned parallel to the a/b orthorhombic axes, and the field applied either parallel (red) or perpendicular (green) to the current. For comparison, data are also shown for the same samples while cooled in zero field (ZFC). The FC MR $((\rho_{FC} - \rho_{ZFC})/\rho_{ZFC})$ and ZFW resistivity difference induced by field cooling $((\rho_{ZFW} - \rho_{ZFC})/\rho_{ZFC})$ for the two field configurations are also plotted in (b) for $x = 1.6\%$ and (d) for $x = 2.5\%$. Vertical lines indicate T_S and T_N 33

- 3.6 Representative optical images of a $\text{Ba}(\text{Fe}_{1-x}\text{Co}_x)_2\text{As}_2$ sample for $x = 2.5\%$, revealing the partial detwinning effect of an in-plane magnetic field. The images (obtained as described in the main text) were taken at $T = 40\text{K}$ below both T_S and T_N . The initial image (a) was taken in zero field, following a zero field cool from above T_N . The field was then swept to 10T , at which field the second image (b) was taken. Horizontal intensity profiles, shown below each image, were calculated by integrating vertically over the image area after background subtraction and noise filtering. Boundaries between domains were estimated as described in the main text, resulting in an estimate of the relative fraction of the two domains indicated by black and white stripes below the figures. The field, which was oriented along the orthorhombic a/b axes, has clearly moved the twin boundaries, favoring one set of twin domains (light) over the other (dark). 34
- 3.7 **(A)** Diagram of the crystal structure of BaFe_2As_2 in the antiferromagnetic state. The magnetic moments on the iron sites point in the a-direction, and align anti-parallel along the longer a-axis, and parallel along the shorter b-axis. **(B)** Diagram illustrating a twin boundary between two domains that form on cooling through the structural transition at T_s . Dense twinning in macroscopic crystals obscures any in-plane electronic anisotropy in bulk measurements. **(C)** Diagram of the device used to detwin single crystals in situ. The sample is held sandwiched between a cantilever and a substrate, with a screw in the center of the cantilever to adjust the uni-axial pressure. The $(0\ 0\ 1)$ surface of the crystal is exposed, enabling transport measurements. 36
- 3.8 Photograph of the device used to detwin single crystals in situ. A representative sample is held sandwiched between a cantilever and a substrate, with a screw in the center of cantilever to adjust the uni-axial pressure. The $(0\ 0\ 1)$ surface of the crystal is exposed, enabling transport measurements. 37

3.9 (A) Splitting of the (-2 -2 20) Bragg peak (referenced to the tetragonal lattice) at 40 K for a sample with $x = 0.025$ under uni-axial pressure, as revealed by high-resolution x-ray diffraction. The two dimensional surface is formed by interpolating between Gaussian fits to a dense mesh of points from h-k scans. Each peak corresponds to one of the two twin domains. The relative volume fraction of the larger domain, corresponding to the shorter b -axis aligned parallel to the applied stress, is approximately 86%. (B) Polarized-light image of the surface of an unstressed BaFe_2As_2 crystal at 5K without applying uni-axial pressure. Vertical light and dark stripes reveal the existence of twin domains with a and b axes reversed. (C) Polarized-light image on the surface of the same crystal under uni-axial pressure at 5K. The absence of stripes indicates the applied pressure has detwinned the crystal. 38

3.10 Representative data illustrating the variation in the temperature dependence of the b -axis resistivity as a function of the external stress for a sample with 2.5 % Cobalt doping. The magnitude of the stress, which is aligned along the current direction, is tuned as described in the main text. Lower panel shows the resistivity normalized by its room temperature value. Upper panel shows the temperature derivatives of the resistivity (successive data sets are shifted for clarity). The sharp feature associated with the SDW transition is essentially unaffected by the external stress. However, the clear feature observed in the resistivity that is associated with the structural transition for an unstressed crystal is progressively broadened by applied pressure, due to the finite nematic susceptibility above T_S 40

3.11 Temperature dependence of the in-plane resistivity ρ_a (green) and ρ_b (red) of $\text{Ba}(\text{Fe}_{1-x}\text{Co}_x)_2\text{As}_2$ for Co concentrations from $x = 0$ to 0.085. Solid and dashed vertical lines mark critical temperatures for the structural and magnetic phase transitions T_S and T_N respectively. Values of T_N for stressed samples, obtained from the peak in the derivative of the resistivity, are identical to those found for unstressed samples, indicating that the uni-axial pressure serves as a weak symmetry breaking field to orient twin domains without affecting the bulk magnetic properties. The uni-axial stress does, however, affect the superconducting transitions in some underdoped samples, inducing a partial superconducting transition for $x = 0.016$ and 0.025, which are not observed for unstressed crystals. Diagrams in the right-hand panel illustrate how measurements of ρ_a and ρ_b were made. Dark arrows indicate the direction in which uni-axial pressure was applied, and smaller arrows indicate the orientation of the a and b crystal axes. In all cases, the same samples and the same contacts (shown in gold for a standard 4-point configuration) were used for both orientations. 42

3.12 **(A)** Evolution of the in-plane resistivity anisotropy as a function of temperature and doping, expressed in terms of the resistivity ratio ρ_b/ρ_a . Structural, magnetic and superconducting critical temperatures, shown as circles, squares and triangles respectively. Significantly, the resistivity ratio deviates from unity at a considerably higher temperature than T_S , indicating that nematic fluctuations extend far above the phase boundary. **(B)** The difference in the temperature derivative of ρ_a and ρ_b ($d(\overline{\rho}_a - \overline{\rho}_b)/dT$, where $\overline{\rho}_a = \rho_a/\rho_a(300K)$, $\overline{\rho}_b = \rho_b/\rho_b(300K)$) as a function of temperature and doping. The resistivity has been normalized by its room temperature value to avoid uncertainty due to geometric factors. Regions of highest intensity are those regions where ρ_b appears to be insulator-like ($d\rho_b/dT < 0$) while ρ_a remains metallic ($d\rho_a/dT > 0$). This behavior is clearly correlated with the nematic phase between the structural and magnetic transitions. 43

- 3.13 Temperature dependence of the inter-plane resistivity ρ_c (black) and in-plane resistivity ρ_b (red) and ρ_a (green) of underdoped $\text{Ba}(\text{Fe}_{1-x}\text{Co}_x)_2\text{As}_2$ for cobalt concentrations from $x = 0$ to 0.051. Data are shown normalized by the room-temperature resistivity $\rho(300K)$ to remove uncertainty in estimates of the absolute value due to geometric factors. Measurements of ρ_a and ρ_b for each composition were made on the same crystal and with the same contacts, as described in previous sections. Measurements of ρ_c were made for separate crystals using a quasi-Montgomery technique. 46
- 3.14 Temperature dependence of the inter-plane resistivity ρ_c (black) and in-plane resistivity ρ_a (green) of optimal and overdoped $\text{Ba}(\text{Fe}_{1-x}\text{Co}_x)_2\text{As}_2$ for Cobalt concentration from $x = 0.07$ to 0.184. Data are shown normalized by the room-temperature resistivity $\rho(300K)$ to remove uncertainty in estimates of the absolute value due to geometric factors. . . 48
- 4.1 **(A)** Schematic diagram of a piezoresistance measurement (upper panel) and of a strain gauge measurement(lower panel). Details about the configuration are described in the supporting online materials. **(B)**(Upper) The relative change of resistivity ($\eta = \Delta\rho/\rho_0$) of a BaFe_2As_2 sample and the strain measured by strain gauge on piezo ($\epsilon_P = \Delta L/L$) as a function of voltage at $T = 140K$. The strain and resistance were measured along the $[1\ 1\ 0]_T$ direction of the crystal. (Lower) Same set of data but η is plotted against ϵ_P . The red line is a linear fit to the data. **(C)(D)** The difference of the strain between zero applied voltage and (C) $V_p = 150V$ and (D) $V_p = 50V$. Dash lines indicate the temperatures below which the strain is fully transmitted to the sample. For low voltage this temperature window spans well above T_S for all compositions studied. 51

4.2	<p>(A) Representative data for BaFe_2As_2 showing the relative change of resistivity ($\eta = \Delta\rho/\rho_0$) as a function of strain ($\epsilon_P = \Delta L/L$) at several temperatures above T_S. The nematic response was obtained by a linear fit of the data near zero applied voltage ($-5 \times 10^{-5} < \epsilon_p(V) - \epsilon_p(0) < 1 \times 10^{-4}$, indicated by the vertical dashed lines). (B) Temperature dependence of the nematic response $d\eta/d\epsilon_P$. Vertical line indicates the structural transition temperature $T_S = 138\text{K}$. Red line shows fit to mean field model, described in the main text.</p>	59
4.3	<p>Temperature dependence of the nematic susceptibility of $\text{Ba}(\text{Fe}_{1-x}\text{Co}_x)_2\text{As}_2$ for various compositions (open symbols). Successive data sets are offset vertically by 50 for clarity. Solid lines are fits based on a phenomenological Ginzburg-Landau theory, taking into account an intrinsic built-in strain, which is measured by η_0 shown in inset figure.</p>	61
4.4	<p>Evolution of the nematic susceptibility ($d\eta/d\epsilon$) of $\text{Ba}(\text{Fe}_{1-x}\text{Co}_x)_2\text{As}_2$ as a function of temperature and doping. Structural, magnetic and superconducting transition temperatures (T_S, T_N and T_c) are shown as squares, triangles and circles. The mean field electronic nematic critical temperature (T^*) obtained from the fit to the data in Fig. 4.3 are shown as open red stars. The evolution of nematic susceptibility and nematic critical temperatures clearly indicates an electronic nematic quantum phase transition occurs close to optimal doping.</p>	62
4.5	<p>Doping dependence of the parameters obtained from the numerical fit based on the Ginzburg-Landau theory.</p>	63
4.6	<p>Photograph of two representative crystals mounted on a piezo stack used to apply in situ tunable strain. Two samples are mounted, corresponding to $\epsilon// [110]_T$ (upper crystal) and $\epsilon// [100]_T$ (lower crystal). Red/black wires are the positive/negative voltage leads of the piezo. The (0 0 1) surface of the crystal is exposed, enabling transport measurements.</p>	64

4.7 Representative data showing the temperature dependence of the nematic response $d\eta/d\epsilon_P$ of $\text{Ba}(\text{Fe}_{0.935}\text{Co}_{0.065})_2\text{As}_2$ samples, for the two configurations shown in fig. S1. Samples were prepared so that the strain and current were aligned along the $[1\ 1\ 0]_T$ (Fe-Fe bonding direction) and $[1\ 0\ 0]_T$ (Fe-As bonding direction), shown as black and red symbols respectively. Vertical line indicates the superconducting critical temperature $T_c = 25\text{K}$ of these optimal doped samples. Inset shows the relative change of resistivity ($\eta = \Delta\rho/\rho_0$) as a function of strain ($\epsilon_P = \Delta L/L$) at $T = 30\text{K}$. Lines show linear fits. 65

5.1 In-plane resistivity anisotropy, ρ_b/ρ_a , as a function of temperature and doping for (a) $\text{Ba}(\text{Fe}_{1-x}\text{Co}_x)_2\text{As}_2$ and (b) $\text{Ba}(\text{Fe}_{1-x}\text{Ni}_x)_2\text{As}_2$. The color scale has been obtained by a linear interpolation between adjacent data points. The same scale has been used for all three panels. Black circles, Squares, and triangles indicate T_S , T_N , and T_c respectively, determined for unstressed conditions. T_c for $\text{Ba}(\text{Fe}_{1-x}\text{Co}_x)_2\text{As}_2$ and $\text{Ba}(\text{Fe}_{1-x}\text{Ni}_x)_2\text{As}_2$ was defined by the midpoint of the superconducting transitions. ($\text{Ba}(\text{Fe}_{1-x}\text{Ni}_x)_2\text{As}_2$ data courtesy of Hsueh-Hui Kuo) . . . 69

5.2 Transverse magnetoresistance(MR) ($\Delta\rho/\rho$) of $\text{Ba}(\text{Fe}_{1-x}\text{Co}_x)_2\text{As}_2$ for (a) $x = 0$ (b) 3.5% at $T = 25\text{K}$. The MR has been measured on detwinned samples with current along a/b axis (Green/Red curves), and also on twinned sample(Black curve). (c,d) The MR of twinned samples of $\text{Ba}(\text{Fe}_{1-x}\text{Co}_x)_2\text{As}_2$ and $\text{Ba}(\text{Fe}_{1-x}\text{Ni}_x)_2\text{As}_2$ respectively at 25 K. *Data for $x = 0$ has been scaled down by a factor of two for clarity. ($\text{Ba}(\text{Fe}_{1-x}\text{Ni}_x)_2\text{As}_2$ data courtesy of Hsueh-Hui Kuo) 70

5.3	(a) The field derivative of MR of twinned samples of $Ba(Fe_{1-x}Co_x)_2As_2$ and (b) $Ba(Fe_{1-x}Ni_x)_2As_2$ *Data for $x = 0$ has been scaled down by a factor of two for clarity. (c) The field derivative of MR (dMR/dB) measured on a twinned sample of the parent compound at $T = 25K$. A critical field scale B^* clearly divides the MR behavior into two regimes: below B^* the MR shows a weak field quadratic behavior and above B^* MR shows a high field linear behavior. (d) The doping evolution of the field scale B^* (blue circles) and the high field MR linear coefficient A_1 (red squares), for $Ba(Fe_{1-x}Co_x)_2As_2$ and $Ba(Fe_{1-x}Ni_x)_2As_2$ (solid and open symbols respectively).($Ba(Fe_{1-x}Ni_x)_2As_2$ data courtesy of Hsueh-Hui Kuo)	71
5.4	The doping evolution of the effective MR mobility μ_{MR} and effective MR carrier density n_{MR} of $Ba(Fe_{1-x}Co_x)_2As_2$ and $Ba(Fe_{1-x}Ni_x)_2As_2$ extracted from weak field MR , as described in the text.	77
5.5	The doping evolution of the in-plane resistivity of the twinned crystals at $T = 25K$ normalized by its room temperature value and the in-plane resistivity anisotropy ratio ρ_b/ρ_a of detwinned crystal at $T = 25K$. Data are plotted for (a) $Ba(Fe_{1-x}Co_x)_2As_2$, (b) $Ba(Fe_{1-x}Ni_x)_2As_2$ ($Ba(Fe_{1-x}Ni_x)_2As_2$ data courtesy of Hsueh-Hui Kuo)	78

Chapter 1

Introduction

The discipline of condensed matter physics involves the study of systems that consist of enormous numbers of particles. Due to correlation effects between these particles, striking collective phenomena emerge. These phenomena often cannot be predicted or understood by the physical laws that govern the behavior of the individual particles. One example is the occurrence of high temperature superconductivity, which is also perhaps the most challenging phenomenon for physicist to understand. First discovered in copper oxide materials in 1986[3], which show superconductivity at temperatures of the order of $100K$, more recently high temperature superconductivity has also been discovered in iron based materials[4], which show superconductivity at temperatures as high as $55K$ [5]. For both classes of materials, the stoichiometric parent compounds are almost always antiferromagnets rather than superconductors¹. Superconductivity is induced by suppression of antiferromagnetic state by tuning parameters such as doping or pressure. Although the mechanism of high temperature superconductivity is still under debate, intensive experimental studies revealed rich and complicated $x - T$ phase diagrams for both classes of materials. An important consensus is that a coherent theory of high T_c superconductor also needs to explain the “parent” electronic phases that are in the proximity of superconducting phase[6, 7]. The main goal of this thesis is to explore and understand the nature of the parent

¹Stoichiometric LiFeAs and NaFeAs are superconductors. However it has been argued that they belong to the underdoped and overdoped part of the phase diagram.

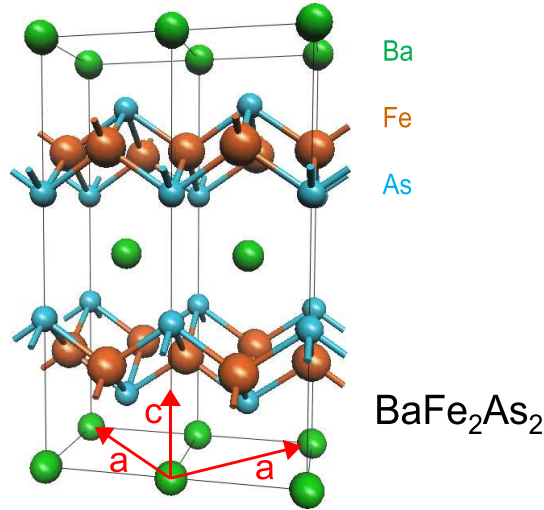


Figure 1.1: Schematic diagram illustrates the crystal structure of BaFe_2As_2 in the tetragonal state. Lattice vectors are shown by red arrows.

phase of iron based superconductors.

There are various types of iron based superconductors, which can be divided into two major categories: the iron pnictides and iron chalcogenides. These categories can be further divided into several families of compounds based on their chemical formulas and crystal structures. The common ingredient of the crystal structure of all types of iron based superconductors is iron pnictide/chalcogenide layer. In this layer pnictogens (As/P) or chalcogens (Se/Te) atoms sit either above or below the center of iron square lattice, tetrahedrally coordinate the iron ions. For example, Fig. 1.1 shows the crystal structure of BaFe_2As_2 , the parent compound of “122” class. It can be seen that the iron arsenide layers are in between barium atoms. The barium atoms donate electrons to FeAs planes and served as spacer layers, which are also part of the crystal structure that varies among different families. However all the electronic action, including superconductivity, takes place in the iron layers.

In general, the electronic properties of iron pnictides show a more metallic behavior than iron chalcogenides, and also suffer less from the disorder effect of iron interstitials or vacancies[8]. In this thesis I focus on the “122” iron pnictides family, in particular

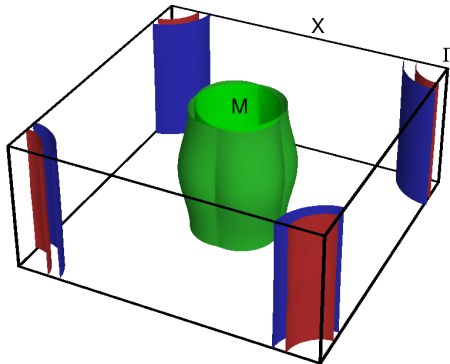


Figure 1.2: Fermi surfaces of LaFeAsO based on density functional theory calculation. Two concentric hole pockets are found at the Γ point and two electron pockets at the M point of the Brillouin zone. (Reproduced from ref[1].)

the $\text{Ba}(\text{Fe}_{1-x}\text{Co}_x)_2\text{As}_2$ system. The advantage of this system is that large single crystals can be easily synthesized, and chemically the amount of cobalt substitution is also well controlled.

The electronic structure of iron pnictides has been intensively studied theoretically [9] and experimentally [10, 11]. The stoichiometric parent compound is a compensated metal, containing equal number of electrons and holes. The Fermi surfaces comprise quasi two dimensional cylinders with hole pockets at the center and electron pockets at the corner of the Brillouin zone. In general the electronic structures of all the iron pnictides are very similar, and the Fermi surface of LaFeAsO shown in Fig.1.2 is a representative example. One important feature that can be found in this figure is that the electron and hole Fermi surfaces can be fairly well nested by a wave vector of $(\pi, \pi)^2$. And this wave vector also happens to be the ordering wave vector of the collinear antiferromagnetic phase of the parent compounds [12]. It has been argued that this antiferromagnetic phase is actually a spin-density wave driven by Fermi surface nesting instability [13]. However experimental findings suggests that local magnetic moments persist even in the paramagnetic state [14], which is inconsistent with a fully itinerant picture. The reconstructed Fermi surfaces in the antiferromagnetic state

²here we use the "two iron" unit cell, in which there two inequivalent Fe atoms per unit cell, distinguished by the alternating tetrahedral coordination of the pnictogen or chalcogen anions.

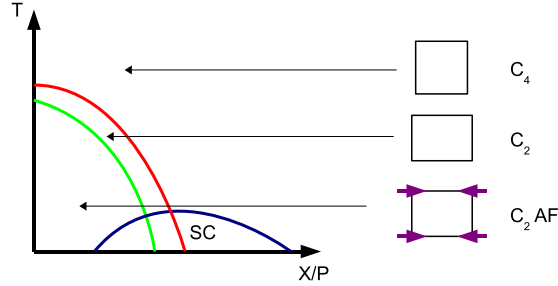


Figure 1.3: Generic phase diagram of the iron arsenide superconductors as a function of tuning parameter (composition, x , or pressure, P). In underdoped regime at high temperature the system is four-fold symmetric. As temperature decreases the crystal structure first breaks into a two-fold symmetry, and at lower temperature antiferromagnetic order further breaks the translational symmetry. For some materials the structural and magnetic transitions occur simultaneously, whereas for other they are separated in temperature (as shown here). For the specific case of $\text{Ba}(\text{Fe}_{1-x}\text{Co}_x)_2\text{As}_2$ studied in this thesis, the structural transition is 2nd order for all compositions, whereas the magnetic transition is first order for low Co concentration and second order for higher Co concentration.

also cannot be described by a simple band-folding scenario[15]. A description based on intermediate coupling might be more appropriate.

Suppression of the antiferromagnetic state by either applied pressure [16] or chemical doping [17, 18] results in superconductivity. It has been proposed that the spin fluctuations associated with suppressed antiferromagnetism form the superconducting pairing glue between the electron and hole pockets, and the associated pairing symmetry is so called extended $S\pm$ wave[19]. Spin resonance measured by inelastic neutron scattering support this proposal[20, 21]. However, unlike copper oxide superconductors, the question about the existence and the location of line nodes in superconducting gaps is far from clear. Experimental evidences suggest that the existence of line nodes depends on types of materials and even sensitively depends on the chemical doping within a single family of the iron based superconductors[22, 23, 24]. One important challenge for the theory of superconductivity in this class of materials

is to reconcile this complex phenomenology[25].

The antiferromagnetic phase and superconducting phase are not the only two symmetry breaking phases of iron pnictides. Significantly, the antiferromagnetic transition is always preceded by or coincident with a tetragonal to orthorhombic structural distortion[26, 27]. The evolution from orthorhombic antiferromagnetic phase to superconductivity is depicted by a generic phase diagram shown in Fig. 1.3. The separation of structural and magnetic transition leaves a finite temperature and doping range in the phase diagram, in which the crystal rotational symmetry is broken without the formation of spatial periodic order. It has been soon proposed that the structural orthorhombicity might not be the principle order parameter, and the phase transition is actually driven by an instability in the electronic system. The theoretical proposals can be categorized into two school of thoughts based on their proposed principle order parameters. (i) Anisotropy of the spin fluctuations[28, 29, 30]. (ii) Polarization in d_{xz} and d_{yz} orbital[31, 32]. Although the microscopic mechanism of the driving force is different, both models involve a spontaneously broken rotational symmetry in the electronic degrees freedom. Borrowing the language from the field of liquid crystal, we refer to such an order as electronic nematic phase.

Electronic systems with spontaneously organized orientational order have long been investigated. Canonical examples include half filling Quantum Hall states[33], the field induced metamagnetic state in $\text{Sr}_3\text{Ru}_2\text{O}_7$ [34] and most recently the hidden order state in URu_2Si_2 [35], in which cases the crystal lattice's fourfold symmetry remains almost unperturbed yet the electronic ground states exhibit a strong two-fold anisotropy.[36]. There is also some evidence of the existence of an electronic nematic phase in underdoped cuprates[37, 38]. In particular, the recent observation of a large in-plane anisotropy in the Nernst effect in $\text{YBa}_2\text{Cu}_3\text{O}_{7-\delta}$ suggests that the much-debated pseudo-gap phase is a rotational symmetry breaking phase[39].

The main goal of this thesis is to explore the rotational symmetry breaking phase of iron arsenide superconductor using an experimental approach. In general, we applied external stress field or magnetic field to perturb the system and read the response through resistivity measurements.

In chapter two, I will first present crystal synthesis, transport and thermodynamic characterization of the prototypical iron arsenide materials $\text{Ba}(\text{Fe}_{1-x}\text{Co}_x)_2\text{As}_2$. The detail measurements resolved the separation of magnetic and structural transition, and map out the temperature verses doping phase diagram, which forms the basis of the following chapters. In order to access the intrinsic in-plane anisotropy in the broken symmetry phase, we have developed two methods to align the twin domains: using uni-axial stress and in-plane magnetic fields. Both will be described in chapter three. Measurements of detwinned single crystals of $\text{Ba}(\text{Fe}_{1-x}\text{Co}_x)_2\text{As}_2$ revealed a large in-plane resistivity anisotropy, which persists above the structural transition temperature and shows a striking non-monotonic doping dependence. The anisotropy above the phase transition is due to fluctuations of broken symmetry state. In chapter four I will describe how these fluctuations can be quantitatively measured by applying an in-situ tunable strain, and in combination with a phenomenological Ginzburg-Landau theory, how we are able to definitely show that the phase transition is driven by a instability in the electronic system. In chapter five I discuss the non-monotonic doping dependence of resistivity anisotropy, and how this could be related to symmetry protected Dirac pockets that emerge due to Fermi surface reconstruction in the antiferromagnetic.

The results presented in the thesis have been published in several references[40, 41, 42, 43, 44]. Additional related measurements performed by collaborators on crystal grown as part of this thesis have also been published [2, 45, 46, 47].

Chapter 2

Materials Synthesis and Phase Diagram of $\text{Ba}(\text{Fe}_{1-x}\text{Co}_x)_2\text{As}_2$

In this chapter, I describe the materials synthesis of single crystal samples of the electron-doped superconductor $\text{Ba}(\text{Fe}_{1-x}\text{Co}_x)_2\text{As}_2$. I will also present data of thermodynamic and transport measurements on these samples, which delineate an $x - T$ phase diagram with a separated structural and magnetic phase transitions. The materials presented in this chapter is published in [40].

2.1 Introduction

BaFe_2As_2 is a prototypical member of the new family of Fe-pnictides that play host to high temperature superconductivity. The stoichiometric compound suffers a structural and antiferromagnetic transition at ~ 140 K [17]. Suppression of the broken-symmetry state by either applied pressure [16] or chemical doping [48, 18] results in superconductivity, and one of the key questions associated with this entire class of material is the role played by spin fluctuations associated with the incipient tendency towards magnetism [19].

Initial work on chemical substitution in BaFe_2As_2 focused on the hole-doped material $\text{Ba}_{1-x}\text{K}_x\text{Fe}_2\text{As}_2$ [17]. In this case, it has been established that the structural/magnetic transition is totally suppressed for K concentrations above $x = 0.4$

[49], whereas superconductivity appears for a wide range of concentrations from $x = 0.3$ to 1 [49]. It has also been shown that Co-substitution (i.e. $\text{Ba}(\text{Fe}_{1-x}\text{Co}_x)_2\text{As}_2$) also suppresses the magnetic and structural transitions, eventually leading to superconductivity [18]. Co-doped BaFe_2As_2 is especially attractive for two reasons. First, from a fundamental point of view, this material allows an exploration of the interrelation between the structural/magnetic phase transitions with superconductivity in the context of an electron-doped system. Secondly, from a more practical perspective, crystal growth using cobalt does not suffer from the inherent difficulties associated with using potassium. Cobalt has neither a large vapour pressure nor attacks the quartz tubing used to encapsulate the growths. It is thus possible to obtain more homogeneous crystals and more reproducible synthesis conditions than is otherwise feasible for potassium-doped samples.

In this chapter we present results of resistivity, Hall coefficient, heat capacity and susceptibility measurements of single crystal samples of $\text{Ba}(\text{Fe}_{1-x}\text{Co}_x)_2\text{As}_2$. We find that the structural/magnetic phase transition which occurs at 134 K in BaFe_2As_2 is rapidly suppressed, and splits in to two successive phase transitions with increasing Co concentration. The signatures of these two distinct phase transitions are relatively sharp, and it is unlikely that this effect is associated with phase separation due to a variation in Co concentration across an individual sample. Superconductivity appears for Co concentrations $0.025 < x < 0.18$, with a maximum T_c for a Co concentration of $x \sim 0.06$, coincident with the concentration at which the structural/magnetic phase transitions are suppressed below T_c . The apparent coexistence of superconductivity with the broken-symmetry state on the underdoped side of the phase diagram is unlikely to be due to phase separation due to Co inhomogeneity, and mirrors what is seen for $\text{Ba}_{1-x}\text{K}_x\text{Fe}_2\text{As}_2$ [49]. These measurements establish an essential symmetry between electron and hole doping of BaFe_2As_2 , in which the appearance of superconductivity in both cases is clearly associated with suppression of the magnetic/structural phase transitions. Nevertheless, there are some clear differences that emerge from this study. Specifically, Co-substitution is found to be significantly more effective at suppressing the structural/magnetic phase transitions than K-substitution, and the superconducting “dome” extends over a much smaller

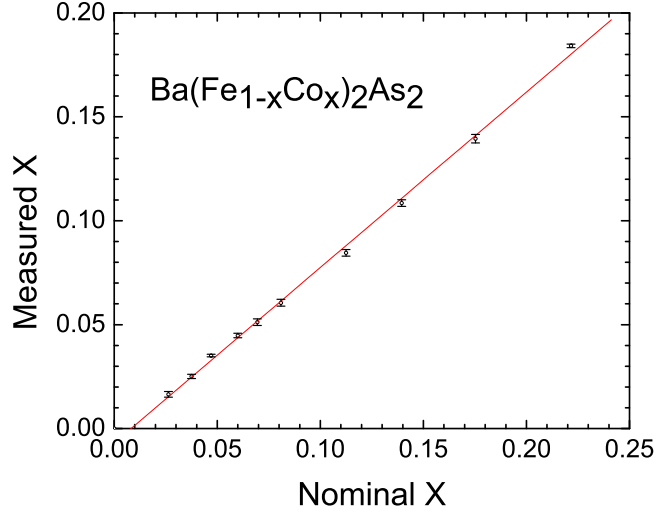


Figure 2.1: The Co concentration measured by electron microprobe analysis (EMPA) verses the nominal melt composition.

range of doping. The resulting phase diagram is highly suggestive that superconductivity is intimately related to the presence of a quantum critical point associated with suppression the structural and/or magnetic phase transitions.

2.2 Single Crystal Growth

Single crystals of $\text{Ba}(\text{Fe}_{1-x}\text{Co}_x)_2\text{As}_2$ were grown from a FeAs self flux methods [50, 18]. The FeAs precursor was synthesized by the reaction of Fe powders and As lumps. The mixture was placed in an alumina crucible and sealed in an evacuated quartz ampoule, then underwent a long heating cycle. It was ramped from room temperature to 600°C at a speed of $25^\circ\text{C}/\text{hour}$, and then held at 600°C for 24 hours. Next it was ramped to 700°C at a speed of $10^\circ\text{C}/\text{hour}$, and then held at 700°C for another 25 hours. Finally it was ramped from 700°C to 900°C at a speed of $20^\circ\text{C}/\text{hour}$, and then held at 900°C for 24 hours. After the whole heating procedures, the growth was cooled by shutting off the furnace. The purpose of long temperature cycles is to avoid rupture

of quartz ampoule by arsenic gas pressure. In order to reduce the risk of exposure to the extreme toxicity of arsenic, the quartz ampoules were also contained by stainless steel tubes, and the furnace is housed in an enclosure connected to a fume hood ventilation system.

The synthesized FeAs and elemental Ba in the molar ratio 4:1 with additional Co were placed in an alumina crucible and sealed in evacuated quartz tubes. The mixture was heated to 1150°C at a speed of $100^\circ\text{C}/\text{hour}$, and held for 24 hours. The growth was then slowly cooling to 1000°C at a speed less than $5^\circ\text{C}/\text{hour}$. At 1000°C the remaining flux was decanted using a centrifuge. The crystals have a plate-like morphology, with the c -axis perpendicular to the plane of the plates, and grow up to several millimeters on a side. The Co concentration was measured by electron microprobe analysis (EMPA) using undoped BaFe_2As_2 and elemental Co as standards. Measurements were made at several locations on each sample. As shown in Fig. 2.1, measured values were close to the nominal melt composition in all cases, and the variation in Co concentration across individual samples was typically characterized by a standard deviation of 0.15%. For instance, the Co concentration corresponding to optimal doping is $x = 0.061 \pm 0.002$.

2.3 Transport and Thermodynamic Measurements

The in-plane electrical resistivity (ρ_{ab}) was measured with a standard four-probe configuration using a Quantum Design Physical Properties Measurement System (PPMS), and the results are summarized in Fig.2.2. Data are shown normalized by the room temperature resistivity, $\rho_{ab}(300\text{K})$, to remove uncertainty in estimates of the absolute value due to geometric factors¹. The anomaly associated with the magnetic/structural phase transition in undoped BaFe_2As_2 is clearly visible at 134 K. This feature changes from a sharp drop in the resistivity below the transition temperature for BaFe_2As_2 , to an abrupt upturn for Co-doped samples. The anomaly

¹Absolute values of $\rho_{ab}(300\text{K})$ for three representative Co concentrations are $0.676\text{ m}\Omega\text{cm}$ ($x=0$, undoped), $0.906\text{ m}\Omega\text{cm}$ ($x=0.061$, optimally doped), and $0.696\text{ m}\Omega\text{cm}$ ($x=0.18$, completely over-doped)

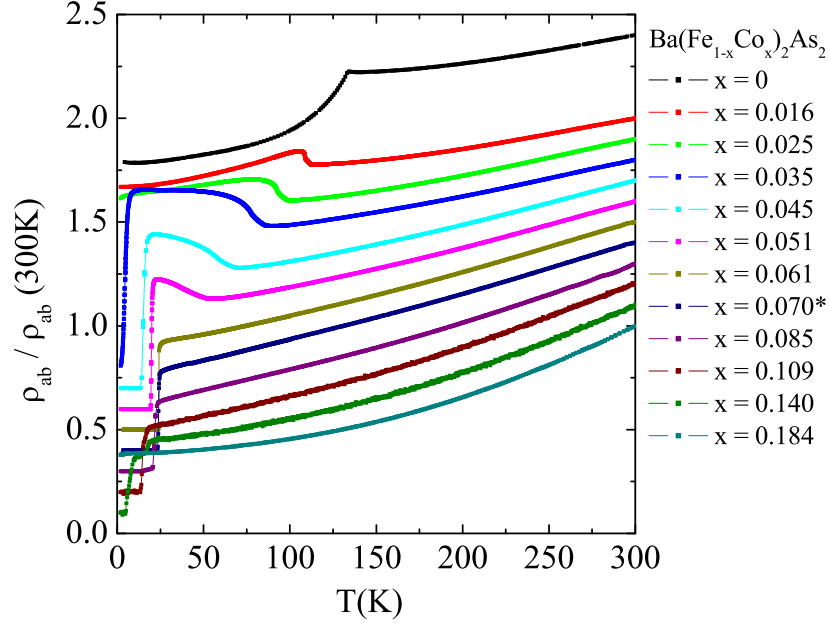


Figure 2.2: Temperature dependence of the in-plane (ρ_{ab}) resistivity of $\text{Ba}(\text{Fe}_{1-x}\text{Co}_x)_2\text{As}_2$. Data are shown normalized by the room temperature resistivity, $\rho_{ab}(300\text{K})$, to remove uncertainty in estimates of the absolute value due to geometric factors. Successive data sets are offset vertically by 0.1 for clarity (except for $x = 0$ data, which is offset by 1.4).

is clearly suppressed in temperature with increasing x . For samples with $x > 0.035$ superconductivity is evident from a sharp drop to zero in the resistivity, while the anomaly associated with the structural/magnetic phase transition is still observable in the normal state. As x increases beyond this value, the superconducting critical temperature T_c (defined here as the midpoint of the resistive transition) increases, whereas the magnetic/structural anomaly continues to be suppressed. Finally T_c reaches the highest value of 24 K in the sample with $x = 0.061$ (“optimal” doping), for which the normal state anomaly is no longer observable. Further increasing x beyond this value results in an eventual suppression of superconductivity (“overdoping”). For the sample with $x = 0.184$, T_c is below our instrumental base temperature

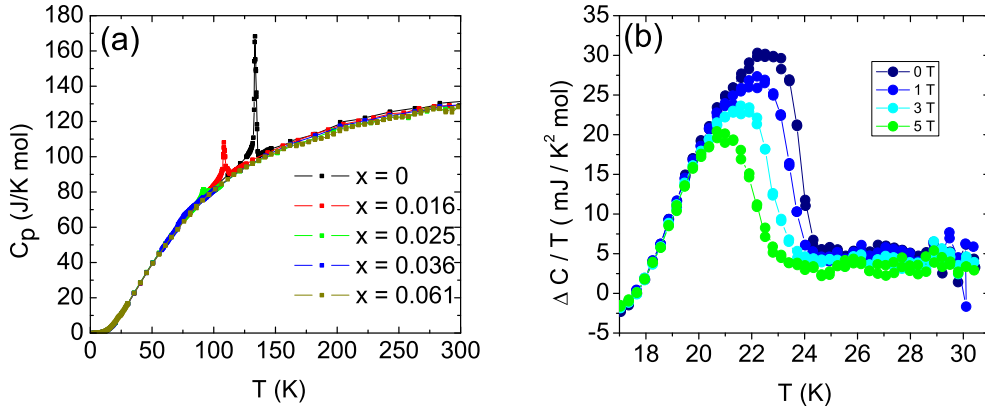


Figure 2.3: (a) Heat capacity data for four representative Co concentrations ($x = 0, 0.016, 0.025, 0.036$ and 0.061) showing the suppression of the structural/magnetic phase transitions with increasing Co concentration. (b) Superconducting anomaly for the sample with $x = 0.061$ shown as $\Delta C/T$ vs. T , where $\Delta C = C_S - C_N$ and C_N is estimated as described in the text from the heat capacity measured in an applied field of 14 T. Data are shown for zero field, and for applied fields of 1, 3 and 5 T along the c -axis.

of 1.8 K.

The suppression of the magnetic/structural phase transitions was also followed by heat capacity, measured for single crystal samples by a relaxation technique using a Quantum Design PPMS. Results are shown in Fig. 2.3(a) for four representative Co concentrations. For undoped BaFe_2As_2 , a sharp peak at 134 K marks the first order structural/magnetic phase transition as reported previously [51]. With increasing x both the transition temperature and the magnitude of the peak are rapidly suppressed, until the anomaly becomes almost unobservable for $x > 0.036$. In order to provide an estimate of the phonon background, the heat capacity was also measured for an optimally doped sample (i.e. $x = 0.061$, which is the smallest Co concentration for which the magnetic/structural phase transition is totally suppressed). These data were taken to lower temperature, revealing the superconducting anomaly. Data for this particular Co-concentration are shown in Fig. 2.3(b) as $\Delta C/T$ vs. T , where ΔC is the difference between the heat capacity in the superconducting state C_S and the

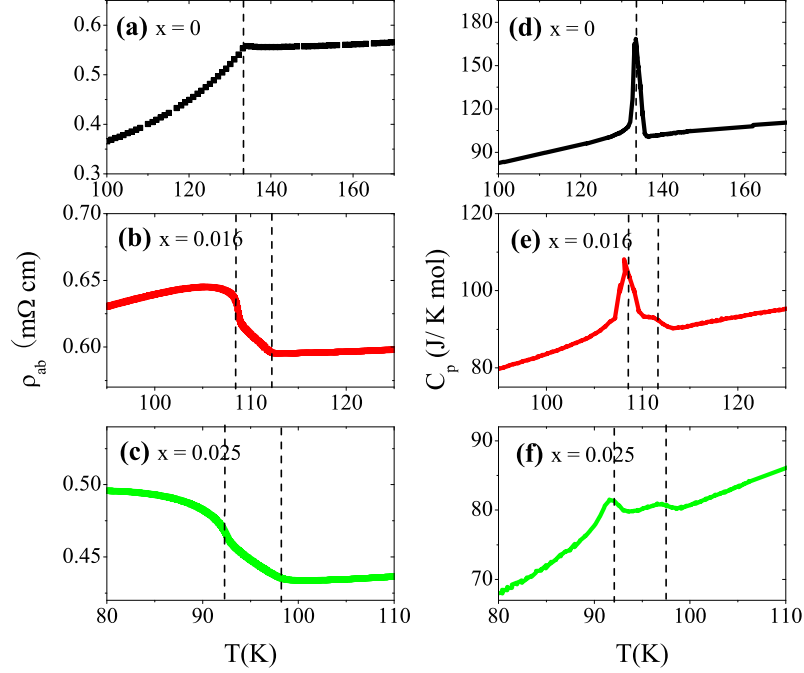


Figure 2.4: Resistivity (panels a-c) and heat capacity (panels d-f) data for samples with $x = 0, 0.016$ and 0.025 over a narrower temperature interval, showing the splitting of the single phase transition observed for $x = 0$ in to two distinct phase transitions for $x > 0$.

normal state C_N . The latter quantity has been estimated over the plotted temperature range from measurements made in a field of 14 T applied along the c -axis. These data indicate $\Delta C/T_c \approx 23$ (mJ/K² mol) in zero field.

2.4 Phase Diagram

Careful inspection of the resistivity and heat capacity data shown in Figs 2.2 and 2.3 reveal that the single anomaly associated with the magnetic/structural phase transition which is seen for undoped BaFe₂As₂ splits in to two distinct features for the Co-doped samples. In fig 2.4 we show the resistivity and heat capacity anomaly near

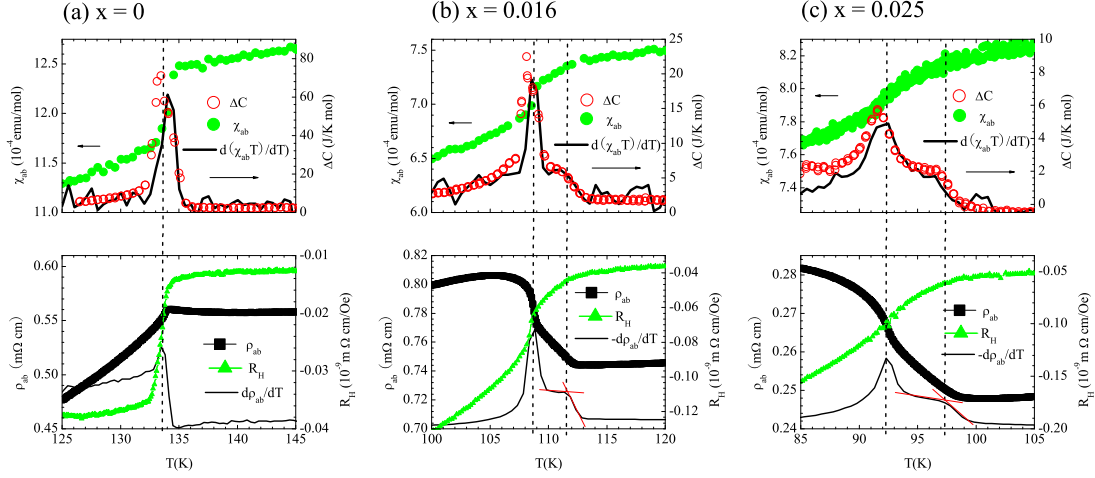


Figure 2.5: Comparison of heat capacity, susceptibility, resistivity and Hall coefficient data for samples with (a) $x = 0$, (b) $x = 0.016$ and (c) $x = 0.025$. In the upper panels, the heat capacity (right axis) is shown as ΔC , having subtracted the background phonon contribution as described in the main text, together with the in-plane susceptibility χ_{ab} (left axis) and the derivative $d(\chi T)/dT$ (arb. units). In the lower panels, absolute values of the in-plane resistivity ρ_{ab} (left axis) are shown together with the Hall coefficient R_H (right axis) and the derivative $-d\rho/dT$ (arb units). Vertical dotted lines mark successive phase transitions, evident in all four physical properties.

these transitions for the undoped and two lightly doped samples. It is evident that the single sharp downturn in BaFe_2As_2 becomes two successive sharp changes in slope in the resistivity of the lightly doped $\text{Ba}(\text{Fe}_{1-x}\text{Co}_x)_2\text{As}_2$. As for the heat capacity, the single sharp first-order peak observed for undoped BaFe_2As_2 , becomes two distinct features, resembling a second order-like step followed by a lower temperature peak, reminiscent of a broadened first-order transition.

To further investigate the apparent splitting of the structural/magnetic phase transitions, magnetic susceptibility and Hall coefficient data were also measured. Results are shown in Fig 2.5 for two representative Co concentrations. Significantly, both measurements indicate the presence of two distinct phase transitions for $x > 0$

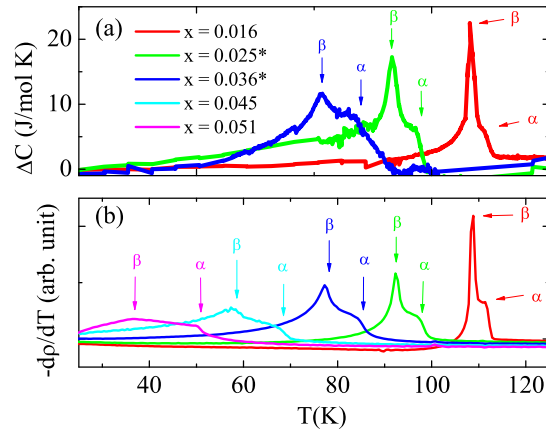


Figure 2.6: Progression of the two successive phase transitions, marked as α and β , as a function of Co concentration as observed in (a) heat capacity and (b) the derivative of the resistivity $-d\rho/dT$. Heat capacity data are shown as ΔC , having subtracted the background phonon contribution as described in the main text. Data for $x = 0.025$ and 0.036 have been multiplied by factors of 3 and 5 respectively for clarity.

evidenced by distinct breaks in the slope of each quantity. In the case of the susceptibility, this effect is more clearly apparent as two peaks in the derivative $d(\chi T)/dT$ ². These data can be compared with the heat capacity measurements (right axis of the upper panels), where we have explicitly subtracted the normal state heat capacity of the optimal doped $\text{Ba}(\text{Fe}_{1-x}\text{Co}_x)_2\text{As}_2$ with $x = 0.061$ as described above, to provide an estimate of the contribution to the heat capacity arising from the two phase transitions. The background subtracted heat capacity is in excellent agreement with the derivative $d(\chi T)/dT$ of the susceptibility, which is proportional to the heat capacity near a second-order phase transition[52]. These data are also in excellent agreement with the derivative of the resistivity $d\rho/dT$. In short, all four measurements indicate unambiguously the presence of two distinct phase transitions. It is very unlikely that this splitting arises from Co inhomogeneity, which in its simplest form would cause a continuous broadening rather than a distinct splitting of the two phase transitions. Indeed, the presence of Co inhomogeneity can be inferred from the broadening of each of these two phase transitions (Fig. 2.6), but this effect remains less than the actual splitting.

Although the magnitude of the heat capacity anomalies associated with these two phase transitions is rapidly suppressed for $x > 0.036$, nevertheless the close correspondence between the heat capacity and the resistivity derivative can be used to follow these phase transitions to even higher Co concentrations. Data for Co concentrations up to $x = 0.051$ are shown in Figure 2.6. As can be seen, both transitions, marked as α and β , are broadened with increasing Co concentration, but the two specific features which can be associated with the critical temperatures for $x = 0.016, 0.025$ and 0.036 remain visible in the resistivity derivative even for $x = 0.045$ and 0.051 . For larger values of the Co concentration, no phase transitions are evident above T_c .

Based on the measurements described above, we can establish a composition-temperature ($x - T$) phase diagram for $\text{Ba}(\text{Fe}_{1-x}\text{Co}_x)_2\text{As}_2$, shown in Fig. 2.7. Phase boundaries delineate the successive phase transitions T_α, T_β and T_c as described above.

²Susceptibility data were smoothed using a linear interpolation and adjacent points averaging before taking the derivative.

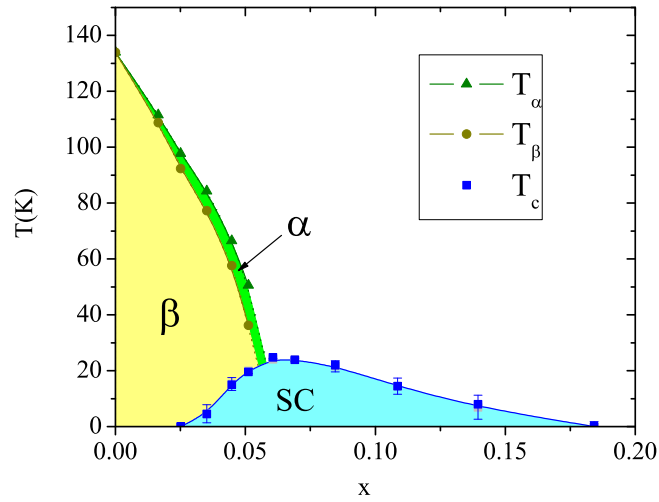


Figure 2.7: Phase diagram for $\text{Ba}(\text{Fe}_{1-x}\text{Co}_x)_2\text{As}_2$ showing the suppression of the two successive phase transitions α and β with increasing Co concentration, and the eventual superconducting (SC) "dome". Data points for T_α and T_β were obtained from heat capacity, resistivity, Hall coefficient and susceptibility data for $x = 0, 0.016, 0.025$ and 0.036 , and from resistivity data alone for $x = 0.045$ and 0.051 . Superconducting T_c values were obtained from resistivity data. Error bars indicate 10 and 90% of the resistive transition. Uncertainty in the Co concentration corresponds to less than the width of the data markers.

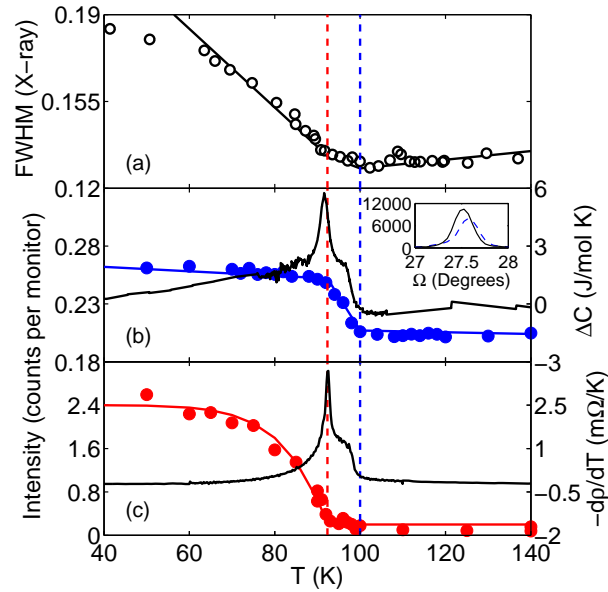


Figure 2.8: Identification of the phase transitions in $\text{Ba}(\text{Fe}_{1-x}\text{Co}_x)_2\text{As}_2$ ($x = 0.025$) (a) T dependence of the $[1\ 1\ 2]_T$ powder line determined from x-ray diffraction. (b) T dependence of integrated intensity (blue circles) of the $[1\ 1\ 2]_T$ nuclear peak determined from $\omega - 2\theta$ scans. Inset shows the Bragg profile $T = 10\text{K}$ and 120K . The solid black line is the heat capacity. (c) T dependence of the integrated intensity (red circles) of the magnetic $[1/2\ 1/2\ 1]_T$ Bragg peak. Solid line is $-d\rho/dT$ (Figure reproduced from ref.[2])

In analogy to the oxy-pnictide CeFeAsO [53] it is tempting to speculate that the upper transition T_α corresponds to the structural distortion, while the lower transition T_β corresponds to the SDW transition. In order to address this issue, subsequent neutron and x-ray scattering measurements were performed and representative data for $x = 0.025$ are shown in Fig. 2.8[2].

For a tetragonal to orthorhombic structural transition, the tetragonal [1 1 2] Bragg peak splits into two peaks, corresponding to the orthorhombic [1 0 2] and [0 1 2] Bragg peaks. Close to the phase transition when the splitting might be too small to resolve, however the orthorhombicity of the lattice can still be track by the full width half max of the original tetragonal [1 1 2] peak. As shown in Fig. 2.8, it can be clearly seen that the broadening of tetragonal [1 1 2] Bragg peak onsets at T_α . On the other hand, the intensity of [1/2 1/2 1] magnetic Bragg peak measured by neutron scattering indicates the antiferromagnetically ordered moments, which onsets at T_β . The results of scattering measurements indeed confirmed that the upper transition is the structural transition and the lower transition is the magnetic transition. Same conclusion was also drawn from the measurements performed by other research group[27].

The apparent coexistence of superconductivity with the broken symmetry states on the underdoped side of the phase diagram raises the question of whether there is macroscopic phase separation associated with a variation in the Co concentration. For length scales above one micron this can be ruled out based on the microprobe analysis. Specifically, the standard deviation in the cobalt doping is much smaller than the range across which we observed this coexistence. From a materials viewpoint it would also be surprising to find Co inhomogeneity on shorter length scales given the large solid solubility. This does not, however, rule out the intriguing possibility of a spontaneous phase separation in an otherwise homogeneous material. In this regard susceptibility measurements provide some insight.

Susceptibility data were taken for representative Co concentrations on the underdoped and overdoped side of the phase diagram, as well as for an optimally doped sample. These measurements were made for applied fields of 50 Oe, oriented in the *ab*-plane, for both zero-field cooling and field cooling cycles. The measurements were

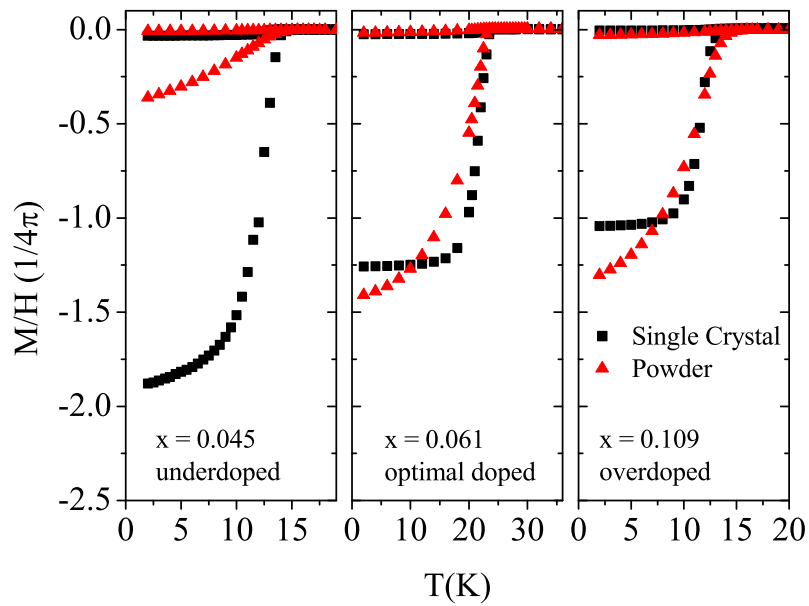


Figure 2.9: Temperature dependence of susceptibility following zero-field cooling (zfc) and field cooling (fc) cycles, for both single crystal and powdered samples for three representative Co concentrations corresponding to $x = 0.045$ (underdoped), $x = 0.061$ (optimally doped) and $x = 0.109$ (overdoped). Measurements were made in a field of 50 Oe applied parallel to the ab -plane of the single crystals.

then repeated for each sample after grinding to a fine powder to examine the role of screening currents. The results of these measurements are shown in Fig 2.9. First we consider the single crystal data (black data points). Field cooled values are relatively small for each Co concentration, indicative of substantial flux trapping. However, zero-field cooled values are large for both underdoped, optimally doped and overdoped cases indicating the presence of significant screening currents. These values do not change substantially when the single crystals are ground to fine powders (red data points) for the optimally doped and overdoped cases, but significantly the underdoped material has a substantially smaller value for the zfc susceptibility. It is clear that the underdoped material is still a bulk superconductor. However, the ability of the underdoped material to support screening currents is significantly reduced by powdering. This effect might be related to the carrier concentration. Specifically, the superfluid density will presumably be smaller for the underdoped material given the coexistence with the SDW state, leading to larger values for the penetration depth. In this case, it is possible that some fraction of the grains in the finely powdered sample will have a size smaller than the penetration depth, reducing the zfc susceptibility. Equally, it is possible that powdering causes significant damage to the surface of the resulting grains. The asymmetry of the superconducting dome might then lead to a stronger suppression of superconductivity for underdoped relative to overdoped samples. Most intriguingly, the lower zfc susceptibility might also reflect the presence of intrinsic inhomogeneity on the underdoped side of the phase diagram, because the percolating shielding currents do not encompass the entire sample. The current measurements are not sufficient to determine the origin of this rather dramatic effect on the susceptibility. Nevertheless, it is clear that there is a substantial volume fraction even in the underdoped region of the phase diagram, but that the superconductivity is to some extent more fragile, at least to the effect of powdering.

2.5 Discussion

The phase diagram shown in Fig. 2.7 is highly suggestive of a scenario in which the superconductivity is intimately related to the presence of a quantum critical point

associated with the eventual suppression of the structural and magnetic phase transitions. For instance, similar phase diagrams are obtained for $CePd_2Si_2$ [54] and UGe_2 [55], for which antiferromagnetic and ferromagnetic phase transitions respectively can be suppressed by applied pressure, and for which magnetic interactions are believed to be responsible for both superconductivity and also non-Fermi liquid behavior in the vicinity of the QCP. Clearly this needs to be investigated in greater detail. Nevertheless, this observation raises the question of whether a similar mechanism is at work in the hole doped analog $Ba_{1-x}K_xFe_2As_2$, and more broadly for all of the superconducting Fe-pnictides. In the specific case of $BaFe_2As_2$, Co-doping is clearly more effective at suppressing the magnetic/structural transitions than K-doping, but it remains to be determined whether this is related to an asymmetry in the electronic structure or to other possibilities.

After the publication of initial results presented in this chapter, several other studies were reported and further deepened our understanding of this phase diagram. Careful scattering and thermodynamic measurements resolved the separation of magnetic and structural transition by $0.7K$ for as grown parent compound $BaFe_2As_2$. It was discovered that the magnetic transition is first order, and the structural transition is second order with the order parameter strongly coupled to magnetic order parameter. Cobalt substitution not only increases the separation of structural and magnetic transition, but also changes the first order magnetic transition to a second order transition at the concentration $x = 0.02$.

The coexistence region of the phase diagram has also been intensively investigated. For example, x-ray scattering measurements revealed that the orthorhombic lattice distortion decreases for temperatures below T_c . For doping concentration near $x = 0.063$, the orthorhombic structure evolve smoothly back to tetragonal structures, which indicates the broken symmetry states coexist and compete with superconductivity in a microscopic level[56]. The absolute values of superfluid density have also been directly measured by our collaborators using magnetic force microscopy. The results show that the superfluid density falls sharply in the underdoped side of the dome, which is consistent with susceptibility data described above[24].

Finally, the possibility of an antiferromagnetic quantum critical point and its

relation to superconductivity in $\text{Ba}(\text{Fe}_{1-x}\text{Co}_x)_2\text{As}_2$ system has been explored by NMR measurements, in which they found evidence for a correlation between T_c and the strength of (π, π) antiferromagnetic spin fluctuations for the overdoped region[57]. Doiron-Leyraud et. al. also analyzed the temperature dependence of resistivity of overdoped $\text{Ba}(\text{Fe}_{1-x}\text{Co}_x)_2\text{As}_2$, and found the strength of the linear term to scale with the superconducting transition temperature T_c leading to a similar conclusion. The possibility of a structural quantum critical point has recently be studied by Yoshizawa et. al. using shear modulus measurements[58]. In chapter 4, I will discuss the fluctuations associated with structural transition in the context of electronic nematic phase transition.

Chapter 3

In-Plane Resistivity Anisotropy of $\text{Ba}(\text{Fe}_{1-x}\text{Co}_x)_2\text{As}_2$

The formation of structural twin domains prevents macroscopic experimental probes from measuring the intrinsic in-plane electronic anisotropy. In this chapter I introduce the techniques to dewtin single crystals of iron pnictides in-situ, and revealed a strikingly large resistivity anisotropy with intriguing doping and temperature dependence. The materials presented in this chapter are published in ref[41, 42]

3.1 Introduction and Motivation

In previous chapter, the phase diagram of $\text{Ba}(\text{Fe}_{1-x}\text{Co}_x)_2\text{As}_2$ has been discussed. One important feature of the phase diagram is that within a specific region above the Neel order transition boundary, the system's C_4 symmetry is broken into C_2 symmetry by structural orthorhombic distortion yet the crystal translational symmetry still preserves. It has been proposed that this structural distortion is driven by an electronic phase transition[28, 30, 29, 59], perhaps due to orbital ordering[?, 32, 31, 60], or fluctuating antiferromagnetism[28, 30]. In both proposals, a large in-plane electronic anisotropy is anticipated in the ‘nematic’ state[61].

One difficulty with probing the in-plane electronic anisotropy of the iron arsenides is that the material naturally forms dense structural twins below the orthorhombic

transition at T_S (Fig. 3.7A,B)[62, 63]. Measurements of twinned samples present only an average of the intrinsic anisotropy, from which little detailed information can be extracted. To overcome this challenge, we have successfully detwinned single crystals of iron pnictides in-situ by either using an in-plane magnetic field or an uni-axial stress. In this chapter we will present the methodology of both techniques, and then focus on the in-plane resistivity anisotropy results obtained by the uni-axial stress experiments.

3.2 Detwinning Single Crystals by a In-plane Magnetic Field

3.2.1 Motivation

In 2002, Lavrov and coworkers performed a series of magnetotransport measurements accompanied by direct optical imaging on lightly doped $La_{2-x}Sr_xCuO_4$ which has an orthorhombic transition around 450K, showing that it can be detwinned by a 14T magnetic field [64]. Encouraged by this result, we have explored the possibility of affecting the structural/magnetic domains of iron pnictides in a similar manner, choosing Co-doped $BaFe_2As_2$ as a starting point. In this section, we show via a combination of angle-dependent magnetoresistance(MR) measurements and direct optical images how magnetic fields can be used to partially detwin underdoped $Ba(Fe_{1-x}Co_x)_2As_2$.

3.2.2 Experimental Methods

Single crystals of $Ba(Fe_{1-x}Co_x)_2As_2$ were grown from a self flux, as described previously. Electrical contacts were made in a standard four-point configuration, with current contacts across the ends of the crystal, and voltage contacts on the exposed (001) surface. Angle-dependent magnetotransport measurements were made in fields up to 14T. All the measurements were performed with both current and

field parallel to the FeAs plane. Samples were cut into bar shapes of typical dimension $1\text{mm}\times 0.2\text{mm}\times 0.05\text{mm}$ and the crystal axes determined by x-ray diffraction¹. Except for the first set of experiments shown in Fig 3.1, for which we deliberately varied the current orientation, all the measurements were taken with current along the orthorhombic a/b direction. Optical measurements were performed in a superconducting magnet cryostat, in which the field could be varied between 0 and 10T. The sample was illuminated with linearly polarized light, and viewed through an almost fully crossed polarizer in order to maximize the contrast of birefringence between neighboring domains. An aspheric objective lens with a numerical aperture (NA) = 0.68 was placed inside the cryostat to focus polarized lights onto the sample. The sample was positioned inside the cryostat using piezo-electric slip-stick positioners, and mounted in an identical manner for both transport and optical measurements in such a way as to minimize external stress.

3.2.3 Results

For the first set of experiments, samples of $\text{Ba}(\text{Fe}_{1-x}\text{Co}_x)_2\text{As}_2$ were cut such that the direction of the current varied with respect to the crystal axes. Representative data are shown in fig. 3.1 for $x=2.5\%$ with current running along the orthorhombic [100] and [010] direction (sample A) and along the orthorhombic [110] direction (sample B). The configuration is illustrated schematically below each panel. At 84K, which is below both the structural and magnetic transitions for this cobalt concentration ($T_S=99\pm 0.5\text{K}$ and $T_N=93\pm 0.5\text{K}$ respectively[2]), we applied 14T and rotated the field within the FeAs plane to measure the resistivity as a function of angle. The angle-dependent MR of sample A is shown in the polar plot fig. 3.1(a). It has a two-fold symmetry (as reported previously by Wang *et al.*[50]), with a positive MR for fields aligned parallel to the current, and negative when the field is perpendicular to the current. The angle dependent MR of sample B is shown in the polar plot fig. 3.1(b). It also has a two-fold symmetry, but the magnitude is much smaller and the angle is shifted by 45 degrees. Clearly the two-fold MR is tied to the crystal axes and not to

¹The susceptibility of $\text{Ba}(\text{Fe}_{1-x}\text{Co}_x)_2\text{As}_2$ is typically very small ($\sim 10^{-3}$ emu/mol), therefore the difference in demagnetization along different directions is negligible.

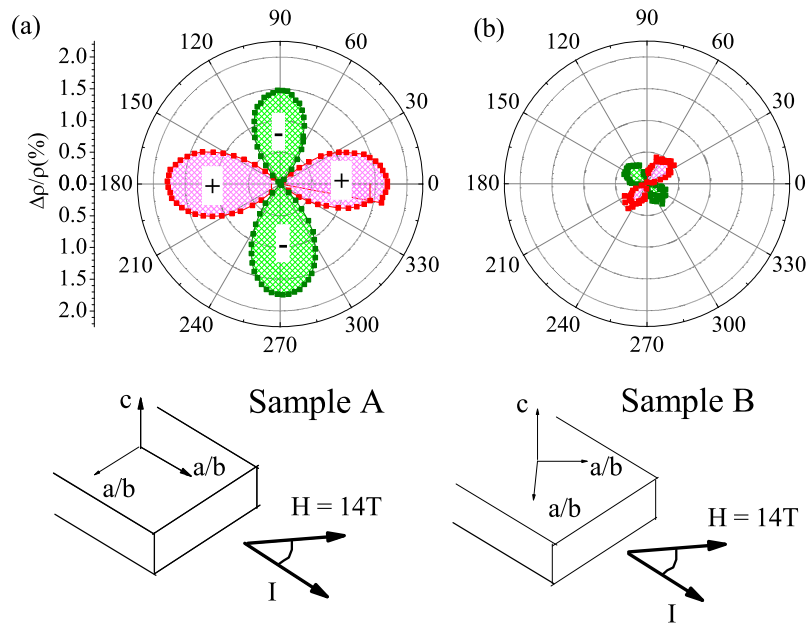


Figure 3.1: The in-plane magnetoresistance $\Delta\rho_{ab}/\rho_{ab}$ (%) of $Ba(Fe_{1-x}Co_x)_2As_2$ for $x = 2.5\%$ for two specific current orientations (sample A and B). The angle independent part of the magnetoresistance for sample B has been subtracted for clarity. The data were taken at 84K, below both T_S and T_N for this cobalt concentration. The geometry of the measurement is indicated below each panel. Both current and field are in the ab -plane, and the angle of the magnetic field is measured relative to the current direction. For sample A current is applied parallel to the orthorhombic a/b axis, whereas for sample B current is applied at 45 degree to the orthorhombic a/b axis.

3.2. DETWINNING SINGLE CRYSTALS BY A IN-PLANE MAGNETIC FIELD²⁹

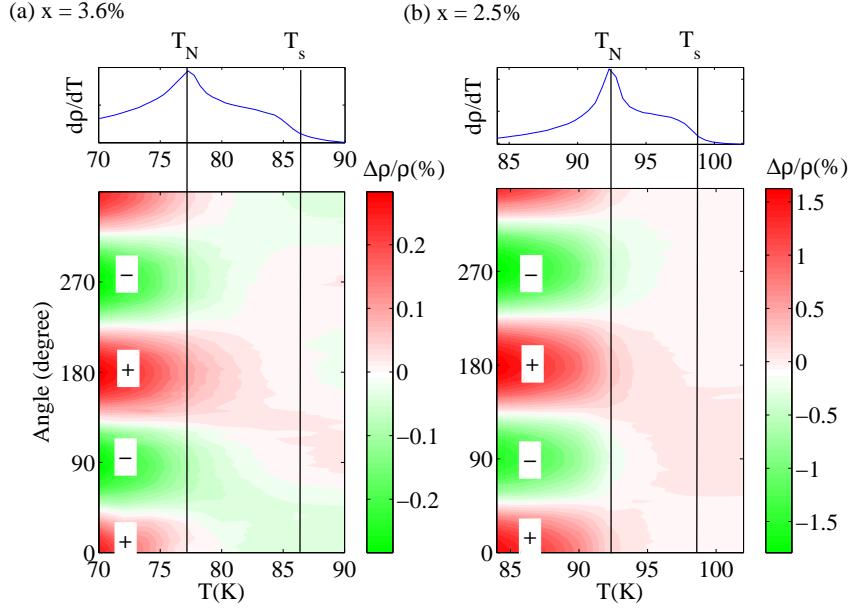


Figure 3.2: (Color online) The angle dependent magnetoresistance ($\rho_{ab}(\theta, 14T) - \overline{\rho_{ab}}/\overline{\rho_{ab}}$) (where $\overline{\rho_{ab}}$ is the average of $\rho_{ab}(\theta, 14T)$ over θ) as a function of angle and temperature of $\text{Ba}(\text{Fe}_{1-x}\text{Co}_x)_2\text{As}_2$ for (a) $x = 3.6\%$ and (b) $x = 2.5\%$. The magnitude of MR is indicated by the color scale. Vertical lines indicate T_S and T_N as determined for these samples by the derivative of the resistivity (shown above each panel).

the current orientation.

To investigate the origin of this angle-dependent MR, we performed a detailed temperature dependent map close to the magnetic and structural transition temperatures. Representative data for $x = 2.5\%$ and 3.6% , in a 14T magnetic field and using the “Sample A” configuration (i.e. current along orthorhombic a/b axis) are shown in Fig.3.2. These data are shown together with the temperature derivative of resistivity, which can be used to determine the two transition temperatures [2][27]. The magnitude of the two-fold MR clearly rises sharply as the samples are cooled below T_N , although a very weak signal is visible up to almost T_S for the higher cobalt concentrations.²

²Variation in the absolute value of the MR for different samples with the same Co concentration indicates that the extent of the partial detwinning effect that we observe depends sensitively on extrinsic parameters, including strain. Consequently, we do not associate any significance to the

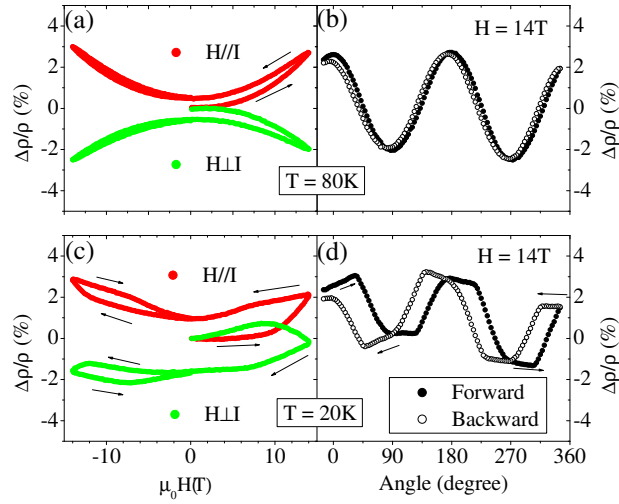


Figure 3.3: Representative magnetoresistance data for $\text{Ba}(\text{Fe}_{1-x}\text{Co}_x)_2\text{As}_2$ as a function of field and angle for $x = 1.6\%$ at $T = 80\text{K}$ (panels (a) and (b)) and $T = 20\text{K}$ (panels (c) and (d)). For all cases the current is aligned parallel to orthorhombic a/b axes and field is applied parallel to the ab plane (i.e. sample A configuration). For field sweeps, the magnetic field was swept from 0 to 14T, then 14 to -14T, then back to 0T following an initial zero-field cool. Data were taken for fields aligned parallel (red) and perpendicular (green) to the current. Angle sweeps were performed in a field of 14T following an initial zero-field cool. Data were taken continuously as the angle was increased from 0 to 360 degrees and then back to zero. The nonzero offset in (c) and (d) results from a slight mixing of out of plane field component due to a small sample misalignment.

3.2. DETWINNING SINGLE CRYSTALS BY A IN-PLANE MAGNETIC FIELD 31

To further investigate this effect, MR measurements were performed as a function of angle and field down to even lower temperatures. Representative data for $x = 1.6\%$ are shown in Fig. 3.3. For temperatures close to T_N , the MR follows an almost perfect sinusoidal angle-dependence with minimal hysteresis as the angle between the field and the current is swept from 0 degrees to 360 degrees and back to 0 again (Fig. 3.3(b)). The MR follows a B^2 field dependence for the entire field range, with a slight indication of some small hysteresis as the field is cycled back to zero (Fig. 3.3(a)). Upon cooling to lower temperatures (for instance to 20K, as shown in panels (c) and (d) of Fig. 3.3), the field dependence of the MR develops an apparent threshold behavior, evidenced by a distinct upward (downward) kink in the MR for fields parallel (perpendicular) to the current. The MR also develops a substantial hysteresis. Both effects are also evident in the angle dependence of the MR (Fig. 3.3(d)), which develops distinct shoulders, presumably related to the threshold behavior observed in the field dependence. The absolute value of the MR in 14T is comparable at the two temperatures shown. It is therefore unlikely that the predominant effect arises from orbital motion of the conduction electrons, which is ordinarily suppressed at higher temperatures according to Kohler's rule [65]. Rather, the behavior shown in Fig. 3.3 is indicative of field-driven changes in the sample. The angle dependence implies that the projection of the applied field on to specific crystal orientations must exceed a specific threshold value to induce these changes at low temperatures.

The changes described above appear to be thermally assisted, such that the associated relaxation after the field is cycled to zero is much slower (essentially frozen on laboratory time scales) at lower temperatures, resulting in a larger hysteresis. Evidence supporting this view can be obtained from time-dependent measurements. Figure 3.4 shows resistivity data as a function of time for a sample with $x = 1.6\%$. The sample was cooled from above T_s to 2 K in a field of 14 T (with the field parallel to the current, following the Sample A configuration), at which temperature the field was cycled to zero. The sample was then warmed to various temperatures (data are shown for 5 and 10 K, in Fig 3.4) and the resistivity measured as a function of time. Clear evidence for relaxation is observed, with a relaxation time that grows

difference in the MR between samples with different Co concentrations.

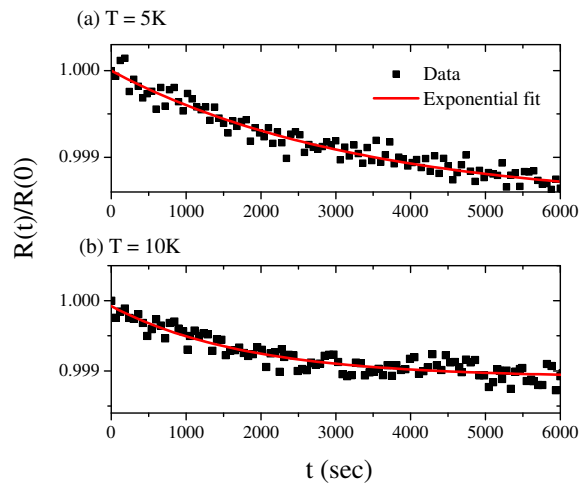


Figure 3.4: Time dependence of the resistivity for a representative sample with $x = 1.6\%$, revealing thermal relaxation of the field-induced changes in the resistivity. The sample was initially cooled to 2 K in 14 T, before the field was cycled to zero. The sample was then warmed to (a) 5 K and (b) 10 K, and the resistivity measured as a function of time after the temperature had stabilized. Data are fit by an exponential relaxation, with resulting time constants of $3.3 \pm 1.8 \times 10^3$ and $1.8 \pm 0.4 \times 10^3$ s respectively.

with decreasing temperature.

In order to maximize the field-induced changes in the resistivity, samples can be cooled through the structural/magnetic transitions in an applied magnetic field. Representative data are shown in Fig. 3.5 for $x = 1.6\%$ and 2.5% for fields applied both parallel and perpendicular to the current (still employing the Sample A configuration). Measurements were taken while cooling in an applied field of 14 T (field cool FC), and then while warming in zero field (zero field warm, ZFW) after cycling the field to zero at base temperature. The resistivity difference induced by field cooling along one orientation can be as large as 5% at low temperature, even after the field is cycled to zero. The FC MR and ZFW resistivity difference for the two field configurations are also plotted in (b) and (d) for the two cobalt concentrations. The sign of MR for the two field orientations is opposite, and the absolute value appears to follow

3.2. DETWINNING SINGLE CRYSTALS BY A IN-PLANE MAGNETIC FIELD 33

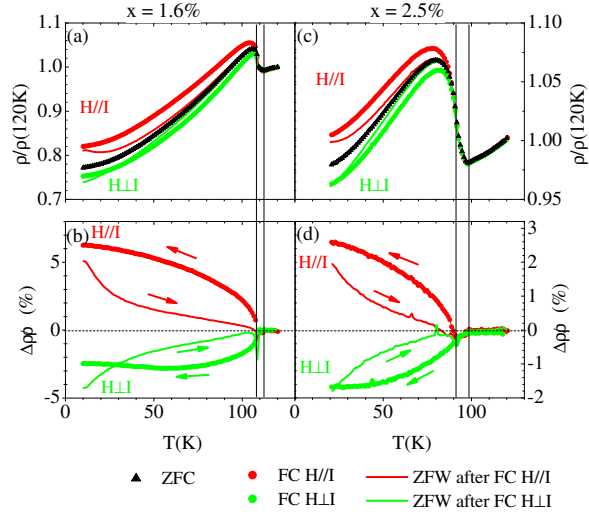


Figure 3.5: Temperature dependence of the resistivity for representative samples with $x = 1.6\%$ (panels (a) and (b)) and $x = 2.5\%$ (panels (c) and (d)). Data were taken during an initial field cool (FC) in 14T, after which the field was cycled to zero and the resistivity measured in zero field while warming (ZFW). The current is aligned parallel to the a/b orthorhombic axes, and the field applied either parallel (red) or perpendicular (green) to the current. For comparison, data are also shown for the same samples while cooled in zero field (ZFC). The FC MR $((\rho_{FC} - \rho_{ZFC})/\rho_{ZFC})$ and ZFW resistivity difference induced by field cooling $((\rho_{ZFW} - \rho_{ZFC})/\rho_{ZFC})$ for the two field configurations are also plotted in (b) for $x = 1.6\%$ and (d) for $x = 2.5\%$. Vertical lines indicate T_S and T_N .

the magnetic order parameter, developing rapidly below T_N . A positive background in the FC MR data can be observed for both orientations, the magnitude of which increases as temperature is decreased, which is likely due to the ordinary metallic MR. In contrast, the resistivity difference of ZFW cycles appears to be rather symmetric. Its magnitude converges rapidly as the temperature is increased, consistent with the thermally assisted relaxation described above, and with the hysteresis effect observed in field sweeps as a function of temperature.

Direct optical measurements were also performed to observe the twinning domains on the surface of $\text{Ba}(\text{Fe}_{1-x}\text{Co}_x)_2\text{As}_2$. Representative images of a 2.5% sample at T

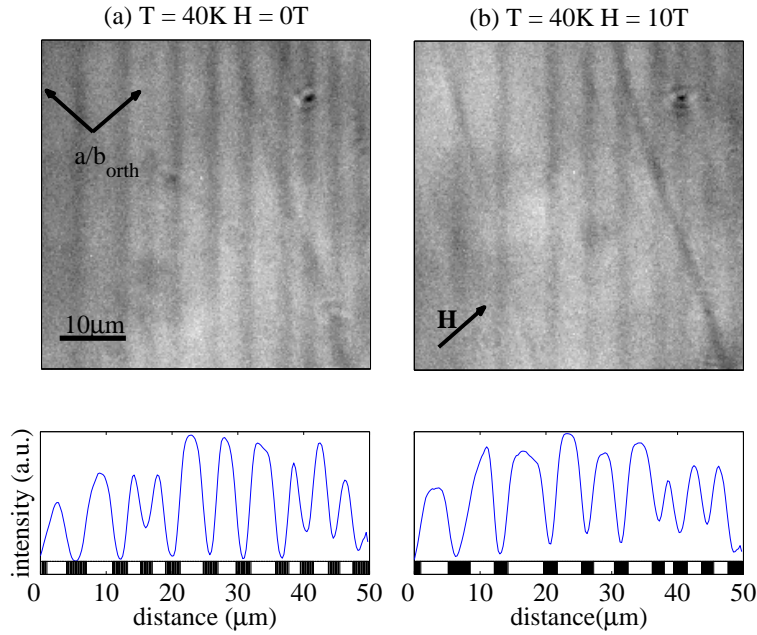


Figure 3.6: Representative optical images of a $\text{Ba}(\text{Fe}_{1-x}\text{Co}_x)_2\text{As}_2$ sample for $x = 2.5\%$, revealing the partial detwinning effect of an in-plane magnetic field. The images (obtained as described in the main text) were taken at $T = 40\text{K}$ below both T_S and T_N . The initial image (a) was taken in zero field, following a zero field cool from above T_N . The field was then swept to 10T , at which field the second image (b) was taken. Horizontal intensity profiles, shown below each image, were calculated by integrating vertically over the image area after background subtraction and noise filtering. Boundaries between domains were estimated as described in the main text, resulting in an estimate of the relative fraction of the two domains indicated by black and white stripes below the figures. The field, which was oriented along the orthorhombic a/b axes, has clearly moved the twin boundaries, favoring one set of twin domains (light) over the other (dark).

= 40K are shown in Fig.3.6. Data were taken in zero field, and also after sweeping to 10 T. The presence of vertical stripes in both images indicates that the sample was twinned in zero and 10 T field. However, the relative density of the two domains is changed by application of the magnetic field. To track the difference of domain distributions, we plot the intensity profile across the boundaries, since the intensity depends on the crystal axes' orientation with respect to the light polarization. The twinning boundaries between two adjacent domains can then be determined from the maximum of the derivative of the intensity, from which we calculate the percentage of the volume of the domains of high intensity ($f = V_b/(V_a + V_b)$). For the two images shown in Fig.3.6, f increases from $54 \pm 1\%$ to $61 \pm 1\%$ a difference $\Delta f = 7\%$ upon application of 10 T. Several regions in the optical images were analyzed, yielding percentage differences Δf ranging from 5% to 15% . Despite the large range in Δf , which is due to the spatial variation of domain distribution, it is always positive, providing convincing evidence for partial field-induced detwinning.

3.2.4 Discussion

The origin of the detwinning effect described above is presumably related to the anisotropic in-plane susceptibility ($\chi_a \neq \chi_b$) that must develop below T_N , and indicates a substantial magnetoelastic coupling. Since the magnetic structure is collinear, with moments oriented along the long a -axis (referred to the orthorhombic unit cell)[2], we can anticipate that $\chi_b > \chi_a$. In this case, fields oriented along the a/b axis of a twinned crystal will favor domains with the b -axis oriented along the field direction. Therefore for currents applied along the a/b axis and fields parallel to the current, the resistivity comprises a larger component of ρ_b than ρ_a . For fields aligned perpendicular to the current the opposite is true. Assuming $\text{Ba}(\text{Fe}_{1-x}\text{Co}_x)_2\text{As}_2$ possesses the generic anisotropic susceptibility of collinear antiferromagnets, the observation of a positive MR for fields aligned parallel to the current, in concert with the relatively small degree of partial detwinning evidenced from optical images, implies a substantial in-plane resistivity anisotropy below T_N with $\rho_a < \rho_b$. This result is consistent with the mechanical detwin experiments described in next section.

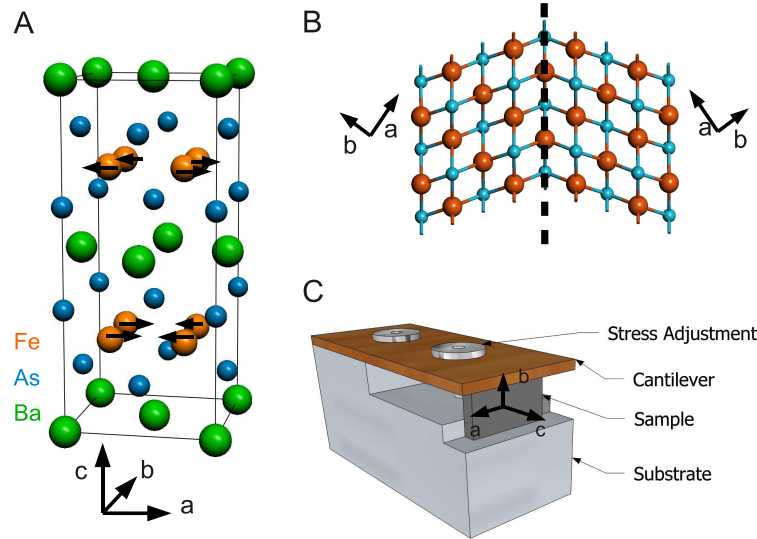


Figure 3.7: (A) Diagram of the crystal structure of $BaFe_2As_2$ in the antiferromagnetic state. The magnetic moments on the iron sites point in the a -direction, and align anti-parallel along the longer a -axis, and parallel along the shorter b -axis. (B) Diagram illustrating a twin boundary between two domains that form on cooling through the structural transition at T_s . Dense twinning in macroscopic crystals obscures any in-plane electronic anisotropy in bulk measurements. (C) Diagram of the device used to detwin single crystals in situ. The sample is held sandwiched between a cantilever and a substrate, with a screw in the center of the cantilever to adjust the uni-axial pressure. The $(0\ 0\ 1)$ surface of the crystal is exposed, enabling transport measurements.

3.3 Detwinning Single Crystals by a Uni-axial Stress

3.3.1 Cantilever Detwinning Device

Single crystals of $Ba(Fe_{1-x}Co_x)_2As_2$ were detwinned in situ using a simple cantilever device. Fig. 3.7C shows a schematic diagram of the device and Fig. 3.8 shows a photograph of a representative crystal held in the device. Crystals were cut such that the orthorhombic a and b axes were aligned parallel to the direction of applied stress. The entire $(0\ 0\ 1)$ face of the crystal is exposed, leaving access for a range of measurements. The beryllium-copper cantilever is fixed at one end, and rests lightly on the side of the crystal, which stands vertically against a supporting edge of the

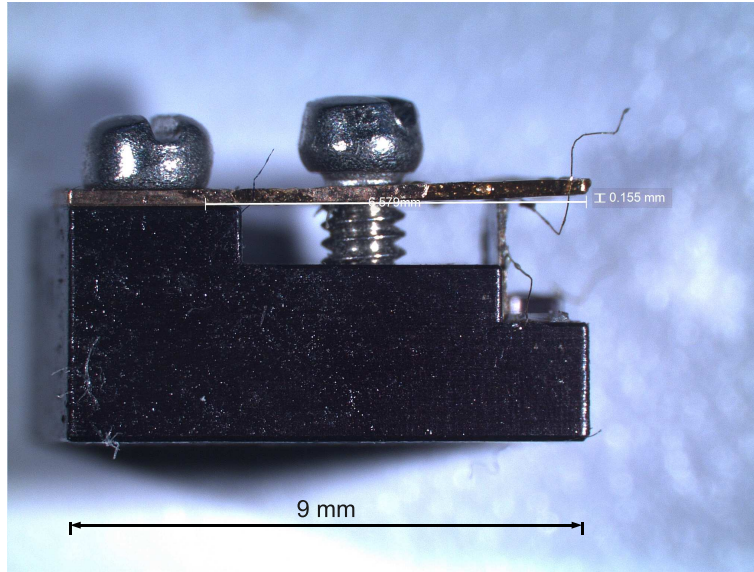


Figure 3.8: Photograph of the device used to detwin single crystals in situ. A representative sample is held sandwiched between a cantilever and a substrate, with a screw in the center of cantilever to adjust the uni-axial pressure. The (0 0 1) surface of the crystal is exposed, enabling transport measurements.

anodized aluminum base. A screw midway along the length of the cantilever enables the downwards force on the crystal to be continuously varied. The deflection of the cantilever can be measured in an optical microscope, allowing a crude estimate of the uni-axial stress. For the example shown in Fig. 3.8 the pressure is approximately 5MPa., small enough that the critical temperature associated with the Neel order (T_N) is unaffected, the device is able to almost fully detwin underdoped crystals, revealing the previously hidden in-plane electronic anisotropy.

3.3.2 Efficacy of the Detwinning Device

Evidence of the efficacy of this method for detwinning can be obtained from high resolution x-ray diffraction measurements. Measurements were carried out on beamline 4-ID-D at the Advanced Photon Source using a focused beam ($\sim 110\mu\text{m}$ and $\sim 200\mu\text{m}$ in the vertical and horizontal directions, respectively) of 20 keV photons in a highly asymmetric reflection geometry. In this geometry the angle of incidence measured

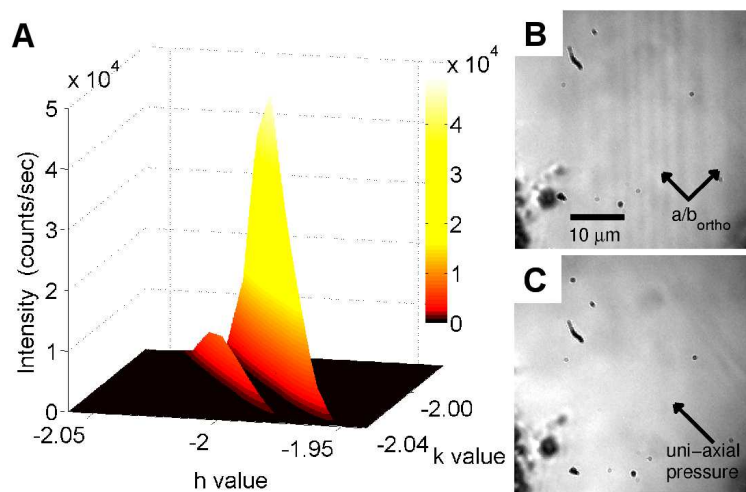


Figure 3.9: (A) Splitting of the $(-2 -2 20)$ Bragg peak (referenced to the tetragonal lattice) at 40 K for a sample with $x = 0.025$ under uni-axial pressure, as revealed by high-resolution x-ray diffraction. The two dimensional surface is formed by interpolating between Gaussian fits to a dense mesh of points from h - k scans. Each peak corresponds to one of the two twin domains. The relative volume fraction of the larger domain, corresponding to the shorter b -axis aligned parallel to the applied stress, is approximately 86% . (B) Polarized-light image of the surface of an unstressed BaFe_2As_2 crystal at 5K without applying uni-axial pressure. Vertical light and dark stripes reveal the existence of twin domains with a and b axes reversed. (C) Polarized-light image on the surface of the same crystal under uni-axial pressure at 5K. The absence of stripes indicates the applied pressure has detwinned the crystal.

from the crystal surface was always kept close to ~ 5 degrees. The use of high energy x-rays guaranteed penetration deep in to the bulk while a near grazing incidence assured illumination of a large area ($> 1 \text{ mm} \times 0.3 \text{ mm}$) of the crystal. Since the crystal size was small ($\sim 2 \text{ mm} \times 2 \text{ mm}$ plate, $< 0.3 \text{ mm}$ thick) the probed volume is representative of the entire crystal.

Data shown in Fig. 3.9A reveal the splitting of the $(-2 -2 20)$ Bragg peak (with respect to the tetragonal lattice) in the orthorhombic state of a crystal with composition $x = 0.025$ held under uni-axial pressure with the cantilever. Note that domain population with the b -axis along the applied stress increases while that of the a -axis

domains decreases. As a result, when the stress direction (horizontal) is orthogonal to the scattering plane (vertical) primarily the a -axis oriented domains are observed. Comparison of the integrated intensity of the two peaks yields a relative volume fraction of 86% of the twin orientation with the shorter b -axis along the applied stress.

Direct optical images were also taken to confirm this result. Optical images were obtained in a cold finger, sample-in-vacuum cryostat. A 0.55 numerical aperture (NA) objective lens outside the cryostat was used for imaging the sample, which was illuminated with broadband, linearly polarized visible ('white') light, with the polarizer aligned approximately 45 degrees to the orthorhombic a/b -axes. The reflected light was analyzed using an almost fully crossed polarizer to maximize the contrast of birefringence between the two twin orientations. Representative images of a BaFe_2As_2 sample surface at 5K are shown for the relaxed cantilever (Fig. 3.9(B)) and strained cantilever (Fig. 3.9(C)). Stripes associated with the twin domains are clearly visible for the unstrained crystal, but these have completely disappeared for the strained sample.

3.4 Stress Dependence Measurement

In order to address the effect of in-plane stress on structural and magnetic transition, the resistivity was systematically measured as a function of the magnitude of the applied stress. Representative results for a sample with 2.5 % Cobalt doping are shown in Fig 3.10. The resistivity was measured for a configuration in which the current was aligned along the uni-axial stress direction, revealing the b -axis resistivity for temperatures below T_s . The magnitude of the applied stress was varied by successively releasing the stress-adjustment screw in the detwinning device by small increments between each measurement. For zero applied stress, two clear features can be seen in the first derivative of the resistivity at 94.5K and 99K which are associated with the SDW and structural transitions respectively. As the stress is progressively increased, the resistivity below the structural transition increases and eventually saturates for a given temperature, indicating that the sample is fully detwinned. The sharp feature associated with the structural transition becomes increasingly broadened as the stress

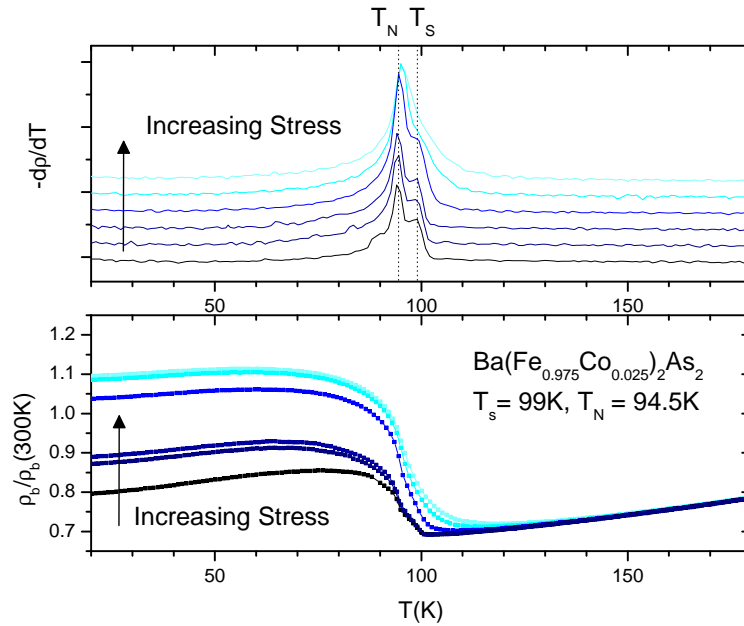


Figure 3.10: Representative data illustrating the variation in the temperature dependence of the b-axis resistivity as a function of the external stress for a sample with 2.5 % Cobalt doping. The magnitude of the stress, which is aligned along the current direction, is tuned as described in the main text. Lower panel shows the resistivity normalized by its room temperature value. Upper panel shows the temperature derivatives of the resistivity (successive data sets are shifted for clarity). The sharp feature associated with the SDW transition is essentially unaffected by the external stress. However, the clear feature observed in the resistivity that is associated with the structural transition for an unstressed crystal is progressively broadened by applied pressure, due to the finite nematic susceptibility above T_S .

is increased, and the resistivity deviates from its zero-stress value at a temperature well above T_S , indicating that the sharp phase transition observed under ambient conditions has been replaced by a cross-over. This behavior is analogous to the case of a ferromagnet cooled through its Curie temperature in a finite external magnetic field, and is indicative of a substantial nematic susceptibility above T_S . In contrast, the sharp feature associated with the SDW transition is essentially unaffected by the applied stress.

3.5 Results of In-Plane Resistivity Anisotropy

Resistivity data were collected for detwinned samples as a function of temperature. Eight representative cobalt concentrations were measured, from the undoped parent compound $x = 0$ through to fully overdoped composition ($x = 0.085$). Representative data for each of these compositions are shown in Fig. 3.11. Measurements were made for currents applied parallel and perpendicular to the applied stress, yielding ρ_b (in red) and ρ_a (in green), respectively.

Inspection of Fig. 3.11 reveals that $\rho_b > \rho_a$ for all underdoped compositions, which is somewhat counterintuitive. Given that the a -axis lattice constant is larger than that of the b -axis, the smaller orbital overlap along the a -axis would ordinarily give rise to a higher resistivity, all else being equal. Equally, the collinear spin arrangement below T_N comprises rows of spins that are arranged ferromagnetically along the b -axis, and antiferromagnetically along the a -axis (Fig. 3.7A). Scattering from spin fluctuations would ordinarily result in a higher resistivity along the antiferromagnetic a -direction. Our observation therefore indicates a more complex situation, and provides a strong constraint for theoretical models of the electronic structure in the orthorhombic state. The degree of in-plane anisotropy can be characterized by the ratio ρ_b/ρ_a , which is shown as a color scale in Fig. 3.12A. The anisotropy varies with temperature and composition, but reaches a maximum value close to two for $0.03 \leq x \leq 0.04$ at low temperatures, in the neighborhood of the beginning of the superconducting dome. In contrast, the overdoped composition $x = 0.085$, which remains tetragonal for all temperatures, reveals no in-plane anisotropy.

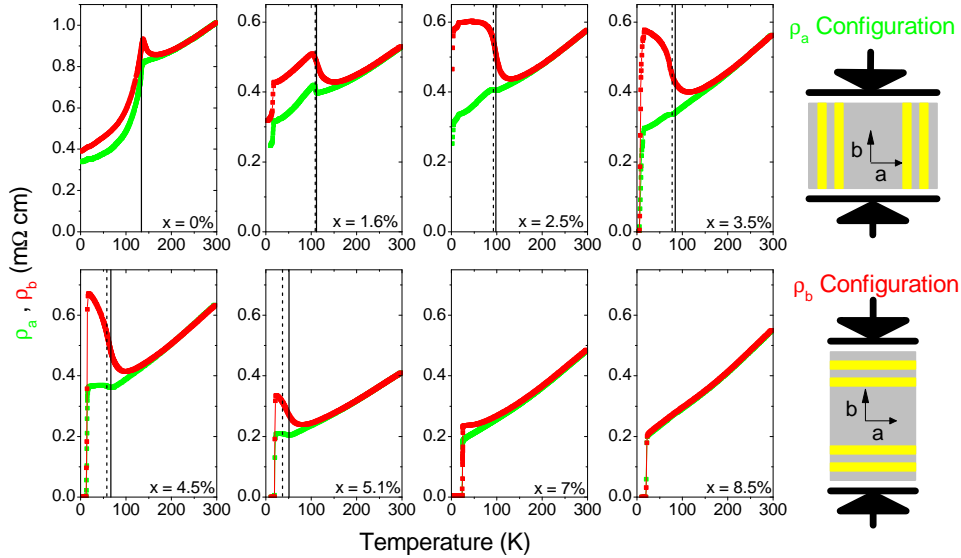


Figure 3.11: Temperature dependence of the in-plane resistivity ρ_a (green) and ρ_b (red) of $\text{Ba}(\text{Fe}_{1-x}\text{Co}_x)_2\text{As}_2$ for Co concentrations from $x = 0$ to 0.085. Solid and dashed vertical lines mark critical temperatures for the structural and magnetic phase transitions T_S and T_N respectively. Values of T_N for stressed samples, obtained from the peak in the derivative of the resistivity, are identical to those found for unstressed samples, indicating that the uni-axial pressure serves as a weak symmetry breaking field to orient twin domains without affecting the bulk magnetic properties. The uni-axial stress does, however, affect the superconducting transitions in some underdoped samples, inducing a partial superconducting transition for $x = 0.016$ and 0.025 , which are not observed for unstressed crystals. Diagrams in the right-hand panel illustrate how measurements of ρ_a and ρ_b were made. Dark arrows indicate the direction in which uni-axial pressure was applied, and smaller arrows indicate the orientation of the a and b crystal axes. In all cases, the same samples and the same contacts (shown in gold for a standard 4-point configuration) were used for both orientations.

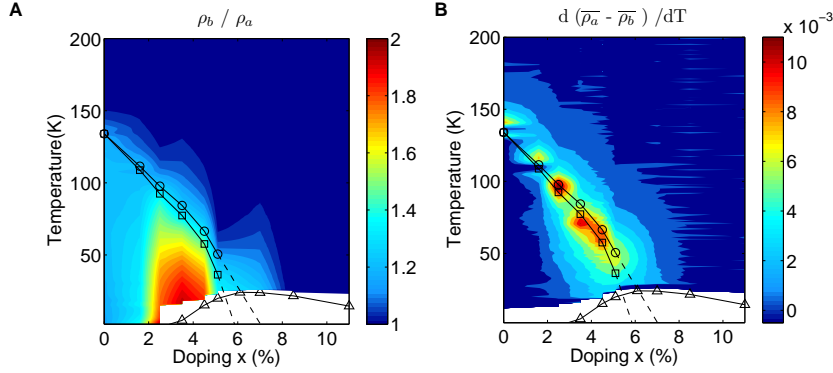


Figure 3.12: **(A)** Evolution of the in-plane resistivity anisotropy as a function of temperature and doping, expressed in terms of the resistivity ratio ρ_b/ρ_a . Structural, magnetic and superconducting critical temperatures, shown as circles, squares and triangles respectively. Significantly, the resistivity ratio deviates from unity at a considerably higher temperature than T_S , indicating that nematic fluctuations extend far above the phase boundary. **(B)** The difference in the temperature derivative of ρ_a and ρ_b ($d(\overline{\rho}_a - \overline{\rho}_b)/dT$, where $\overline{\rho}_a = \rho_a/\rho_a(300K)$, $\overline{\rho}_b = \rho_b/\rho(300K)$) as a function of temperature and doping. The resistivity has been normalized by its room temperature value to avoid uncertainty due to geometric factors. Regions of highest intensity are those regions where ρ_b appears to be insulator-like ($d\rho_b/dT < 0$) while ρ_a remains metallic ($d\rho_a/dT > 0$). This behavior is clearly correlated with the nematic phase between the structural and magnetic transitions.

The temperature dependence of the resistivity (Fig.3.11) is especially striking. At high temperatures, the resistivity is isotropic and starts off as almost linear. For currents running in the b -direction the resistivity deviates from this behavior at a temperature significantly above T_S and increases steeply with decreasing temperature. This insulator-like behavior is cut off near T_N for the lowest doping levels, but extends to much lower temperatures for larger cobalt concentrations. In contrast, for currents flowing in the a direction, the resistivity behaves similarly to a normal metal, continuing to decrease with decreasing temperature over the entire temperature range, except for a small jump near T_N . The superconducting transition at the lowest temperatures causes both ρ_a and ρ_b to drop to zero. The difference of the temperature derivatives of ρ_b and ρ_a (normalized by the room temperature value) shown in Fig. 3.12B, reveals a strong correlation with the orthorhombic distortion.

The composition dependence of the anisotropy in the in-plane resistivity (Fig. 3.12A and B) is in stark contrast to that of the structural anisotropy that develops below T_S . The orthorhombic distortion, characterized by the ratio of in-plane lattice constants, has a maximum value for $x=0$ at low temperature of $(a-b)/(a+b) = 0.36\%$, and decreases monotonically with increasing cobalt concentration[66]; whereas the resistivity anisotropy is a non-monotonic function of doping, exhibiting a maximum near the beginning of the superconducting dome. These contrasting behaviors suggest that the itinerant electrons do not passively follow the lattice distortion. Rather, it appears that the material suffers an underlying electronic phase transition that profoundly affects the low energy excitations near the Fermi level, and in a manner that is much less apparent in the response of the crystal lattice.

Significantly, the resistivity anisotropy is evident for temperatures well above T_S . Even though the crystal symmetry is tetragonal in this temperature range, the uniaxial stress applied by the cantilever breaks the 4-fold symmetry in the basal plane. The external symmetry-breaking field induces a non-zero order parameter above the critical temperature, smoothing the divergent behavior associated with the critical point observed under ambient conditions[67]. The increasing anisotropy for temperatures approaching T_S reveals that the nematic susceptibility is diverging at the critical temperature, providing compelling evidence that the resistivity anisotropy is due to a real phase transition at T_S in the zero stress limit. There is no evidence in either thermodynamic or transport properties for a third phase transition above T_S .

Co-doped BaFe_2As_2 was chosen for this initial study because the structural and magnetic transition are clearly separated in temperature, and the material can be readily tuned in a controlled and reproducible fashion. However, given the rather generic phase diagram found in this family of compounds, it is possible that the observed anisotropy is quite general to underdoped iron-pnictides. For example, recent STM measurements also reveal a significant electronic anisotropy of Co-doped CaFe_2As_2 at low temperatures[68].

Following the research works presented in this chapter, our collaborators have modified the detwinning device and successfully performed optical conductivity and angle resolved photoemission measurements on detwinned single crystals of Co doped

BaFe₂As₂[46, 45, 47]. It was found that the anisotropy persists up to high energy in optical conductivity, and the photoemission data showed a significant splitting of d_{xz} and d_{yz} orbitals in energy.

Resistivity anisotropy measurement has also been extended to the hole doped side of the phase diagram. Surprisingly, the anisotropy was found to be vanishingly small in underdoped Ba_{1-x}K_xFe₂As₂, and even reverse sign, i.e. $\rho_b < \rho_a$, as the doping is increased towards optimal doping[69, 70]. The large in-plane resistivity anisotropy of electron doped compounds and the sign reversal in hole doped compounds have been consistently explained by models based on anisotropic spin fluctuations[71] and orbital order[72].

3.6 c-axis Resistivity

In addition to the in-plane resistivity measurements described previously, we also performed *c*-axis resistivity measurements in order to obtain a complete determination of the temperature-dependence of all of the terms in the resistivity tensor. These data also demonstrate that there is no significant mixing of the *c*-axis resistivity in our in-plane measurements. The temperature dependence of the inter-plane resistivity ρ_c was measured for cobalt concentrations from $x = 0$ to 0.18 using a quasi-Montgomery technique. Representative data are shown in Fig. 3.13 and Fig. 3.14 for underdoped and overdoped samples respectively. Single crystals were cut into slabs with approximate dimensions $(0.3 - 0.6) \times (0.3 - 0.6) \times (0.2 - 0.8) \text{mm}^3$ and large current and voltage pads mounted on the top and the bottom surfaces. The absolute value of the room temperature *c*-axis resistivity ranged from 0.5 - 1.5 m Ωcm , with considerable sample-to-sample variation for any given Co concentration. This variation is a consequence of the relatively small inter-plane anisotropy ($\rho_c/\rho_{ab} < 5$), which makes the aspect ratio of the equivalent isotropic crystal slightly too small to accurately extract the *c*-axis resistivity. (The equivalent isotropic crystal is a hypothetical isotropic crystal which would give the same resistances as those measured for the actual anisotropic sample, and is obtained by multiplying the *c*-axis dimension by the square root of

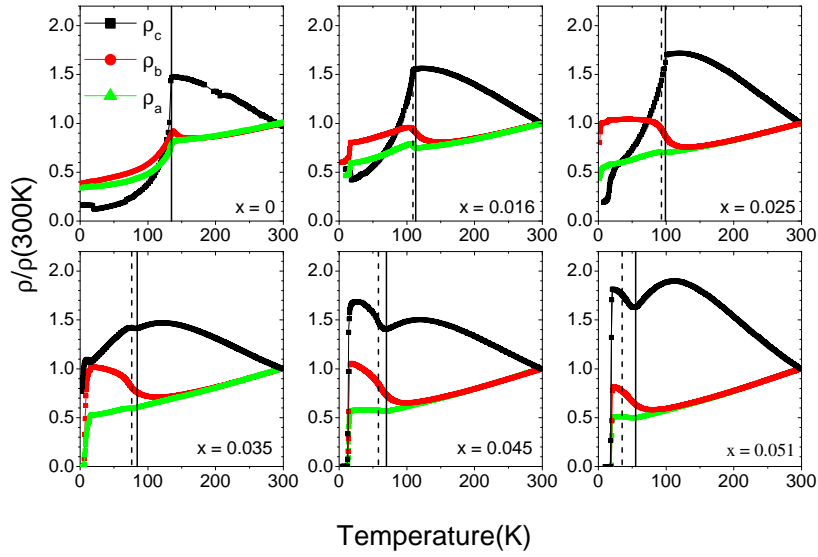


Figure 3.13: Temperature dependence of the inter-plane resistivity ρ_c (black) and in-plane resistivity ρ_b (red) and ρ_a (green) of underdoped $\text{Ba}(\text{Fe}_{1-x}\text{Co}_x)_2\text{As}_2$ for cobalt concentrations from $x = 0$ to 0.051. Data are shown normalized by the room-temperature resistivity $\rho(300\text{K})$ to remove uncertainty in estimates of the absolute value due to geometric factors. Measurements of ρ_a and ρ_b for each composition were made on the same crystal and with the same contacts, as described in previous sections. Measurements of ρ_c were made for separate crystals using a quasi-Montgomery technique.

the resistivity anisotropy. The aspect ratio of the isotropic crystal should ideally approach those of a matchstick sample for a good measurement of the c -axis resistivity.) However, even though we cannot completely eliminate the possibility of in-plane resistivity mixing in these c -axis data due to the above mentioned difficulty, the very different temperature dependence of these data already implies that the actual c -axis resistivity has a different temperature dependence to the in-plane component. Specifically, inspection of the normal state resistivity (above T_S , T_N and T_c), reveals that the c -axis resistivity has a negative temperature gradient at room temperature for all cobalt concentrations. This is in sharp contrast to the in-plane resistivity, which always has a positive temperature gradient at room temperature. Details of the the temperature dependence of the inter-plane resistivity vary slightly from sample to sample for any given Co concentration (for example, the location of the broad maximum of the resistivity in the normal state shows some variation between samples with the same Co concentration, depending on the relative thickness of the crystal measured), which is again due to the above mentioned difficulty, however the overall trend is clear and is in broad agreement with the recent measurements[73].

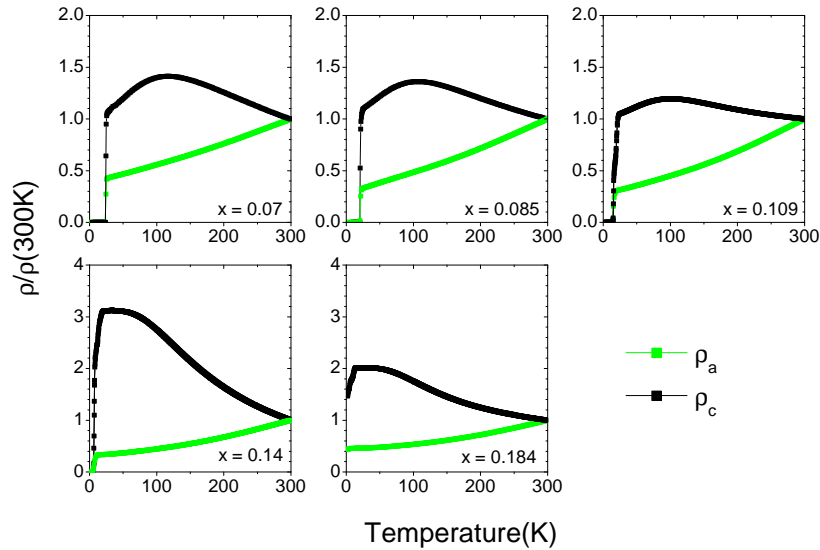


Figure 3.14: Temperature dependence of the inter-plane resistivity ρ_c (black) and in-plane resistivity ρ_a (green) of optimal and overdoped $\text{Ba}(\text{Fe}_{1-x}\text{Co}_x)_2\text{As}_2$ for Cobalt concentration from $x = 0.07$ to 0.184. Data are shown normalized by the room-temperature resistivity $\rho(300\text{K})$ to remove uncertainty in estimates of the absolute value due to geometric factors.

Significantly, based on our c -axis resistivity data, it is clear that there is not any significant c -axis mixing in the in-plane resistivity measurements described in the main article, since this would result in a different temperature dependence up to room temperature, which is not observed. In addition, measurements of the in-plane resistivity for unstressed crystals (performed before and after the pressure dependent experiments) reveal exactly the same temperature dependence as measurements made for thin, long-bar shape twinned crystals, and indeed are the same as previously published data from several different groups, demonstrating that differences in c -axis mixing due to sample geometry are minimal and do not affect any of the in-plane measurements described in this chapter.

Chapter 4

Divergent Nematic Susceptibility Measured by a Tunable Strain

In this chapter I show how measurement of the divergent nematic susceptibility of an iron pnictide superconductor unambiguously distinguishes an electronic nematic phase transition from a simple ferroelastic distortion. These measurements also reveal an electronic nematic quantum phase transition at the composition with optimal superconducting transition temperature. The materials presented in this chapter were published in ref[44].

4.1 Introduction and Motivation

In previous chapter we have described results of resistivity anisotropy of detwinned single crystals of $\text{Ba}(\text{Fe}_{1-x}\text{Co}_x)_2\text{As}_2$. The strikingly large resistivity anisotropy and together with its unusual temperature doping dependence, is highly suggestive of the existence of an electronic nematic phase transition. An electronic nematic phase transition refers to a phase transition in which the electronic system self-organizes with orientational order without forming spatial periodic order[61]. For crystalline systems, such a nematic transition breaks a discrete rotational symmetry of the crystal lattice without altering the existing translational symmetry. However, one of the key doubts accompanied by the experiment described in chapter 3 is that the crystal lattice of

these two systems does not retain a fourfold symmetry, i.e, an orthorhombic structural distortion is always accompanying the rapid increase of resistivity anisotropy, which puts the legitimacy of the term "electronic nematic" into question.

In this chapter I describe measurements of the resistivity anisotropy induced by a tunable uni-axial strain above the phase transition, which exhibits a divergent behaviour as the system approaches the phase transition from the high temperature side. Our result explicitly shows that the structural phase transition in $\text{Ba}(\text{Fe}_{1-x}\text{Co}_x)_2\text{As}_2$ is purely driven by the instability in the electronic part of the free energy, and furthermore reveals an electronic nematic quantum phase transition at the composition with optimal superconducting transition temperature.

4.2 Methodology

4.2.1 In-situ Tunable Strain Applied by Piezo Device

Motivated by previous piezoresistance measurements of quantum Hall systems[74], we developed a similar scheme to apply in-situ tunable strain for single crystal samples of iron based superconductors. As shown in Fig. 4.1(A), by gluing the sample on the side wall of a PZT piezo stack¹ using a standard two part epoxy², strains can be applied by the deformation of the piezo, which is controlled by an applied voltage(V_P). By applying a positive voltage bias through the red and black voltage leads, the piezo stack expands along the long dimension and contracts along the transverse direction. The strain (i.e. the fractional change of length along the current direction, $\epsilon_P = \Delta L/L$) was monitored via a strain gauge³ glued on the back side of the piezo stack. Both ϵ_P and the fractional change of resistivity ($\eta = \Delta\rho/\rho_0$, where ρ_0 is the resistivity of the free standing sample before gluing on the piezo stack) were measured at constant temperature while the applied voltage was swept, as shown in Fig. 4.1(B). The voltage dependence of η and ϵ_P shows hysteretic behaviour due to

¹Part No. PSt 150/557, from Piezomechanik, Munich, Germany.

²Part No. 14250, General Purpose Adhesive Epoxy, from Devcon, U.S.A.

³Part No. WK-XX-062TT-350, General Purpose Strain Gages - Tee Rosette, from Vishay Precision Group.

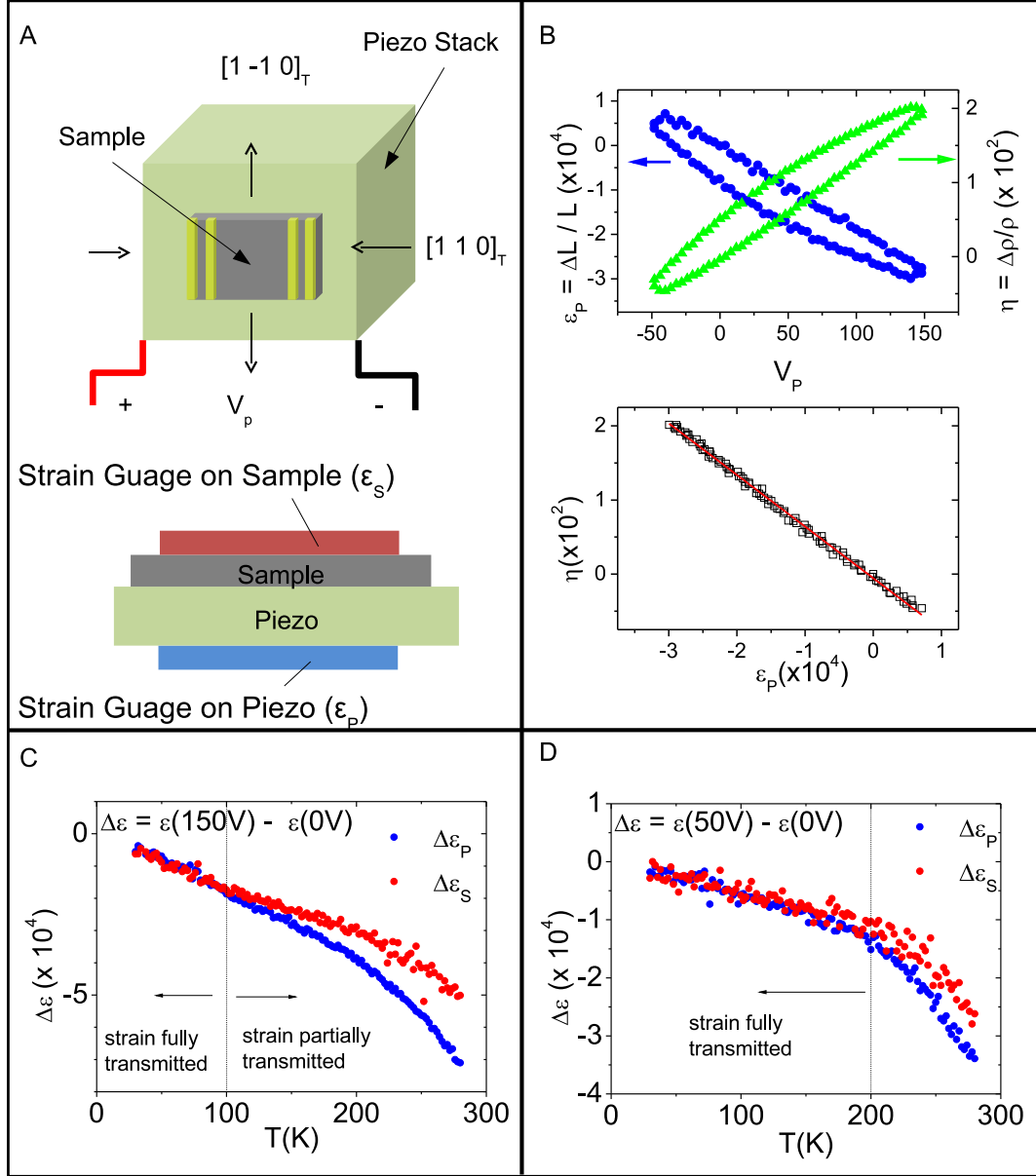


Figure 4.1: **(A)** Schematic diagram of a piezoresistance measurement (upper panel) and of a strain gauge measurement (lower panel). Details about the configuration are described in the supporting online materials. **(B)** (Upper) The relative change of resistivity ($\eta = \Delta\rho/\rho_0$) of a BaFe_2As_2 sample and the strain measured by strain gauge on piezo ($\epsilon_p = \Delta L/L$) as a function of voltage at $T = 140K$. The strain and resistance were measured along the $[1\ 1\ 0]_T$ direction of the crystal. (Lower) Same set of data but η is plotted against ϵ_p . The red line is a linear fit to the data. **(C)** **(D)** The difference of the strain between zero applied voltage and (C) $V_p = 150V$ and (D) $V_p = 50V$. Dash lines indicate the temperatures below which the strain is fully transmitted to the sample. For low voltage this temperature window spans well above T_S for all compositions studied.

the ferroelectric nature of the piezo materials, yet the two quantities exhibit a linear relationship without any hysteresis(Fig. 4.1(B)).

The amount of strain transmitted to the sample (ϵ_S) can be assessed by gluing another strain gauge on the top surface of the crystal, shown schematically in the lower panel of Fig. 4.1(A). The comparison of ϵ_S and ϵ_P for a $\text{Ba}(\text{Fe}_{0.955}\text{Co}_{0.045})_2\text{As}_2$ sample is summarized in Fig 4.1 (C and D). For applied voltages $|V_p| < 150V$, the strain is fully transmitted to the sample for temperatures below approximately 100 K for typical thickness crystals (less than 100 μm). For lower voltages, $|V_p| < 50V$, the strain is fully transmitted to even higher temperatures (Figure 1(D)). The maximum strain that can be applied ($|\epsilon| < 5 \times 10^{-4}$) is substantially less than the lattice distortion developed below the phase transition($10^{-2} \sim 10^{-3}$), and, as we show below, the system is always in the regime of linear response.

4.2.2 Resistivity Anisotropy and Nematic Order

In general, the electronic nematic order parameter can be expressed as a function of the resistivity anisotropy $\psi = (\rho_b - \rho_a)/(\rho_b + \rho_a)$. Taking a Taylor expansion for small values of ψ , the leading term is linear, such that ψ is directly proportional to the electronic nematic order parameter when the order parameter is small. For a strained crystal in the tetragonal state ρ_b and ρ_a refer to the resistivity in directions parallel and perpendicular to the applied compressive stress. As discussed in the previous section, we measure the relative change of the resistivity $\eta = \Delta\rho/\rho_0$ of a strained samples in the tetragonal state. In the absence of strain $\rho_a = \rho_b = \rho_0$. When an infinitesimal amount of strain $\delta\epsilon$ is applied, the resultant ρ_a and ρ_b (here b represents the compressive strain direction) can be expressed as a linear function of $\delta\epsilon$.

$$\rho_a = \rho_0(1 - \alpha\delta\epsilon) \quad (4.1)$$

$$\rho_b = \rho_0(1 + \alpha'\delta\epsilon) \quad (4.2)$$

$$\psi = \frac{\alpha + \alpha'}{2}\delta\epsilon + O(\delta\epsilon^2) \quad (4.3)$$

If α equals α' , it's straight forward to show that $\psi = \eta$, otherwise another proportional factor needs to be introduced in the relationship between these two quantities. If only the leading order term in the expansion of ψ in terms of $\delta\epsilon$ is considered, we then get:

$$\delta\epsilon < 0 \Rightarrow \psi = \frac{\alpha' + \alpha}{2\alpha'}\eta \quad (4.4)$$

$$\delta\epsilon > 0 \Rightarrow \psi = \frac{\alpha' + \alpha}{2\alpha}\eta \quad (4.5)$$

In principle, the resistivity anisotropy will also be affected by acoustic phonon fluctuations associated with the structural transition. However for a $k = 0$ transition the wavelength of such fluctuations is comparable to the sample size, and therefore scattering from such fluctuations makes negligible contribution to the resistivity anisotropy except for extremely close to T_S [75]. To conclude, the relative change of resistivity η along the strain ϵ is a good measure of system's nematic response in a wide range of circumstances.

4.3 Ginzburg-Landau Theory of Electronic Nematic Phase

In the presence of a crystal lattice, an electronic nematic phase transition breaks the crystalline point group rotational symmetry. For example in the case of Co doped BaFe_2As_2 , the C_4 symmetry is lowered to C_2 symmetry. In this particular case we can write down the system's free energy in terms of an expansion of an Ising order parameter ψ ;

$$F = \frac{a}{2}\psi^2 + \frac{b}{4}\psi^4 \quad (4.6)$$

To minimize the free energy one can take the derivative of F with respect to ψ and set it to zero:

$$\frac{\partial F}{\partial \psi} = a\psi + b\psi^3 = 0 \quad (4.7)$$

This equation allows a non-zero solution for $a < 0$ and $b > 0$. Following the usual procedure, we express a by $a_0(T - T^*)$ and set b as a positive constant to model the onset of a finite order parameter at temperature T^* . In the presence of electron-lattice coupling, the non-zero order parameter in the electronic degree of freedom will always induce a finite order parameter in the lattice degree of freedom. In the case of C_4 to C_2 symmetry breaking the lattice order parameter is measured by a orthorhombic strain $\epsilon = (a - b)/(a + b)$. The effect of electron-lattice coupling can be modelled by the following free energy expression:

$$F = \frac{a}{2}\psi^2 + \frac{b}{4}\psi^4 + \frac{c}{2}\epsilon^2 + \frac{d}{4}\epsilon^4 - \lambda\psi\epsilon \quad (4.8)$$

The term $\lambda\psi\epsilon$ indicates that electronic order parameter and lattice order parameters are bilinearly coupled, which is the lowest order coupling allowed by symmetry. We take the derivative of free energy with respect to ψ and with respect to ϵ , and set them to be zero.

$$\frac{\partial F}{\partial \psi} = a\psi + b\psi^3 - \lambda\epsilon = 0 \quad (4.9)$$

$$\frac{\partial F}{\partial \epsilon} = c\epsilon + d\epsilon^3 - \lambda\psi = 0 \quad (4.10)$$

These two equations determine the electronic and lattice order parameters as a function of temperature under the constraint of minimizing the free energy. Substituting for ϵ in equation 4.10 using the expression of $\epsilon = (a\psi + b\psi^3)/\lambda$ obtained from eq. 4.9, we get:

$$\left(a - \frac{\lambda^2}{c}\right)\psi + \left(b + \frac{d\lambda^3}{c\lambda^2}\right)\psi^3 = 0 \quad (4.11)$$

similarly we get

$$\left(c - \frac{\lambda^2}{a}\right)\epsilon + \left(d + \frac{bc^3}{a\lambda^2}\right)\epsilon^3 = 0 \quad (4.12)$$

Equation 4.11 has the same form as equation 4.7, but the coefficients are renormalized due to coupling to the lattice. In essence, the order parameter becomes non-zero at a temperature T_S higher than T^* , where $T_S = T^* + \lambda^2/(a_0c)$. Physically, the lattice provides a polarizable medium, which enhances the nematic instability. We can also look at equation 4.12, which describes the lattice part of the free energy. Due to the coupling to the electronic degree of freedom, the coefficient c , which is the "bare" elastic modulus, is also renormalized to a new effective modulus $c_{eff} = c - \lambda^2/a = c - \lambda^2/(a_0(T - T^*))$. Even though c might always be positive, meaning that there is no instability in the lattice part of the free energy, the effective modulus still goes to zero at T_S , indicating the onset of non-zero spontaneous strain ϵ . Notice that the above derivation is completely reciprocal between the electronic and lattice order parameters – an instability in the lattice degree of freedom will also lead to non-zero electron nematicity below a structural phase transition. Then the question arises, how do we know that the electronic anisotropy in $\text{Ba}(\text{Fe}_{1-x}\text{Co}_x)_2\text{As}_2$ is due to a real electronic nematic phase transition, rather than a parasitic effect of a pure elastic phase transition? A Gedankenexperiment one can do is to put the electrons in an infinitely stiff lattice, i.e. tune the parameter c to infinity. In this scenario if there is really an electronic nematic phase transition, then the lattice will always stay C_4 symmetric while the electronic system will spontaneously break C_4 symmetry at temperature T^* , which can be measured by the resistivity anisotropy. Another approach is to directly measure the bare coefficients a , and determine whether the bare nematic coefficient really becomes zero at some temperature T^* . This measurement can be done by perturbing the system with a symmetry breaking stress, and measuring the quantity $d\psi/d\epsilon$, which is essentially the amount of nematic response at a constant strain. To obtain this result, we introduce stress h , the conjugate field to strain ϵ ,

into the free energy:

$$F = \frac{a}{2}\psi^2 + \frac{b}{4}\psi^4 + \frac{c}{2}\epsilon^2 + \frac{d}{4}\epsilon^4 - \lambda\psi\epsilon - h\epsilon \quad (4.13)$$

The stress breaks the dual symmetry between ψ and ϵ in free energy, because ψ does not couple directly to h . Minimizing this free energy with respect to ψ and ϵ we get a similar set of “equations of motion” for ψ and ϵ :

$$\frac{\partial F}{\partial \psi} = a\psi + b\psi^3 - \lambda\epsilon = 0 \quad (4.14)$$

$$\frac{\partial F}{\partial \epsilon} = c\epsilon + b\epsilon^3 - \lambda\psi - h = 0 \quad (4.15)$$

To see how system responds to stress, we take the derivative of equation 4.14 with respect to h :

$$a\frac{d\psi}{dh} + 3b\psi^2\frac{d\psi}{dh} - \lambda\frac{d\epsilon}{dh} = 0 \quad (4.16)$$

From this we get:

$$\frac{d\psi}{d\epsilon} = \frac{d\psi/dh}{d\epsilon/dh} = \frac{\lambda}{a + 3b\psi^2} \quad (4.17)$$

If we only consider the zero stress limit $h \sim 0$, then $\psi \sim 0$, and the above equation reduces to :

$$\frac{d\psi}{d\epsilon} = \frac{d\psi/dh}{d\epsilon/dh} = \frac{\lambda}{a} \quad (4.18)$$

Therefore if there is truly an electronic nematic phase transition, one should observe a Curie-Weiss diverging behavior of the quantity $d\psi/d\epsilon$ with a critical temperature T^* . This in contrast to the quantity $d\psi/dh$, the nematic response at a constant stress:

$$\frac{d\psi}{dh} = \frac{\lambda}{ac - \lambda^2} \quad (4.19)$$

From this expression, it is clear that the nematic response under a constant stress (eq. 4.19) will show a $1/T$ divergence no matter whether the driving force is a structural or electronic phase transition.

As described in the previous section, our measurement of $d\eta/d\epsilon$ is directly proportional to $d\psi/d\epsilon$. The experiment is equivalent to measuring the temperature dependence of the nematic order parameter at constant strain, as can be appreciated from eq. 4.14. Above T_S we can neglect terms proportional to ψ^3 , leading to $\psi = \lambda\epsilon/a$ and hence $d\psi/d\epsilon = \lambda/a$. Although it is highly unphysical, if we also allow a direct coupling between mechanical stress and the nematic order parameter and include a term $g\lambda\psi$ in the free energy, we obtain:

$$\frac{d\psi}{d\epsilon} = \frac{cg + \lambda}{a + \lambda g} \quad (4.20)$$

The separation of c and a into numerator and denominator still allows us to distinguish the electronic instability from structural, since $d\psi/d\epsilon$ diverges only when a goes to zero. Physically, this distinction is possible because $d\psi/d\epsilon$ is related to the ratio of two thermodynamic quantities. We refer $d\psi/d\epsilon$ as a nematic susceptibility because in the limit that $g = 0$, the strain ϵ is the only field to the nematic order parameter.

4.4 Experimental Results and Analysis

Representative data showing the electronic nematicity (η) as a function of strain (ϵ_P) for a BaFe₂As₂ sample are shown in Fig. 4.2(A) at various temperatures above the structural transition temperature T_S . Data were fit by a straight line in a small range of strain near zero applied voltage. As shown in Fig. 4.2(D), the nematic susceptibility $d\eta/d\epsilon$, which essentially measures the nematic response induced by a constant strain, diverges upon approaching T_S from above. This divergent behavior is reminiscent of the resistivity anisotropy observed above T_S for samples held in a mechanical clamp as described in last chapter. However, as explained in the previous section, there is an important distinction between measurements made under condition of constant stress (mechanical clamp), and constant strain (measurement of $d\eta/d\epsilon$ in the current

set up.) The nematic response under a constant stress (eq. 4.19) will show a $1/T$ divergence no matter whether the driving force is a structural or electronic phase transition. However the nematic response under a constant strain will only diverge when it is a true electronic nematic phase transition (eq. 4.18). In this sense, the divergence in $d\eta/d\epsilon$ shown in Fig. 4.2 is direct evidence that BaFe_2As_2 suffers a true electronic nematic instability, and the structural transition merely passively follows the nematic order.

From Eq. 4.18 $d\psi/d\epsilon = \lambda/a = \lambda/(a_0(T - T^*))$, it is natural to fit the data of $d\eta/d\epsilon$ in Fig. 4.2(B) with a Curie-Weiss temperature dependence. However Eq. 4.18 is only valid in the limit of vanishing strain, at which one can disregard the higher order non-linear terms. In the realistic experiment situation, there is always some intrinsic built in strain even at zero applied voltage due to the different thermal contraction of the sample and the piezo stack. To take into account this built in-strain, we perform a numerical fit based on the following expression:

$$\frac{d\eta}{d\epsilon} = \frac{\lambda}{a_0(T - T^*) + 3b\eta_0^2} \quad (4.21)$$

where η_0 is the induced relative change of resistivity of the sample at zero applied voltage comparing to before it was glued on the piezo. It is a function of temperature and was simultaneously measured when we performed voltage sweep at fix temperature in order to acquire $\eta(\epsilon)$. Data corresponding to the measurement presented in Fig.4.2B is plotted in the inset. A numerical fit was performed based on the following expression:

$$d\eta/d\epsilon = \frac{P_1}{T - P_2 + P_3\eta_0^2} + P_4 \quad (4.22)$$

where $d\eta/d\epsilon$ and η_0 are functions of temperature T , and are simultaneously fitted by four parameters. P_1 , P_2 and P_3 correspond to λ/a_0 , T^* and $3b/a_0$ in the Ginzburg-Landau theory respectively. The contribution due to the built in strain is usually of the order of a few Kelvin, which will only be relevant if T is very close to T^* . $P_4 = \chi_0$

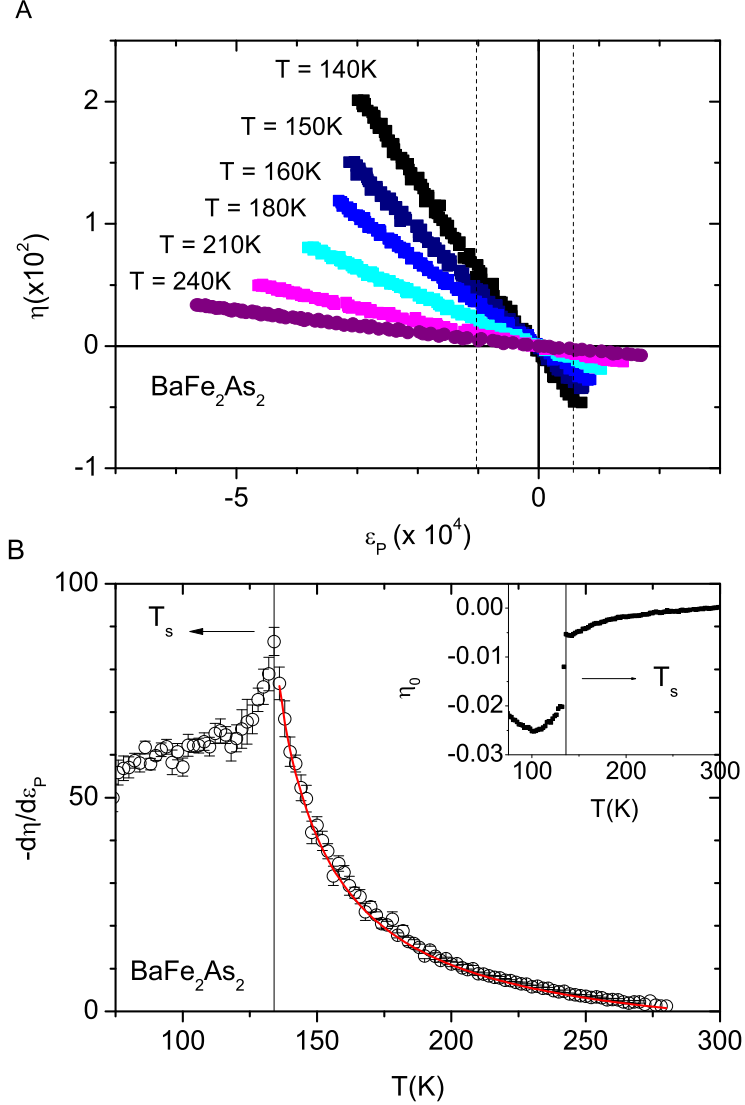


Figure 4.2: **(A)** Representative data for BaFe₂As₂ showing the relative change of resistivity ($\eta = \Delta\rho/\rho_0$) as a function of strain ($\epsilon_P = \Delta L/L$) at several temperatures above T_S . The nematic response was obtained by a linear fit of the data near zero applied voltage ($-5 \times 10^{-5} < \epsilon_p(V) - \epsilon_p(0) < 1 \times 10^{-4}$, indicated by the vertical dashed lines). **(B)** Temperature dependence of the nematic response $d\eta/d\epsilon_P$. Vertical line indicates the structural transition temperature $T_S = 138$ K. Red line shows fit to mean field model, described in the main text.

is a new parameter we introduced to take into account the intrinsic piezoresistive response of metals and semiconductors that occurs due to the induced orthorhombicity even in the absence of nematic fluctuations. The result of this fitting is plotted in Fig.4.2(B) as a solid red curve, which is in excellent agreement with measured data $d\eta/d\epsilon$. The mean field critical temperature T^* obtained from the fitting is $116K$, $22K$ lower than the actual phase transition temperature ($T_S = 138K$), this is expected from the Ginzburg-Landau theory discussed in previous section.

The divergence of $d\eta/d\epsilon$ not only reveals the tendency towards an electronic nematic phase transition, but also measures the strength of nematic fluctuations, according to the fluctuation-dissipation theorem. We have measured $d\eta/d\epsilon$ of $\text{Ba}(\text{Fe}_{1-x}\text{Co}_x)_2\text{As}_2$ samples for doping concentration ranging from the undoped parent compound to overdoped compositions, as shown in Fig.4.3. The magnitude of $d\eta/d\epsilon$ is plotted as a color-map in the composition versus temperature phase diagram in Fig.4.4. For the underdoped part of the phase diagram, $d\eta/d\epsilon$ increases rapidly near the structural phase transition boundary. As the doping concentration increases, the intensity of fluctuations increases, and reaches a maximum near optimal doping concentration, where structural and magnetic transitions are fully suppressed. The nematic fluctuations persist to the overdoped regime, eventually decreasing as the superconducting T_c decreases. The associated softening of the shear modulus has been extensively studied by resonant ultrasound measurements[76, 58].

To quantitatively track the evolution of nematic fluctuations across the phase diagram, numerical fits to the data of $d\eta/d\epsilon$ and η_0 (shown in inset of Fig. 4.3) were performed for each composition based on Eq.4.22. The obtained T^* is also plotted as a function of composition in Fig.4.4. It can be clearly seen that the mean field nematic critical temperature T^* closely tracks the actual structural transition temperature T_S in the underdoped regime, and is suppressed to zero at the optimal doping. T^* becomes negative as the doping further increases beyond optimal doping, indicating a “paranematic” state. Significantly, our experimental data and analysis reveal an electronic nematic quantum phase transition for a composition close to optimal doping. It remains to be seen whether fluctuations associated with this quantum phase

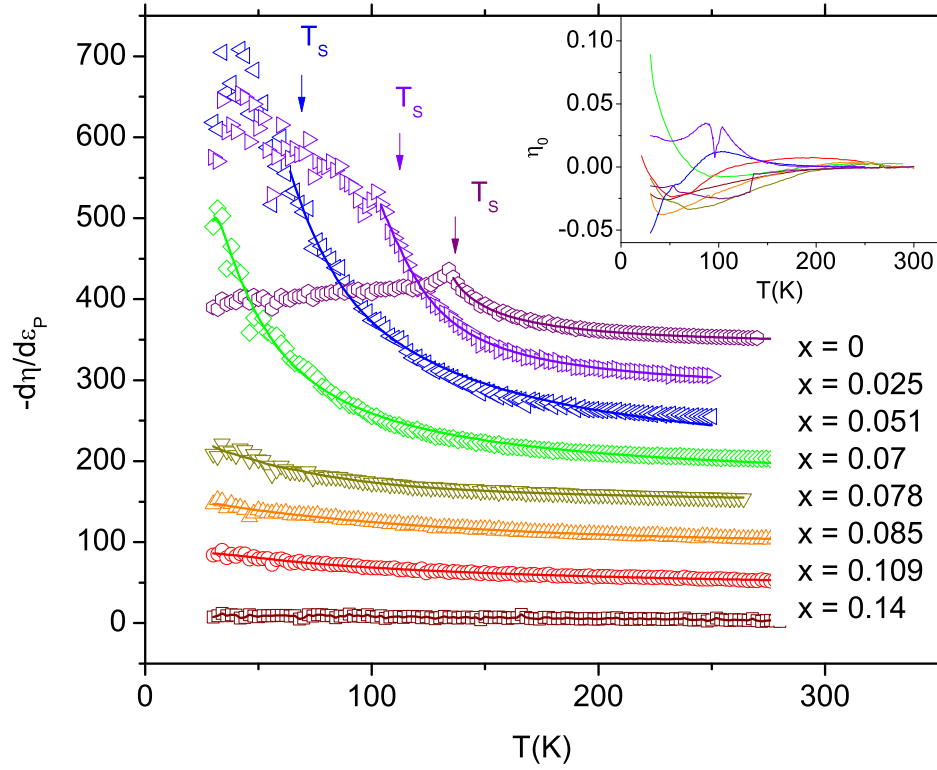


Figure 4.3: Temperature dependence of the nematic susceptibility of $\text{Ba}(\text{Fe}_{1-x}\text{Co}_x)_2\text{As}_2$ for various compositions (open symbols). Successive data sets are offset vertically by 50 for clarity. Solid lines are fits based on a phenomenological Ginzburg-Landau theory, taking into account an intrinsic built-in strain, which is measured by η_0 shown in inset figure.

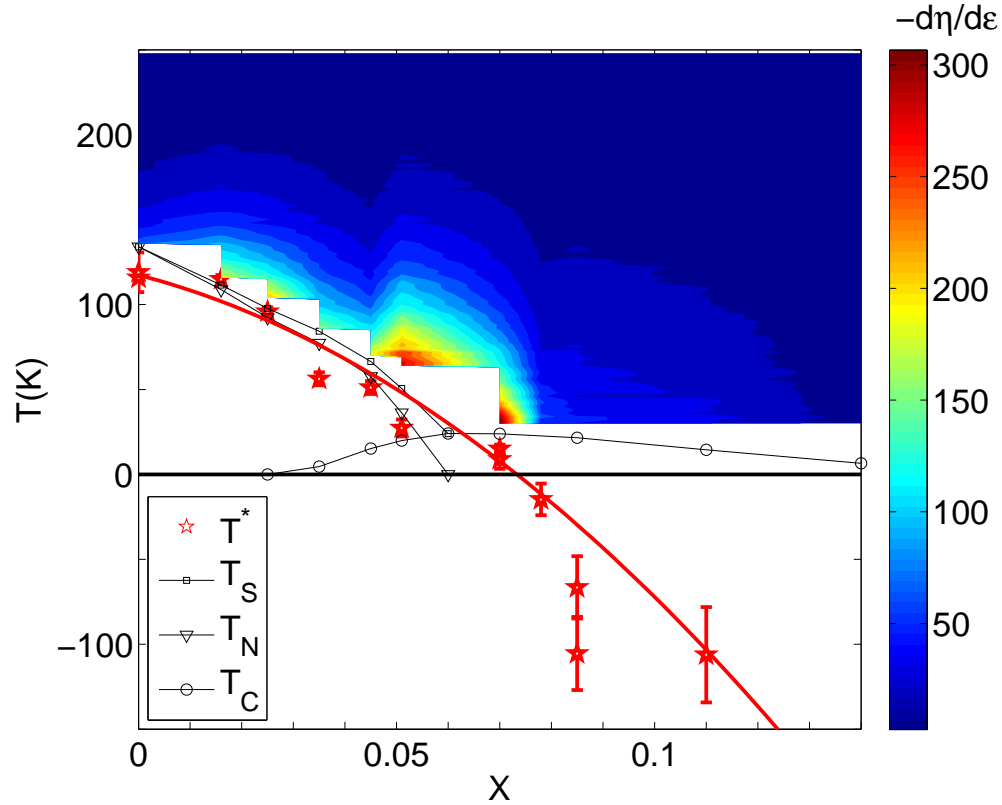


Figure 4.4: Evolution of the nematic susceptibility ($d\eta/d\epsilon$) of $\text{Ba}(\text{Fe}_{1-x}\text{Co}_x)_2\text{As}_2$ as a function of temperature and doping. Structural, magnetic and superconducting transition temperatures (T_S , T_N and T_C) are shown as squares, triangles and circles. The mean field electronic nematic critical temperature (T^*) obtained from the fit to the data in Fig. 4.3 are shown as open red stars. The evolution of nematic susceptibility and nematic critical temperatures clearly indicates an electronic nematic quantum phase transition occurs close to optimal doping.

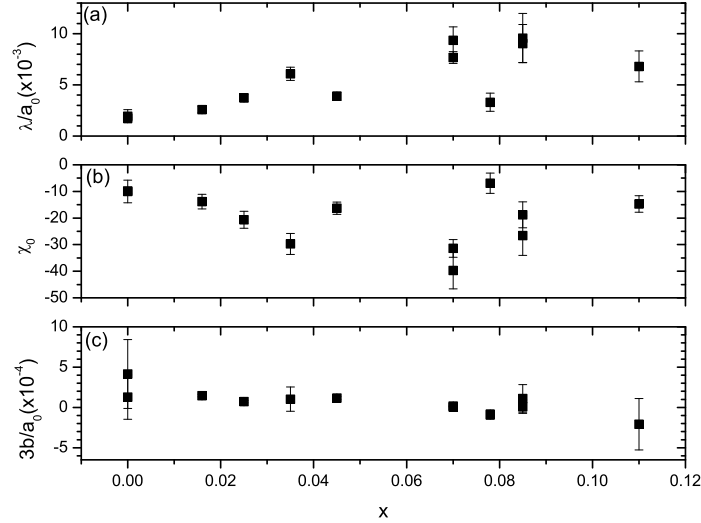


Figure 4.5: Doping dependence of the parameters obtained from the numerical fit based on the Ginzburg-Landau theory.

transition play an important role in enhancing T_c in the superconducting phase. Nevertheless the existence of nematic fluctuations across such a wide temperature and doping range suggests that they are a fundamental ingredient to describe the normal state of the system[76].

The obtained fit parameters other than T^* are shown in Fig. 4.5 as a function of cobalt concentration x . Inspection of Fig. 4.5, also reveals an enhancement of λ/a_0 and χ_0 near optimal doping, which can be consistently explained by an enhancement of electron-lattice coupling λ . The enhancement of λ not only increases λ/a_0 , but also could potentially affect the “background” piezoresistivity effect measured by χ_0 . However the numerical fit also becomes less consistent close to optimal doping (Fig.4.3), which might be due to the effect of quantum critical fluctuations. Finally, the parameter $3b/a_0$ remains mostly constant across underdoped and optimal doped compositions but becomes negative for some overdoped compositions. This might be due to the fact that both $d\eta/d\epsilon$ and η_0 become small for overdoped compounds, which makes the fitting less constrained. On the other hand for the overdoped compounds

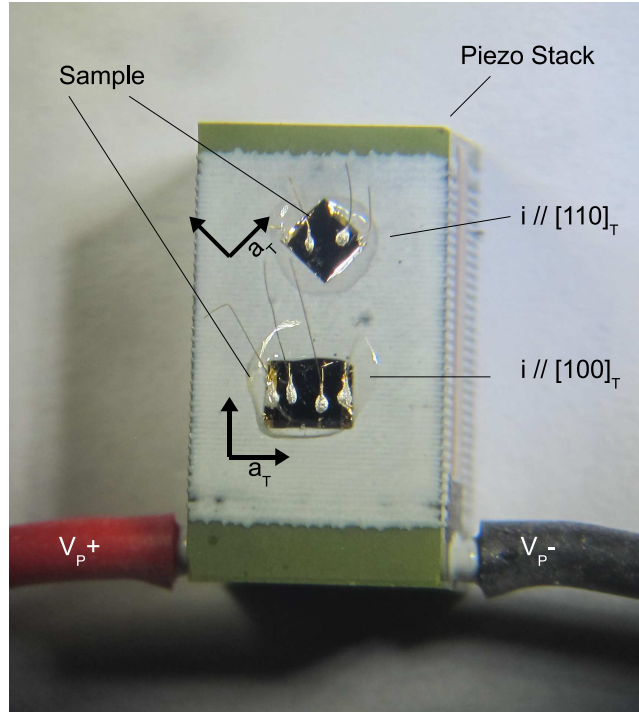


Figure 4.6: Photograph of two representative crystals mounted on a piezo stack used to apply in situ tunable strain. Two samples are mounted, corresponding to $\epsilon // [110]_T$ (upper crystal) and $\epsilon // [100]_T$ (lower crystal). Red/black wires are the positive/negative voltage leads of the piezo. The (0 0 1) surface of the crystal is exposed, enabling transport measurements.

there is no phase transition at finite temperature, and hence the sign of parameter b is less crucial, and higher order coefficients can be introduced to bound the free energy.

4.5 Control Experiment for Different Orientations

For a control experiment, two samples of $\text{Ba}(\text{Fe}_{1-x}\text{Co}_x)_2\text{As}_2$ with $x = 0.065$ (i.e. nearly optimally doped) were measured, one with strain aligned along the tetragonal $[110]$ direction ($\epsilon // [110]_T$) and one aligned along the tetragonal $[100]$ direction ($\epsilon // [100]_T$). The resistivity was always measured along the strain direction. A photograph of the

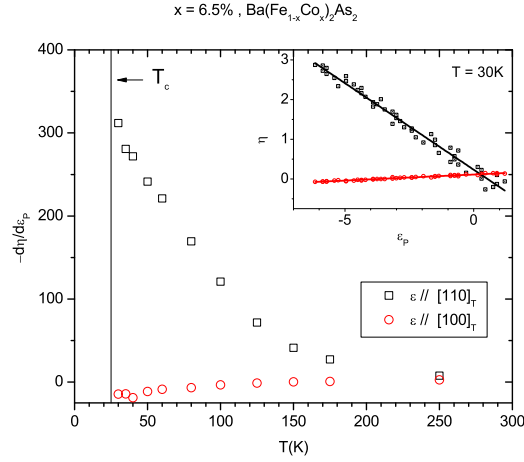


Figure 4.7: Representative data showing the temperature dependence of the nematic response $d\eta/d\epsilon_P$ of $\text{Ba}(\text{Fe}_{0.935}\text{Co}_{0.065})_2\text{As}_2$ samples, for the two configurations shown in fig. S1. Samples were prepared so that the strain and current were aligned along the $[1\ 1\ 0]_T$ (Fe-Fe bonding direction) and $[1\ 0\ 0]_T$ (Fe-As bonding direction), shown as black and red symbols respectively. Vertical line indicates the superconducting critical temperature $T_c = 25\text{K}$ of these optimal doped samples. Inset shows the relative change of resistivity ($\eta = \Delta\rho/\rho_0$) as a function of strain ($\epsilon_P = \Delta L/L$) at $T = 30\text{K}$. Lines show linear fits.

experiment configuration is displayed in Fig. 4.6 and the results are shown in Fig. 4.7. For $\epsilon//[110]_T$ the temperature dependence of $d\eta/d\epsilon$ exhibits a similar divergent behavior to that of the optimal doped sample shown in the main text Fig.4. However, for $\epsilon//[100]_T$ (i.e. at 45 degrees to the orthorhombic direction observed for underdoped compositions) $d\eta/d\epsilon$ has an opposite sign and a much smaller value, and exhibits a much weaker temperature dependence. The significant difference of $d\eta/d\epsilon$ obtained between for the two orientations confirms the following analysis in which the divergent behavior is due to the coupling to nematic fluctuations.

Chapter 5

Non-monotonic Doping Dependence of Resistivity Anisotropy

In this chapter I described magnetotransport measurements of single crystals of Co and Ni doped BaFe_2As_2 , both showing a non-monotonic doping dependence of resistivity anisotropy. Magnetotransport data suggest that the relatively small in-plane anisotropy of the parent compound in the spin density wave state is due to the presence of an isotropic, high mobility pocket of the reconstructed Fermi surface. Progressive suppression of the contribution to the conductivity arising from this isotropic pocket with chemical substitution eventually reveals the underlying in-plane anisotropy associated with the remaining Fermi surface pockets. The materials discussed in this chapter are published in ref[43].

5.1 Introduction and Motivation

In previous chapter, by measurements of resistivity anisotropy induced by a tunable strain above the phase transition, we have established that the orthorhombic structural transition in $\text{Ba}(\text{Fe}_{1-x}\text{Co}_x)_2\text{As}_2$ is truly driven by an electronic nematic phase transition. One important argument is that in-plane resistivity anisotropy is a

good measure of electronic nematic order parameter. However, one puzzling feature revealed by the measurements of detwinned crystals is that at low temperature resistivity anisotropy showing a non-monotonic doping dependence, in striking contrast to the structural order parameter, which diminishes monotonically with increasing cobalt concentration [66]. It raises the question that to what extent does the correspondence between resistivity anisotropy and nematic order parameter hold, and if it breaks down, what is the origin of the breaking down.

The nonmonotonic behavior is not restricted to $\text{Ba}(\text{Fe}_{1-x}\text{Co}_x)_2\text{As}_2$. Here we also present data of the in-plane resistivity anisotropy of the closely related cases of Ni-substituted BaFe_2As_2 . The in-plane resistivity anisotropy, expressed as ρ_b/ρ_a , is shown as a function of temperature and composition in Fig.5.1. In both cases, ρ_b/ρ_a is found to vary non-monotonically with increasing amounts of Ni or Co. For the case of Co substitution, the in-plane anisotropy peaks at a value of nearly 2 for a composition $0.025 < x < 0.045$, close to the onset of the superconducting dome. In comparison, for Ni substitution, ρ_b/ρ_a peaks for $0.012 < x < 0.022$, approximately half the dopant concentration as for Co substitution. In addition, a much weaker secondary maximum is found for $\text{Ba}(\text{Fe}_{1-x}\text{Ni}_x)_2\text{As}_2$ centered at $x \sim 0.03$. Measurements of multiple crystals confirmed the presence of this feature.

In this chapter, we investigate the origin of non-monotonic doping dependence of the in-plane resistivity anisotropy. I will show that for both $\text{Ba}(\text{Fe}_{1-x}\text{Co}_x)_2\text{As}_2$ and $\text{Ba}(\text{Fe}_{1-x}\text{Ni}_x)_2\text{As}_2$, the onset of the large in-plane resistivity anisotropy coincides with a suppression of a large linear term in the magnetoresistance, suggesting a common origin for the two effects. Through the analysis of magnetotransport data, we attribute the origin of these two effects to the presence of an isotropic, high mobility pocket of the reconstructed Fermi surface in the antiferromagnetic state, which dominates the transport of the parent compound and short circuits other more anisotropic Fermi surfaces. Progressive suppression of the contribution to the conductivity arising from this isotropic pocket with chemical substitution eventually reveals the underlying in-plane anisotropy associated with the remaining Fermi surface pockets.

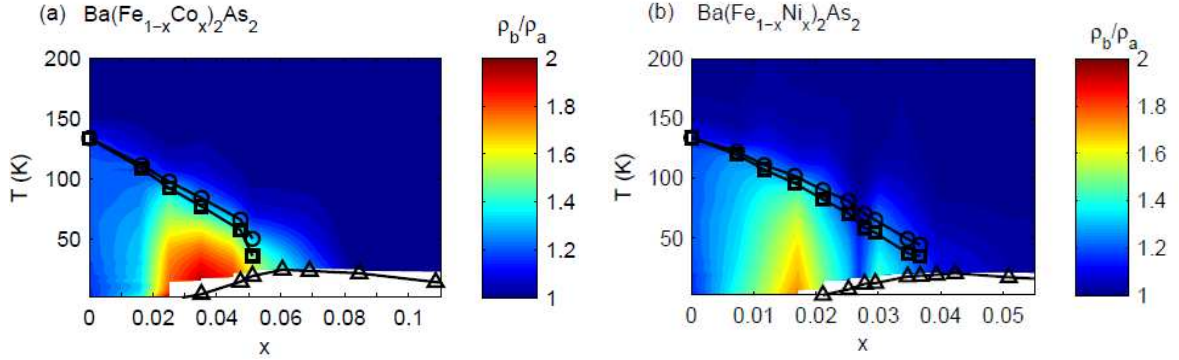


Figure 5.1: In-plane resistivity anisotropy, ρ_b/ρ_a , as a function of temperature and doping for (a) $\text{Ba}(\text{Fe}_{1-x}\text{Co}_x)_2\text{As}_2$ and (b) $\text{Ba}(\text{Fe}_{1-x}\text{Ni}_x)_2\text{As}_2$. The color scale has been obtained by a linear interpolation between adjacent data points. The same scale has been used for all three panels. Black circles, Squares, and triangles indicate T_S , T_N , and T_c respectively, determined for unstressed conditions. T_c for $\text{Ba}(\text{Fe}_{1-x}\text{Co}_x)_2\text{As}_2$ and $\text{Ba}(\text{Fe}_{1-x}\text{Ni}_x)_2\text{As}_2$ was defined by the midpoint of the superconducting transitions. ($\text{Ba}(\text{Fe}_{1-x}\text{Ni}_x)_2\text{As}_2$ data courtesy of Hsueh-Hui Kuo)

5.2 Magnetoresistance and Hall measurements

To investigate the origin of the non-monotonic doping dependence of the in-plane resistivity anisotropy, which is observed for both Co and Ni dopants, magnetotransport measurements were performed at the National High Magnetic Field Laboratory (NHMFL) in Tallahassee in dc magnetic fields up to 35 T and in Stanford in fields up to 14 T. The magnetic field was always oriented along the c -axis and the samples were mounted using a 4-point contact configuration. Measurements were made for both positive and negative field orientations in order to subtract any small resistive component due to contact misalignment.

Transverse (B parallel to c -axis) magnetoresistance (MR, defined as $\Delta\rho/\rho$) has been measured on both detwinned and twinned samples. We first discuss the parent compound, for which representative MR data are shown in Fig.5.2(a) for a temperature of 25 K. As has been previously observed, the MR of the parent compound is linear over a wide field range [77]. This behavior extends to very low fields, at which point the MR naturally reduces to a weak-field quadratic dependence. Interestingly,

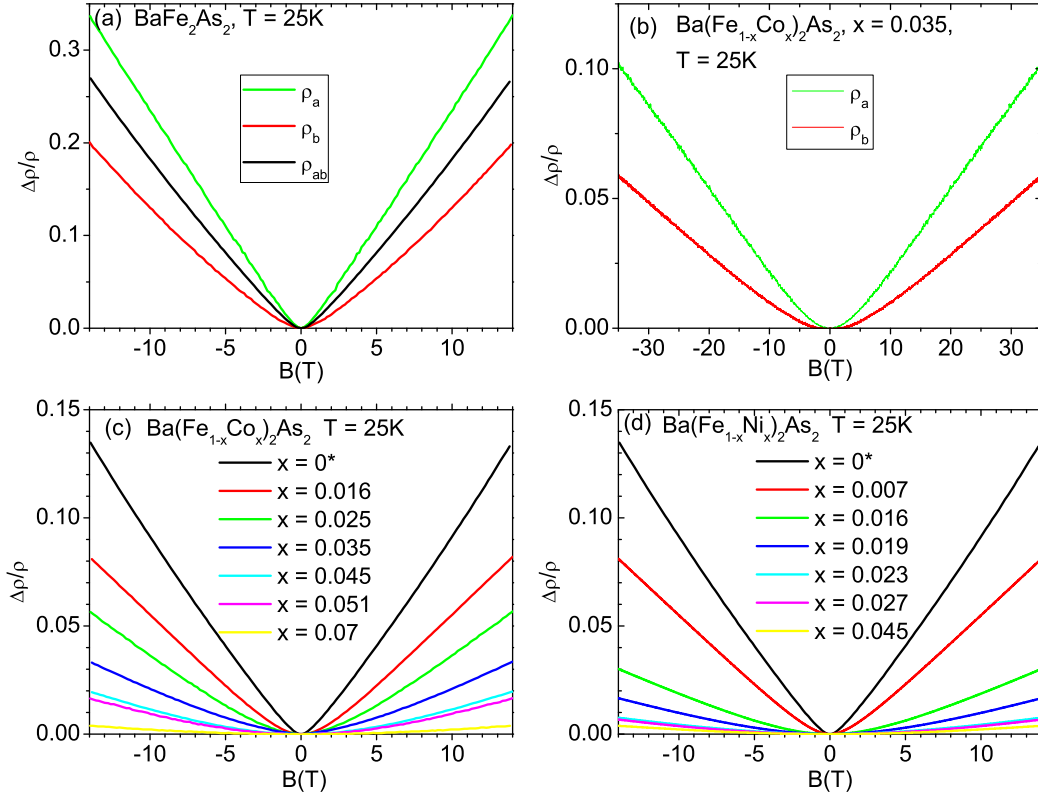


Figure 5.2: Transverse magnetoresistance (MR) ($\Delta\rho/\rho$) of $\text{Ba}(\text{Fe}_{1-x}\text{Co}_x)_2\text{As}_2$ for (a) $x = 0$ (b) 3.5% at $T = 25\text{ K}$. The MR has been measured on detwinned samples with current along a/b axis (Green/Red curves), and also on twinned sample (Black curve). (c,d) The MR of twinned samples of $\text{Ba}(\text{Fe}_{1-x}\text{Co}_x)_2\text{As}_2$ and $\text{Ba}(\text{Fe}_{1-x}\text{Ni}_x)_2\text{As}_2$ respectively at 25 K. *Data for $x = 0$ has been scaled down by a factor of two for clarity. ($\text{Ba}(\text{Fe}_{1-x}\text{Ni}_x)_2\text{As}_2$ data courtesy of Hsueh-Hui Kuo)

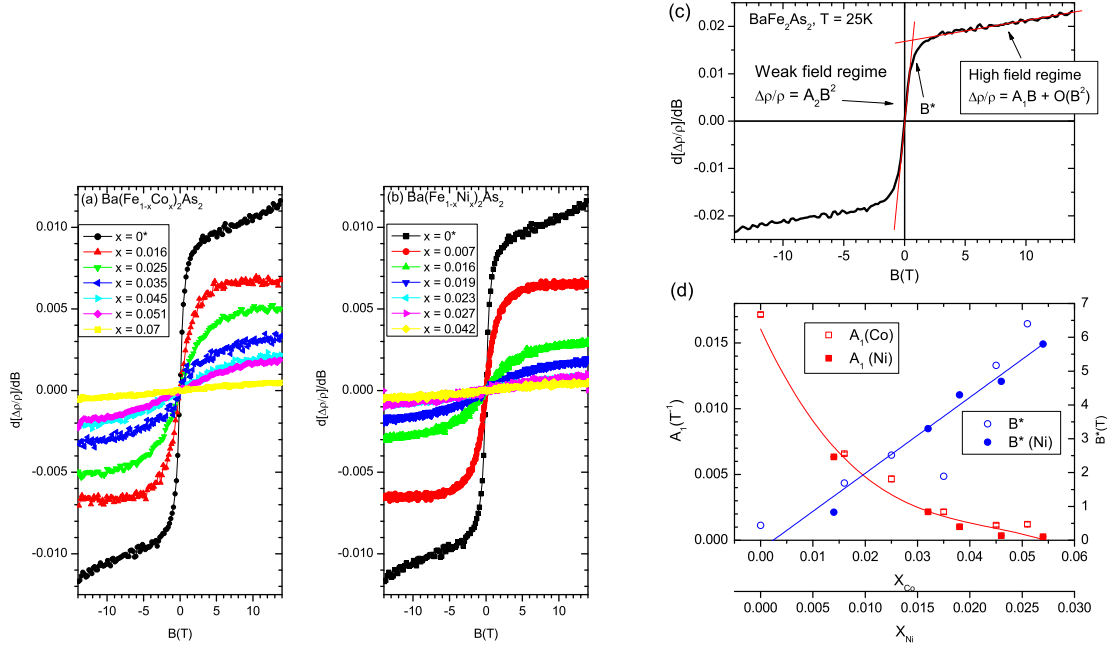


Figure 5.3: (a) The field derivative of MR of twinned samples of $\text{Ba}(\text{Fe}_{1-x}\text{Co}_x)_2\text{As}_2$ and (b) $\text{Ba}(\text{Fe}_{1-x}\text{Ni}_x)_2\text{As}_2$ *Data for $x = 0$ has been scaled down by a factor of two for clarity. (c) The field derivative of MR (dMR/dB) measured on a twinned sample of the parent compound at $T = 25\text{K}$. A critical field scale B^* clearly divides the MR behavior into two regimes: below B^* the MR shows a weak field quadratic behavior and above B^* MR shows a high field linear behavior. (d) The doping evolution of the field scale B^* (blue circles) and the high field MR linear coefficient A_1 (red squares), for $\text{Ba}(\text{Fe}_{1-x}\text{Co}_x)_2\text{As}_2$ and $\text{Ba}(\text{Fe}_{1-x}\text{Ni}_x)_2\text{As}_2$ (solid and open symbols respectively). ($\text{Ba}(\text{Fe}_{1-x}\text{Ni}_x)_2\text{As}_2$ data courtesy of Hsueh-Hui Kuo)

the linear behavior does not depend strongly on the current direction, and the difference of the linear slope can be mainly accounted for by the difference of the zero field resistivity, i.e. $\Delta\rho/\rho$ scales approximately with B/ρ . As was first shown by Abrikosov, a linear band dispersion can lead to a linear MR in the quantum limit[78, 79, 80]. In the case of BaFe_2As_2 , the linear MR could be naturally explained by the presence of Dirac pockets in the AFM reconstructed state due to the symmetry protected band crossing[81].

The cross-over from the weak-field B^2 dependence to the high-field linear dependence can be best seen by considering the field derivative of the MR , ($d[\Delta\rho/\rho]/dB$),

which is plotted in Fig.5.3 for the parent compound. At low fields, $\Delta\rho/\rho = A_2B^2$, resulting in a linear field dependence for $d[\Delta\rho/\rho]/dB$ as B approaches zero. However, above a characteristic field B^* , $d[\Delta\rho/\rho]/dB$ starts to deviate from this weak field behavior, and appears to saturate to a much reduced slope. This indicates that at high field the MR is dominated by a linear field dependence, but there is also a small quadratic term ($\Delta\rho/\rho = A_1B + O(B^2)$).

Substitution of Co or Ni rapidly suppresses the linear *MR* observed for the parent compound. Representative data are shown in Fig.5.2(b) for a detwinned single crystal of $\text{Ba}(\text{Fe}_{1-x}\text{Co}_x)_2\text{As}_2$ with $x = 0.035$ at 25 K. As can be seen, a linear MR is still observed, but the weak-field quadratic behavior extends to a higher field values. As for the parent compound, the anisotropy in the linear slope can be mainly accounted for by the anisotropy in ρ_a and ρ_b .

A comprehensive doping-dependence was obtained for twinned samples of Co and Ni doped BaFe_2As_2 . Representative data are shown in Figs. 5.2 (d) and (e) respectively, illustrating the rapid suppression of the MR with substitution. As described for the parent compound, we can extract the characteristic field B^* by considering the field derivative of the $\Delta\rho/\rho$ (Fig. 5.3). Fitting the high field ($B > B^*$) MR by a second order polynomial, we obtain the coefficient of the linear field dependence coefficient A_1 , the doping dependence of which is shown in Fig. 5.3. As can be seen, the characteristic field scale B^* increases rapidly as a function of doping, whereas the linear coefficient decreases and almost vanishes at $x = 0.051$ for $\text{Ba}(\text{Fe}_{1-x}\text{Co}_x)_2\text{As}_2$ and $x = 0.027$ for $\text{Ba}(\text{Fe}_{1-x}\text{Co}_x)_2\text{As}_2$. Apparently, the rate at which the linear MR is suppressed is twice as rapid for Ni substitution as for Co substitution. This behavior is clearly correlated with the enhancement of resistivity anisotropy, which occurs over a similar range of compositions as shown in Fig. 5.1, indicating that the relatively small resistivity anisotropy in the parent compound is due to the presence of high-mobility Dirac pocket(s).

5.3 Analysis of Magnetoresistance

Both Co and Ni substitutions investigated in this study exhibit a non-monotonic variation of the in-plane resistivity anisotropy as the dopant concentration is progressively increased (Fig. 5.1). Without further information it is not clear whether this effect is related to changes in the anisotropy of the scattering rate, or to changes in the electronic structure. However, as described above, consideration of the magnetotransport properties is suggestive of an important role for the Dirac pocket of the reconstructed Fermi surface. The progressive suppression of the linear MR with chemical substitution, point to a scenario in which the contribution to the conductivity from the FS pockets associated with the protected band crossing (the Dirac pockets) rapidly diminishes with increasing dopant concentrations. For a multi-band system, the conductivity tensor is the sum of the contribution from each Fermi surface. If one particular Fermi surface pocket dominates the conductivity tensor, then the transport anisotropy will also be determined by the anisotropy of that particular Fermi surface. As observed previously by photoemission measurements, the Dirac pockets have an almost isotropic in-plane Fermi velocity [82]. If the mobility of this pocket is such that it dominates the transport, it would severely diminish the anisotropy associated with any other Fermi surfaces, just as we observe for the parent compound. The contribution from these Dirac pockets is progressively weakened by the transition metal substitution, which is manifested in the magnetoresistance. The subsequent emergence of a large in-plane resistivity anisotropy clearly indicates that the remaining low-mobility FS pockets are highly anisotropic.

The mechanism that suppresses the contribution from the Dirac pockets is unclear. The band crossing is protected by crystal inversion symmetry, but introducing impurities into FeAs planes locally breaks this symmetry. This effect would not only open a gap at the Dirac point, but would also increase the scattering rate for the Dirac electrons due to mixing of the orbital wavefunctions. On the other hand, Co substitution is argued to effectively electron-dope the system,[83] which shifts the chemical potential. If there is a gap at the Dirac point, this chemical potential shift could possibly lead to a Lifshitz transition in which the Dirac pocket vanishes. This

possibility has been extensively discussed in the recent papers by Liu et al.[84, 85] A recent Nernst effect measurement also shows a suppression of Dirac transport by Co substitution in the $\text{Eu}(\text{Fe}_{1-x}\text{Co}_x)_2\text{As}_2$ system[86], suggesting the effect is not restricted to BaFe_2As_2 system.

To make a more quantitative understanding of how the Dirac pockets are being suppressed as a function of doping, one would ideally like to obtain the transport parameters for each band. According to Density Functional Theory calculations based Local Density Approximation (LDA), the BaFe_2As_2 parent compound has four closed Fermi surface pockets in the AF reconstructed states, therefore one would need eight independent parameters (mobility and carrier density for each pocket) to characterize the transport properties. If we focus only on the data for fields close to zero, we can obtain the coefficient of the B^2 quadratic term, A_2 , by inverting the sum of the conductivity tensors of the four Fermi surfaces. We denote the conductivity and mobility of each Fermi surface by $\sigma_{i,j}$ and $\mu_{i,j}$, where the index $i = e, h$ stands for electrons or holes, and the index $j = D, P$ represents the Dirac bands and the parabolic bands. We assume no intrinsic magnetoresistance for each individual Fermi surface, because in the condition of isotropic scattering rate and an ellipsoidal FS the leading quadratic term in Zener-Jones expansion is zero. The parameter A_2 is given by

$$A_2 = \frac{\sigma_e \sigma_h (\mu_e + \mu_h)^2}{(\sigma_e + \sigma_h)^2} + \frac{\sigma_e}{\sigma_e + \sigma_h} A_{2,e} + \frac{\sigma_h}{\sigma_e + \sigma_h} A_{2,h} \quad (5.1)$$

$$A_{2,i} = \frac{\sigma_{i,P} \sigma_{i,D} (\mu_{i,D} - \mu_{i,P})^2}{(\sigma_{i,P} + \sigma_{i,D})^2} \quad (5.2)$$

$$\mu_i = \frac{\sigma_{i,D}}{\sigma_{i,P} + \sigma_{i,D}} \mu_{i,D} + \frac{\sigma_{i,P}}{\sigma_{i,P} + \sigma_{i,D}} \mu_{i,P} \quad (5.3)$$

$$\sigma_i = \sigma_{i,D} + \sigma_{i,P}. \quad (5.4)$$

Here, $\sigma_e, \sigma_h, \mu_e, \mu_h$ are the effective electron and hole conductivity and mobility in zero field. If we assume the the Dirac bands are dominating the transport, i.e. $\sigma_{e,D}, \sigma_{h,D} \gg \sigma_{e,P}, \sigma_{h,P}$ and $\mu_{e,D}, \mu_{h,D} \gg \mu_{e,P}, \mu_{h,P}$, the above expression can be greatly simplified because $\sigma_i \sim \sigma_{i,D}$ and $\mu_i \sim \mu_{i,D}$. The second and third term in equation 1 can be

assumed to be much smaller than the first term:

$$\frac{\sigma_e}{\sigma_e + \sigma_h} A_{2,e} = \frac{\sigma_e \sigma_{e,P} \sigma_{e,D} (\mu_{e,P} - \mu_{e,D})^2}{(\sigma_e + \sigma_h) (\sigma_{e,D} + \sigma_{e,P})^2} \quad (5.5)$$

$$= \frac{\sigma_{e,P} \sigma_{e,D} (\mu_{e,P} - \mu_{e,D})^2}{(\sigma_e + \sigma_h) \sigma_e} \sim \frac{\sigma_{e,P} \mu_e^2}{(\sigma_e + \sigma_h)} \quad (5.6)$$

$$= \frac{\sigma_{e,P} (\sigma_e + \sigma_h) \mu_e^2}{(\sigma_e + \sigma_h)^2} \ll \frac{\sigma_e \sigma_h (\mu_e + \mu_h)^2}{(\sigma_e + \sigma_h)^2}, \quad (5.7)$$

and equation 1 reduces to only the first term, which only depends on the effective mobility and conductivity of electrons and holes. The simplicity of this expression allow us to make a physical interpretation of the coefficient A_2 in terms of an effective mobility,

$$\sqrt{A_2} = \frac{\sqrt{\sigma_e \sigma_h}}{\sigma_e + \sigma_h} (\mu_e + \mu_h) = \mu_{MR} \leq \frac{1}{2} (\mu_e + \mu_h) \equiv \mu_{ave}. \quad (5.8)$$

The square root of the quadratic field coefficient A_2 , which we denote as μ_{MR} , gives the lower bound of the average mobility of electrons and holes (μ_{ave}). The equality between μ_{ave} and μ_{MR} holds only when the electron and hole conductivities are equal. However, even in the case of a strongly asymmetric conduction scenario, the μ_{MR} still gives a good estimate of μ_{ave} . For example if $\sigma_e/\sigma_h = 10$ then $\mu_{MR} = 0.6\mu_{ave}$. All of the above reasoning makes sense only when the assumption that the Dirac bands dominate the transport holds. To be consistent, we extract the real number of the parent compounds to see if this is really the case. The value of μ_{MR} of the parent compounds at 25 K is about 1130 cm²/Vs, which is comparable to the mobility of the Dirac pockets extracted from quantum oscillations for crystals prepared under similar conditions (~ 1000 cm²/Vs)[87]. This is indeed consistent with the assumption of $\mu_e \sim \mu_{e,D}$. We can also obtain the effective carrier density n_{MR} by using the relation $\sigma = ne\mu$. If $\sigma_e \sim \sigma_{e,D}$, then n_{MR} should be similar to the carrier density of Dirac carriers rather than the total carrier density. In the parent compound the observed value of $\mu_{MR} = 1130$ cm²/Vs corresponds to a very low effective carrier concentration, $n_{MR} = 0.003$ electron per Fe. This value is much lower than the total number of carriers that one would obtain from the LDA calculations and ARPES

measurements, but is comparable to the size of Dirac pockets as observed from the quantum oscillation experiments[87]. Therefore the assumption $\sigma_e \sim \sigma_{e,D}$ also holds.

The effective mobility extracted from MR is much higher than the mobility directly obtained from the Hall coefficient $\mu_{Hall} = |R\sigma| = 376\text{cm}^2/Vs$. This is because the contribution of electron and hole mobility in the Hall coefficient cancel each other:

$$R = \frac{\sigma_e^2 R_e + \sigma_h^2 R_h}{(\sigma_e + \sigma_h)^2} = \frac{-\sigma_e \mu_e + \sigma_h \mu_h}{(\sigma_e + \sigma_h)^2} \quad (5.9)$$

$$\mu_{Hall} = \left| \frac{-\sigma_e \mu_e + \sigma_h \mu_h}{\sigma_e + \sigma_h} \right| \quad (5.10)$$

In fact, the much smaller value of Hall mobility than the MR mobility already implies that the contribution to the conductivity of electrons and holes are of the same scale. To understand this one can consider the opposite case, one where electrons dominate the conduction $\mu_e \gg \mu_h$ and $\sigma_e \gg \sigma_h$:

$$\mu_{Hall} = \left| \frac{-\sigma_e \mu_e + \sigma_h \mu_h}{\sigma_e + \sigma_h} \right| \sim \left| \frac{-\sigma_e \mu_e}{\sigma_e + \sigma_h} \right| \sim \mu_e \quad (5.11)$$

$$\mu_{MR} = \frac{\sqrt{\sigma_e \sigma_h}}{\sigma_e + \sigma_h} (\mu_e + \mu_h) \sim \frac{\sqrt{\sigma_e \sigma_h}}{\sigma_e} \mu_e = \sqrt{\frac{\sigma_h}{\sigma_e}} \mu_e \quad (5.12)$$

$$\sqrt{\frac{\sigma_h}{\sigma_e}} \ll 1 \Rightarrow \mu_{MR} \ll \mu_{Hall} \quad (5.13)$$

Therefore our measured value suggests that both electrons and holes play an important role in the transport in the reconstructed state in the parent compound, and this also gives us the confidence that μ_{MR} is a good estimate of μ_{ave} , since their difference is smaller when σ_e gets closer to σ_h .

As we argued above: the high μ_{MR} and small n_{MR} reflects the fact that transport in the parent compound is dominated by a small number of high mobility carriers, i.e. the carriers from the Dirac pockets. However, this is no longer the case as we increase the Ni or Co doping concentration. The extracted value of μ_{MR} and n_{MR} as a function of doping is plotted in Fig. 5.4. By increasing doping concentration μ_{MR}

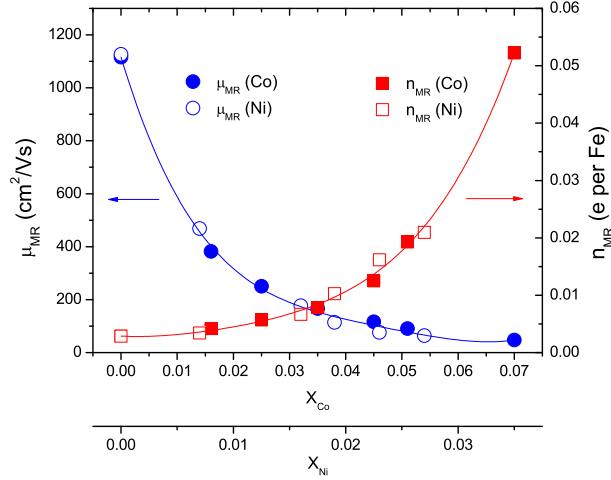


Figure 5.4: The doping evolution of the effective MR mobility μ_{MR} and effective MR carrier density n_{MR} of $Ba(Fe_{1-x}Co_x)_2As_2$ and $Ba(Fe_{1-x}Ni_x)_2As_2$ extracted from weak field MR , as described in the text.

decreases rapidly and n_{MR} increases rapidly. Apparently our previous assumption that helped us simplify the MR expression is no longer valid, and it is difficult to make a simple physical interpretation of the extracted μ_{MR} or n_{MR} . Nevertheless, the observed doping evolution is highly suggestive of a shift of the dominant role in transport to the high carrier density and low mobility carriers. Again the effect of Ni doping on suppressing the Dirac carriers is twice as fast as Co. Our data reveal that as the conductivity from the Dirac pockets is progressively suppressed, a large in-plane resistivity anisotropy emerges. The direct implication is that the other pockets of reconstructed FS are highly anisotropic, which is borne out by recent quantum oscillation measurements of $BaFe_2As_2$. [88]

Evidence for the suppression of the contribution of a high mobility pocket of reconstructed FS can also be found in the doping-dependence of the resistivity at low temperature. A direct comparison of the magnitude of the in-plane resistivity

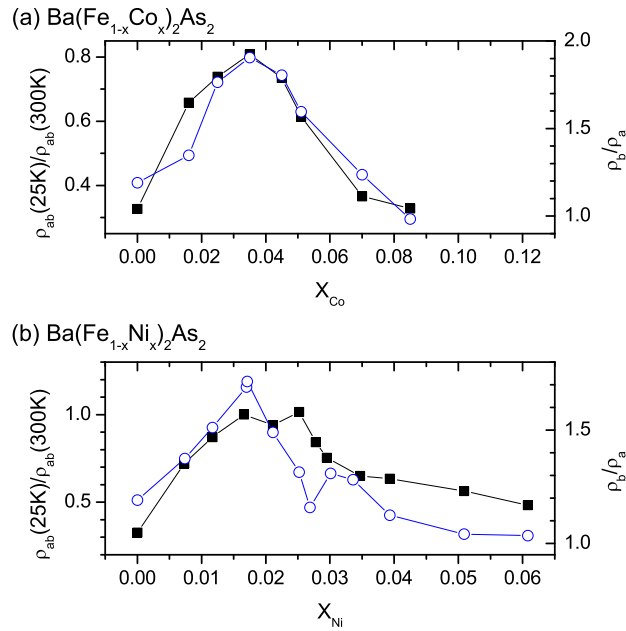


Figure 5.5: The doping evolution of the in-plane resistivity of the twinned crystals at $T = 25\text{K}$ normalized by its room temperature value and the in-plane resistivity anisotropy ratio ρ_b/ρ_a of detwinned crystal at $T = 25\text{K}$. Data are plotted for (a) $\text{Ba}(\text{Fe}_{1-x}\text{Co}_x)_2\text{As}_2$, (b) $\text{Ba}(\text{Fe}_{1-x}\text{Ni}_x)_2\text{As}_2$ ($\text{Ba}(\text{Fe}_{1-x}\text{Ni}_x)_2\text{As}_2$ data courtesy of Hsueh-Hui Kuo)

normalized by its room temperature value^{1 2} and the in-plane resistivity anisotropy at $T = 25$ K is plotted in Fig. 5.5. As can be seen, the two quantities follow each other closely in the case of Co and Ni doping. Based on the previous analysis, the doping evolution of the resistivity can be readily understood. Initial suppression of the contribution to the transport arising from the Dirac pocket leads to an initial rise of the normalized resistivity. With progressive doping the magnetic order is further suppressed, releasing carriers and hence leading to a decrease in the resistivity for higher dopant concentrations. Note that the progressive doping also suppresses the structural transition that breaks the rotational symmetry, therefore after reaching a maximum value, the in-plane anisotropy also decreases.

5.4 Discussion

An intriguing correspondence can be made between the iron pnictides and underdoped cuprates.[89] Recent Nernst measurements reveal a large in-plane electronic anisotropy onsets at the pseudogap temperature[39]. Further Hall coefficient and quantum oscillation measurements suggested at even lower temperatures broken translational symmetry causes a reconstruction the Fermi surface and a high mobility isotropic electron pocket emerges[90]. This high mobility electron pocket dominates the low temperature transport. As a result, not only does the Hall effect change sign from positive to negative, but the large electronic anisotropy which onsets at pseudogap temperature is also reduced. It has also been suggested that at a critical doping the system could undergo a Lifshitz transition at which the high mobility electron pocket disappears, which is also accompanied by an enhancement of in-plane resistivity anisotropy[90].

¹To avoid uncertainty in geometric factor, the magnitude of the resistivity is normalized by its room temperature value, which is typically $250 \sim 300 \mu\Omega cm$ in this doping range[73]. The room temperature value decreases slightly as a function of doping in the doping range we study here (less than 20%), therefore the large variation of the normalized value at low temperature reflects the evolution of the electronic structure and charge dynamics.

²We used the resistivity of the twinned crystals, which is essentially the average of ρ_a and ρ_b . The average value is actually more revealing to study the effect of isotropic Dirac pocket

Chapter 6

Summary and Outlook

It is generally believed that insights into the physics of the normal state will lead to a better understanding of the origin of high temperature superconductivity. Mounting evidences suggest that the rotational symmetry breaking plays an important role in the normal state of both iron and copper based superconductors. The major effort of this thesis is to characterize and understand the nature of the broken rotational symmetry in iron arsenide superconductors.

The phase diagram for the electron-doped iron pnictides $\text{Ba}(\text{Fe}_{1-x}\text{Co}_x)_2\text{As}_2$ was determined through several thermodynamic and transport measurements. We find that the single structural/magnetic phase transition that occurs in BaFe_2As_2 splits with Co-doping, with structural transition occurred at higher temperatures. Critical temperatures associated with both transitions are progressively reduced with increasing Co concentration, and are suppressed below T_c coincident with optimal doping. The superconducting "dome" extends over a limited range of Co concentrations, from $x = 0.025$ to $x = 0.18$. These observations clearly delineate regions of the $x - T$ phase diagram for which the system breaks the crystal rotational symmetry without breaking translational symmetry.

To asses the intrinsic in-plane electronic anisotropy in the broken symmetry phase, we perform measurements of the in-plane resistivity of detwinned single crystals of $\text{Ba}(\text{Fe}_{1-x}\text{Co}_x)_2\text{As}_2$. We reveal that this representative class of iron arsenide develops a large electronic anisotropy at the structural transition, with the resistivity along

the shorter b -axis ρ_b being greater than ρ_a . The anisotropy reaches a maximum value of ~ 2 for compositions in the neighborhood of the beginning of the superconducting dome, showing an intriguing non-monotonic doping dependence. For temperatures well above the structural transition, uniaxial stress induces a resistivity anisotropy, indicating a substantial nematic susceptibility.

In order to determine the true driving force behind the structural phase transition, we develop experiment technique to apply in-situ tunable strain on single crystal samples, which allow us to explicitly measure the nematic susceptibility at a constant strain. The divergent nematic susceptibility above structural phase transition unambiguously distinguishes an electronic nematic phase transition from a simple ferroelastic distortion. These measurements also reveal an electronic nematic quantum phase transition at the composition with optimal superconducting transition temperature.

In comparison to other electron nematic systems such as $\text{Sr}_3\text{Ru}_2\text{O}_7$ [34] and the quantum Hall system[33], the phase transition of iron-pnictides occurs at zero field and at a temperature range between 50 and 150K, providing an accessible platform for spectroscopy and thermodynamic measurements. While the pseudo-gap phase in underdoped cuprates exists for similar conditions to these, the iron-arsenides have a well-defined phase boundary associated with the nematic phase transition. In this sense, the iron-arsenides present a cleaner system in which to investigate the physical origin of nematic order and the consequences for superconductivity.

The non-monotonic variation in the resistivity anisotropy at low temperature as the dopant concentration is increased is especially striking given the uniform suppression of the lattice orthorhombicity. The linear MR which are observed for the parent compound, and which are likely associated with the Dirac pockets of the reconstructed FS, are suppressed with increasing dopant concentrations. Intriguingly, for both Co and Ni substitution, the large in-plane resistivity anisotropy is found to emerge over the same range of compositions at which the linear MR are progressively suppressed. Consideration of this evidence suggests that the isotropic, high-mobility Dirac pockets revealed by dHvA, ARPES and magnetotransport measurements, might effectively mask the intrinsic in-plane transport anisotropy associated with the other pockets of

reconstructed FS. Within such a scenario, only when the contribution to the conductivity from the Dirac pockets is suppressed can the underlying anisotropy be revealed in the transport, perhaps accounting for the non-monotonic doping dependence.

Although subsequent measurements of optical conductivity[45] and photoemission[46] of detwinned samples of $\text{Ba}(\text{Fe}_{1-x}\text{Co}_x)_2\text{As}_2$ revealed that the electronic anisotropy extends to high energy. It remains to be seen to what extent the presence of a large anisotropy is a generic feature of the phase diagram of Fe-pnictide superconductors. Recent measurements of K-substituted BaFe_2As_2 indicate that the hole doped analog exhibit a vanishingly small, and even reverse in-plane anisotropy [69, 70]. This might reflect differences in the effect of electron vs hole doping on the reconstructed FS, or perhaps differences in the elastic scattering rate, since chemical substitution away from the Fe plane will presumably have a weaker effect.

Finally the experiment we introduced in chapter 4 is a methodology to detect the electronic tendency towards rotational symmetry breaking as if there is no coupling to the lattice, and is by no means restricted to the iron pnictides. One can also incorporate this methodology with other experimental probes, which allows us to more generally disentangle the cause and effect in systems for which different degrees of freedom strongly couple. For example, it is still an ongoing debate about the microscopic mechanism of the electron nematic phase transition in pnictides, which could potentially arise from the spin or orbital degree of freedom. By applying a constant strain and measuring temperature dependence of the orbital response by ARPES[46] or optical conductivity[45] and measuring the spin response by neutron scattering , the debate might be resolved.

Bibliography

- [1] S Graser, T A Maier, P J Hirschfeld, and D J Scalapino. Near-degeneracy of several pairing channels in multiorbital models for the Fe pnictides. *New Journal of Physics*, 11(2):025016, 2009.
- [2] C. Lester, Jiun-Haw Chu, J. G. Analytis, S. C. Capelli, A. S. Erickson, C. L. Condon, M. F. Toney, I. R. Fisher, and S. M. Hayden. Neutron scattering study of the interplay between structure and magnetism in $\text{Ba}(\text{Fe}_{1-x}\text{Co}_x)_2\text{As}_2$. *Phys. Rev. B*, 79:144523, Apr 2009.
- [3] J.G. Bednorz and K.A. Mueller. Possible high TC superconductivity in the Ba-La-Cu-O system. *Z. Phys. B*, 64.
- [4] Yoichi Kamihara, Takumi Watanabe, Masahiro Hirano, and Hideo Hosono. Iron-Based Layered Superconductor $\text{La}[\text{O}_{1-x}\text{F}_x]\text{FeAs}$ ($x = 0.050.12$) with $T_c = 26$ K. *Journal of the American Chemical Society*, 130(11):3296–3297, 2008.
- [5] Ren Zhi-An, Lu Wei, Yang Jie, Yi Wei, Shen Xiao-Li, Zheng-Cai, Che Guang-Can, Dong Xiao-Li, Sun Li-Ling, Zhou Fang, and Zhao Zhong-Xian. Superconductivity at 55 K in Iron-Based F-Doped Layered Quaternary Compound $\text{Sm}[\text{O}_{1-x}\text{F}_x]\text{FeAs}$. *Chinese Physics Letters*, 25(6):2215, 2008.
- [6] J. Orenstein and A. J. Millis. Advances in the Physics of High-Temperature Superconductivity. *Science*, 288:468–475, April 2000.
- [7] G. R. Stewart. Superconductivity in iron compounds. *Rev. Mod. Phys.*, 83:1589–1652, Dec 2011.

- [8] J. Wen, G. Xu, G. Gu, J. M. Tranquada, and R. J. Birgeneau. Interplay between magnetism and superconductivity in iron-chalcogenide superconductors: crystal growth and characterizations. *Reports on Progress in Physics*, 74(12):124503, December 2011.
- [9] D. J. Singh and M.-H. Du. Density Functional Study of $\text{LaFeAsO}_{1-x}\text{F}_x$: A Low Carrier Density Superconductor Near Itinerant Magnetism. *Phys. Rev. Lett.*, 100:237003, Jun 2008.
- [10] D. H. Lu, M. Yi, S.-K. Mo, A. S. Erickson, J. Analytis, J.-H. Chu, D. J. Singh, Z. Hussain, T. H. Geballe, I. R. Fisher, and Z.-X. Shen. Electronic structure of the iron-based superconductor LaOFeP . *Nature*, 455:81–84, September 2008.
- [11] M. Yi, D. H. Lu, J. G. Analytis, J.-H. Chu, S.-K. Mo, R.-H. He, R. G. Moore, X. J. Zhou, G. F. Chen, J. L. Luo, N. L. Wang, Z. Hussain, D. J. Singh, I. R. Fisher, and Z.-X. Shen. Electronic structure of the BaFe_2As_2 family of iron-pnictide superconductors. *Phys. Rev. B*, 80:024515, Jul 2009.
- [12] M. D. Lumsden and A. D. Christianson. TOPICAL REVIEW: Magnetism in Fe-based superconductors. *Journal of Physics Condensed Matter*, 22(20):203203, May 2010.
- [13] A. V. Chubukov, D. V. Efremov, and I. Eremin. Magnetism, superconductivity, and pairing symmetry in iron-based superconductors. *Phys. Rev. B*, 78:134512, Oct 2008.
- [14] H. Gretarsson, A. Lupascu, Jungho Kim, D. Casa, T. Gog, W. Wu, S. R. Julian, Z. J. Xu, J. S. Wen, G. D. Gu, R. H. Yuan, Z. G. Chen, N.-L. Wang, S. Khim, K. H. Kim, M. Ishikado, I. Jarrige, S. Shamoto, J.-H. Chu, I. R. Fisher, and Young-June Kim. Revealing the dual nature of magnetism in iron pnictides and iron chalcogenides using x-ray emission spectroscopy. *Phys. Rev. B*, 84:100509, Sep 2011.
- [15] M. Yi, D. H. Lu, J. G. Analytis, J.-H. Chu, S.-K. Mo, R.-H. He, M. Hashimoto, R. G. Moore, I. I. Mazin, D. J. Singh, Z. Hussain, I. R. Fisher, and Z.-X. Shen.

- Unconventional electronic reconstruction in undoped (Ba,Sr)Fe₂As₂ across the spin density wave transition. *Phys. Rev. B*, 80:174510, Nov 2009.
- [16] P. L. Alireza, Y. T. C. Ko, J. Gillett, C. M. Petrone, J. M. Cole, G. G. Lonzarich, and S. E. Sebastian. FAST TRACK COMMUNICATION: Superconductivity up to 29 K in SrFe₂As₂ and BaFe₂As₂ at high pressures. *Journal of Physics Condensed Matter*, 21(1):012208, January 2009.
- [17] Marianne Rotter, Marcus Tegel, Dirk Johrendt, Inga Schellenberg, Wilfried Hermes, and Rainer Pottgen. *Phys. Rev. B*, 78:020503, 2008.
- [18] Athena S. Sefat, Rongying Jin, Michael A. McGuire, Brian C. Sales, David J. Singh, and David Mandrus. *Phys. Rev. Lett.*, 101:117004, 2008.
- [19] I. I. Mazin, D. J. Singh, M. D. Johannes, and M. H. Du. Unconventional Superconductivity with a Sign Reversal in the Order Parameter of LaFeAsO_{1-x}F_x. *Phys. Rev. Lett.*, 101:057003, Jul 2008.
- [20] A. D. Christianson, E. A. Goremychkin, R. Osborn, S. Rosenkranz, M. D. Lumsden, C. D. Malliakas, I. S. Todorov, H. Claus, D. Y. Chung, M. G. Kanatzidis, R. I. Bewley, and T. Guidi. Resonant spin excitation in the high temperature superconductor Ba_{0.6}K_{0.4}Fe₂As₂. *NATURE*, 456:930, 2008.
- [21] D. S. Inosov, J. T. Park, P. Bourges, D. L. Sun, Y. Sidis, A. Schneidewind, K. Hradil, D. Haug, C. T. Lin, B. Keimer, and V. Hinkov. Normal-state spin dynamics and temperature-dependent spin-resonance energy in optimally doped BaFe_{1.85}Co_{0.15}As₂. *Nature Physics*, 6:178–181, March 2010.
- [22] J. D. Fletcher, A. Serafin, L. Malone, J. G. Analytis, J.-H. Chu, A. S. Erickson, I. R. Fisher, and A. Carrington. Evidence for a Nodal-Line Superconducting State in LaFePO. *Phys. Rev. Lett.*, 102:147001, Apr 2009.
- [23] Clifford W. Hicks, Thomas M. Lippman, Martin E. Huber, James G. Analytis, Jiun-Haw Chu, Ann S. Erickson, Ian R. Fisher, and Kathryn A. Moler. Evidence

- for a Nodal Energy Gap in the Iron-Pnictide Superconductor LaFePO from Penetration Depth Measurements by Scanning SQUID Susceptometry. *Phys. Rev. Lett.*, 103:127003, Sep 2009.
- [24] Lan Luan, Thomas M. Lippman, Clifford W. Hicks, Julie A. Bert, Ophir M. Auslaender, Jiun-Haw Chu, James G. Analytis, Ian R. Fisher, and Kathryn A. Moler. Local Measurement of the Superfluid Density in the Pnictide Superconductor $\text{Ba}(\text{Fe}_{1-x}\text{Co}_x)_2\text{As}_2$ across the Superconducting Dome. *Phys. Rev. Lett.*, 106:067001, Feb 2011.
- [25] P J Hirschfeld, M M Korshunov, and I I Mazin. Gap symmetry and structure of fe-based superconductors. *Reports on Progress in Physics*, 74(12):124508, 2011.
- [26] J. W. Lynn Jiying Li W. Ratcliff II J. L. Zarestky H. A. Mook G. F. Chen J. L. Luo N. L. Wang Clarina de la Cruz, Q. Huang and Pengcheng Dai. Magnetic order close to superconductivity in the iron-based layered $\text{LaO}_{1-x}\text{F}_x\text{FeAs}$ systems. *Nature*, 453(7197):899, 2008.
- [27] D. K. Pratt, W. Tian, A. Kreyssig, J. L. Zarestky, S. Nandi, N. Ni, S. L. Bud'ko, P. C. Canfield, A. I. Goldman, and R. J. McQueeney. Coexistence of competing antiferromagnetic and superconducting phases in the underdoped $\text{ba}(\text{fe}_{0.953}\text{CO}_{0.047})_2\text{as}_2$ compound using x-ray and neutron scattering techniques. *Phys. Rev. Lett.*, 103:087001, Aug 2009.
- [28] Chen Fang, Hong Yao, Wei-Feng Tsai, JiangPing Hu, and Steven A. Kivelson. Theory of electron nematic order in LaFeAsO. *Phys. Rev. B*, 77:224509, Jun 2008.
- [29] Cenke Xu, Markus Müller, and Subir Sachdev. Ising and spin orders in the iron-based superconductors. *Phys. Rev. B*, 78:020501, Jul 2008.
- [30] T. Yildirim. Strong Coupling of the Fe-Spin State and the As-As Hybridization in Iron-Pnictide Superconductors from First-Principle Calculations. *Phys. Rev. Lett.*, 102:037003, Jan 2009.

- [31] C.-C. Chen, B. Moritz, J. van den Brink, T. P. Devereaux, and R. R. P. Singh. Finite-temperature spin dynamics and phase transitions in spin-orbital models. *Phys. Rev. B*, 80:180418, Nov 2009.
- [32] Weicheng Lv, Jiansheng Wu, and Philip Phillips. Orbital ordering induces structural phase transition and the resistivity anomaly in iron pnictides. *Phys. Rev. B*, 80:224506, Dec 2009.
- [33] M. P. Lilly, K. B. Cooper, J. P. Eisenstein, L. N. Pfeiffer, and K. W. West. Evidence for an anisotropic state of two-dimensional electrons in high Landau levels. *Phys. Rev. Lett.*, 82:394–397, Jan 1999.
- [34] R. A. Borzi, S. A. Grigera, J. Farrell, R. S. Perry, S. J. S. Lister, S. L. Lee, D. A. Tennant, Y. Maeno, and A. P. Mackenzie. Formation of a Nematic Fluid at High Fields in $\text{Sr}_3\text{Ru}_2\text{O}_7$. *Science*, 315(5809):214–217, 2007.
- [35] R. Okazaki, T. Shibauchi, H. J. Shi, Y. Haga, T. D. Matsuda, E. Yamamoto, Y. Onuki, H. Ikeda, and Y. Matsuda. Rotational Symmetry Breaking in the Hidden-Order Phase of URu_2Si_2 . *Science*, 331:439–, January 2011.
- [36] C. Stingl, R. S. Perry, Y. Maeno, and P. Gegenwart. Symmetry-Breaking Lattice Distortion in $\text{Sr}_3\text{Ru}_2\text{O}_7$. *Phys. Rev. Lett.*, 107:026404, Jul 2011.
- [37] Yoichi Ando, Kouji Segawa, Seiki Komiya, and A. N. Lavrov. Electrical resistivity anisotropy from self-organized one dimensionality in high-temperature superconductors. *Phys. Rev. Lett.*, 88:137005, Mar 2002.
- [38] V. Hinkov, D. Haug, B. Fauqu, P. Bourges, Y. Sidis, A. Ivanov, C. Bernhard, C. T. Lin, and B. Keimer. Electronic Liquid Crystal State in the High-Temperature Superconductor $\text{YBa}_2\text{Cu}_3\text{O}_{6.45}$. *Science*, 319(5863):597–600, 2008.
- [39] R. Daou, J. Chang, David LeBoeuf, Olivier Cyr-Choiniere, Francis Laliberte, Nicolas Doiron-Leyraud, B. J. Ramshaw, Ruixing Liang, D. A. Bonn, W. N. Hardy, and Louis Taillefer. Broken rotational symmetry in the pseudogap phase of a high- $T(c)$ superconductor. *NATURE*, 463(7280):519–522, JAN 28 2010.

- [40] Jiun-Haw Chu, James G. Analytis, Chris Kucharczyk, and Ian R. Fisher. Determination of the phase diagram of the electron-doped superconductor $\text{Ba}(\text{Fe}_{1-x}\text{Co}_x)_2\text{As}_2$. *Phys. Rev. B*, 79:014506, Jan 2009.
- [41] Jiun-Haw Chu, James G. Analytis, David Press, Kristiaan De Greve, Thaddeus D. Ladd, Yoshihisa Yamamoto, and Ian R. Fisher. In-plane electronic anisotropy in underdoped $\text{Ba}(\text{Fe}_{1-x}\text{Co}_x)_2\text{As}_2$ revealed by partial detwinning in a magnetic field. *Phys. Rev. B*, 81:214502, Jun 2010.
- [42] J.-H. Chu, J. G. Analytis, K. De Greve, P. L. McMahon, Z. Islam, Y. Yamamoto, and I. R. Fisher. In-Plane Resistivity Anisotropy in an Underdoped Iron Arsenide Superconductor. *Science*, 329:824–, August 2010.
- [43] Hsueh-Hui Kuo, Jiun-Haw Chu, Scott C. Riggs, Leo Yu, Peter L. McMahon, Kristiaan De Greve, Yoshihisa Yamamoto, James G. Analytis, and Ian R. Fisher. Possible origin of the nonmonotonic doping dependence of the in-plane resistivity anisotropy of $\text{Ba}(\text{Fe}_{1-x}\text{T}_x)_2\text{As}_2$ (T=Co, Ni and Cu). *Phys. Rev. B*, 84:054540, Aug 2011.
- [44] J.-H. Chu, H.-H. Kuo, J. G. Analytis, and I. R. Fisher. Divergent nematic susceptibility in an iron arsenide superconductor. *ArXiv e-prints*, March 2012.
- [45] A. Dusza, A. Lucarelli, F. Pfuner, J.-H. Chu, I. R. Fisher, and L. Degiorgi. Anisotropic charge dynamics in detwinned $\text{Ba}(\text{Fe}_{1-x}\text{Co}_x)_2\text{As}_2$. *EPL (Europhysics Letters)*, 93:37002, February 2011.
- [46] M. Yi, D. Lu, J.-H. Chu, J. G. Analytis, A. P. Sorini, A. F. Kemper, B. Moritz, S.-K. Mo, R. G. Moore, M. Hashimoto, W.-S. Lee, Z. Hussain, T. P. Devereaux, I. R. Fisher, and Z.-X. Shen. Symmetry-breaking orbital anisotropy observed for detwinned $\text{Ba}(\text{Fe}_{1-x}\text{Co}_x)_2\text{As}_2$ above the spin density wave transition. *Proceedings of the National Academy of Science*, 108:6878–6883, April 2011.
- [47] A Dusza, A Lucarelli, A Sanna, S Massidda, J-H Chu, I R Fisher, and L Degiorgi. Anisotropic in-plane optical conductivity in detwinned $\text{Ba}(\text{Fe}_{1-x}\text{Co}_x)_2\text{As}_2$. *New Journal of Physics*, 14(2):023020, 2012.

- [48] Marianne Rotter, Marcus Tegel, and Dirk Johrendt. Superconductivity at 38 K in the Iron Arsenide $(\text{Ba}_{1-x}\text{K}_x)\text{Fe}_2\text{As}_2$. *Phys. Rev. Lett.*, 101:107006, Sep 2008.
- [49] H. Chen, Y. Ren, Y. Qiu, Wei Bao, R. H. Liu, G. Wu, T. Wu, Y. L. Xie, X. F. Wang, Q. Huang, and X. H. Chen. Coexistence of the spin-density wave and superconductivity in $\text{Ba}_{1-x}\text{K}_x\text{Fe}_2\text{As}_2$. *EPL (Europhysics Letters)*, 85(1):17006, 2009.
- [50] X. F. Wang, T. Wu, G. Wu, H. Chen, Y. L. Xie, J. J. Ying, Y. J. Yan, R. H. Liu, and X. H. Chen. Anisotropy in the Electrical Resistivity and Susceptibility of Superconducting BaFe_2As_2 Single Crystals. *Phys. Rev. Lett.*, 102:117005, Mar 2009.
- [51] J K Dong, L Ding, H Wang, X F Wang, T Wu, G Wu, X H Chen, and S Y Li. Thermodynamic properties of $\text{Ba}_{1-x}\text{K}_x\text{Fe}_2\text{As}_2$ and $\text{Ca}_{1-x}\text{Na}_x\text{Fe}_2\text{As}_2$. *New Journal of Physics*, 10(12):123031, 2008.
- [52] Michael E. Fisher. *Philos. Mag.*, 7:1731, 1962.
- [53] Clarina de la Cruz Shiliang Li J. W. Lynn Y. Chen M. A. Green G. F. Chen G. Li Z. Li J. L. Luo N. L. Wang Jun Zhao, Q. Huang and Pengcheng Dai. *Nature Materials*, 7:953, 2008.
- [54] N. D. Mathur, F. M. Grosche, S. R. Julian, I. R. Walker, D. M. Freye, R. K. W. Haselwimmer, and G. G. Lonzarich. *Nature*, 394:39, 1998.
- [55] S. S. Saxena, P. Agarwal, K. Ahilan, F. M. Grosche, R. K. W. Haselwimmer, M. J. Steiner, E. Pugh, I. R. Walker, S. R. Julian, P. Monthoux, G. G. Lonzarich, A. Huxley, I. Sheikin, D. Braithwaite, and J. Flouquet. *Nature*, 406:587, 2000.
- [56] S. Nandi, M. G. Kim, A. Kreyssig, R. M. Fernandes, D. K. Pratt, A. Thaler, N. Ni, S. L. Bud'ko, P. C. Canfield, J. Schmalian, R. J. McQueeney, and A. I. Goldman. Anomalous Suppression of the Orthorhombic Lattice Distortion in Superconducting $\text{Ba}(\text{Fe}_{1-x}\text{Co}_x)_2\text{As}_2$ Single Crystals. *Phys. Rev. Lett.*, 104:057006, Feb 2010.

- [57] F. L. Ning, K. Ahilan, T. Imai, A. S. Sefat, M. A. McGuire, B. C. Sales, D. Mandrus, P. Cheng, B. Shen, and H.-H. Wen. Contrasting Spin Dynamics between Underdoped and Overdoped $\text{Ba}(\text{Fe}_{1-x}\text{Co}_x)_2\text{As}_2$. *Phys. Rev. Lett.*, 104:037001, Jan 2010.
- [58] M. Yoshizawa, D. Kimura, T. Chiba, S. Simayi, Y. Nakanishi, K. Kihou, C.-H. Lee, A. Iyo, H. Eisaki, M. Nakajima, and S.-i. Uchida. Structural Quantum Criticality and Superconductivity in Iron-Based Superconductor $\text{Ba}(\text{Fe}_{1-x}\text{Co}_x)_2\text{As}_2$. *Journal of the Physical Society of Japan*, 81(2):024604, February 2012.
- [59] M. D. Johannes and I. I. Mazin. Microscopic origin of magnetism and magnetic interactions in ferropnictides. *Phys. Rev. B*, 79:220510, Jun 2009.
- [60] Chi-Cheng Lee, Wei-Guo Yin, and Wei Ku. Ferro-orbital order and strong magnetic anisotropy in the parent compounds of iron-pnictide superconductors. *Phys. Rev. Lett.*, 103:267001, Dec 2009.
- [61] M. J. Lawler, J. P. Eisenstein, E. Fradkin, S. A. Kivelson and A. P. Mackenzie. Nematic fermi fluids in condensed matter physics. *Annu. Rev. Condens. Matter Phys.*, 1:153, 2010.
- [62] C. Ma, H. X. Yang, H. F. Tian, H. L. Shi, J. B. Lu, Z. W. Wang, L. J. Zeng, G. F. Chen, N. L. Wang, and J. Q. Li. Microstructure and tetragonal-to-orthorhombic phase transition of AFe_2As_2 $\text{A}=\text{Sr},\text{Ca}$ as seen via transmission electron microscopy. *Phys. Rev. B*, 79:060506, Feb 2009.
- [63] M. A. Tanatar, A. Kreyssig, S. Nandi, N. Ni, S. L. Bud'ko, P. C. Canfield, A. I. Goldman, and R. Prozorov. Direct imaging of the structural domains in the iron pnictides AFe_2As_2 $\text{A}=\text{Ca},\text{Sr},\text{Ba}$. *Phys. Rev. B*, 79:180508, May 2009.
- [64] A. N. Lavrov, S. Komiya, and Y. Ando. Antiferromagnets: Magnetic shape-memory effects in a crystal. *Nature*, 418:385–386, July 2002.
- [65] *Magnetoresistance in Metals*. Cambridge University Press, London, 1989.

- [66] R. Prozorov, M. A. Tanatar, N. Ni, A. Kreyssig, S. Nandi, S. L. Bud'ko, A. I. Goldman, and P. C. Canfield. *Phys. Rev. B*, 80, Nov 2009.
- [67] *Statistical Physics, Part I*. Butterworth-Heinemann, Oxford, 1980.
- [68] T.-M. Chuang, M. P. Allan, J. Lee, Y. Xie, N. Ni, S. L. Bud'ko, G. S. Boebinger, P. C. Canfield, and J. C. Davis. Nematic Electronic Structure in the “Parent” State of the Iron-Based Superconductor $\text{Ca}(\text{Fe}_{1-x}\text{Co}_x)_2\text{As}_2$. *Science*, 327:181–, January 2010.
- [69] J. J. Ying, X. F. Wang, T. Wu, Z. J. Xiang, R. H. Liu, Y. J. Yan, A. F. Wang, M. Zhang, G. J. Ye, P. Cheng, J. P. Hu, and X. H. Chen. Measurements of the anisotropic in-plane resistivity of underdoped Fe-based pnictide superconductors. *Phys. Rev. Lett.*, 107:067001, Aug 2011.
- [70] E. C. Blomberg, M. A. Tanatar, R. M. Fernandes, B. Shen, H.-H. Wen, J. Schmalian, and R. Prozorov. Sign-reversal of the in-plane resistivity anisotropy in hole-doped iron pnictides. *ArXiv e-prints*, February 2012.
- [71] Rafael M. Fernandes, Elihu Abrahams, and Jörg Schmalian. Anisotropic in-plane resistivity in the nematic phase of the iron pnictides. *Phys. Rev. Lett.*, 107:217002, Nov 2011.
- [72] C.-C. Chen, J. Maciejko, A. P. Sorini, B. Moritz, R. R. P. Singh, and T. P. Devereaux. Orbital order and spontaneous orthorhombicity in iron pnictides. *Phys. Rev. B*, 82:100504, Sep 2010.
- [73] M. A. Tanatar, N. Ni, A. Thaler, S. L. Bud'ko, P. C. Canfield, and R. Prozorov. Pseudogap and its critical point in the heavily doped $\text{Ba}(\text{Fe}_{1-x}\text{Co}_x)_2\text{As}_2$ from c -axis resistivity measurements. *Phys. Rev. B*, 82:134528, Oct 2010.
- [74] M. Shayegan, K. Karrai, Y. P. Shkolnikov, K. Vakili, E. P. de Poortere, and S. Manus. Low-temperature, in situ tunable, uniaxial stress measurements in semiconductors using a piezoelectric actuator. *Applied Physics Letters*, 83:5235, December 2003.

- [75] A. Cano, M. Civelli, I. Eremin, and I. Paul. Interplay of magnetic and structural transitions in iron-based pnictide superconductors. *Phys. Rev. B*, 82:020408, Jul 2010.
- [76] R. M. Fernandes, L. H. VanBebber, S. Bhattacharya, P. Chandra, V. Keppens, D. Mandrus, M. A. McGuire, B. C. Sales, A. S. Sefat, and J. Schmalian. Effects of nematic fluctuations on the elastic properties of iron arsenide superconductors. *Phys. Rev. Lett.*, 105:157003, Oct 2010.
- [77] Khuong K. Huynh, Yoichi Tanabe, and Katsumi Tanigaki. Both Electron and Hole Dirac Cone States in $\text{Ba}(\text{FeAs})_2$ Confirmed by Magnetoresistance. *Phys. Rev. Lett.*, 106:217004, May 2011.
- [78] A. A. Abrikosov. *Sov. Phys. JETP*, 29:476, 1969.
- [79] A. A. Abrikosov. Quantum magnetoresistance. *Phys. Rev. B*, 58:2788–2794, Aug 1998.
- [80] A. A. Abrikosov. Quantum linear magnetoresistance. *EPL (Europhysics Letters)*, 49(6):789, 2000.
- [81] Ying Ran, Fa Wang, Hui Zhai, Ashvin Vishwanath, and Dung-Hai Lee. Nodal spin density wave and band topology of the FeAs-based materials. *Phys. Rev. B*, 79:014505, Jan 2009.
- [82] P. Richard, K. Nakayama, T. Sato, M. Neupane, Y.-M. Xu, J. H. Bowen, G. F. Chen, J. L. Luo, N. L. Wang, X. Dai, Z. Fang, H. Ding, and T. Takahashi. Observation of Dirac Cone Electronic Dispersion in BaFe_2As_2 . *Phys. Rev. Lett.*, 104:137001, Mar 2010.
- [83] Kazuma Nakamura, Ryotaro Arita, and Hiroaki Ikeda. First-principles calculation of transition-metal impurities in LaFeAsO . *Phys. Rev. B*, 83:144512, Apr 2011.
- [84] C. Liu, T. Kondo, R. M. Fernandes, A. D. Palczewski, E. D. Mun, N. Ni, A. N. Thaler, A. Bostwick, E. Rotenberg, J. Schmalian, S. L. Bud'Ko, P. C. Canfield,

- and A. Kaminski. Evidence for a Lifshitz transition in electron-doped iron arsenic superconductors at the onset of superconductivity. *Nature Physics*, 6:419–423, June 2010.
- [85] Chang Liu, A. D. Palczewski, R. S. Dhaka, Takeshi Kondo, R. M. Fernandes, E. D. Mun, H. Hodovanets, A. N. Thaler, J. Schmalian, S. L. Bud’ko, P. C. Canfield, and A. Kaminski. Importance of the Fermi-surface topology to the superconducting state of the electron-doped pnictide $\text{Ba}(\text{Fe}_{1-x}\text{Co}_x)_2\text{As}_2$. *Phys. Rev. B*, 84:020509, Jul 2011.
- [86] Marcin Matusiak, Zbigniew Bukowski, and Janusz Karpinski. Doping dependence of the Nernst effect in $\text{Eu}(\text{Fe}_{1-x}\text{Co}_x)_2\text{As}_2$: Departure from Dirac-fermion physics. *Phys. Rev. B*, 83:224505, Jun 2011.
- [87] James G. Analytis, Ross D. McDonald, Jiun-Haw Chu, Scott C. Riggs, Alimamy F. Bangura, Chris Kucharczyk, Michelle Johannes, and I. R. Fisher. Quantum oscillations in the parent pnictide BaFe_2As_2 : Itinerant electrons in the reconstructed state. *Phys. Rev. B*, 80:064507, Aug 2009.
- [88] Taichi Terashima, Nobuyuki Kurita, Megumi Tomita, Kunihiro Kihou, Chul-Ho Lee, Yasuhide Tomioka, Toshimitsu Ito, Akira Iyo, Hiroshi Eisaki, Tian Liang, Masamichi Nakajima, Shigeyuki Ishida, Shin-ichi Uchida, Hisatomo Harima, and Shinya Uji. Complete Fermi Surface in BaFe_2As_2 Observed via Shubnikov de Haas Oscillation Measurements on Detwinned Single Crystals. *Phys. Rev. Lett.*, 107:176402, Oct 2011.
- [89] J. Chang, Nicolas Doiron-Leyraud, Francis Laliberté, R. Daou, David LeBoeuf, B. J. Ramshaw, Ruixing Liang, D. A. Bonn, W. N. Hardy, Cyril Proust, I. Sheikin, K. Behnia, and Louis Taillefer. Nernst effect in the cuprate superconductor $\text{YBa}_2\text{Cu}_3\text{O}_y$: Broken rotational and translational symmetries. *Phys. Rev. B*, 84:014507, Jul 2011.
- [90] David LeBoeuf, Nicolas Doiron-Leyraud, B. Vignolle, Mike Sutherland, B. J. Ramshaw, J. Levallois, R. Daou, Francis Laliberté, Olivier Cyr-Choinière, Johan

Chang, Y. J. Jo, L. Balicas, Ruixing Liang, D. A. Bonn, W. N. Hardy, Cyril Proust, and Louis Taillefer. Lifshitz critical point in the cuprate superconductor $\text{YBa}_2\text{Cu}_3\text{O}_y$ from high-field Hall effect measurements. *Phys. Rev. B*, 83:054506, Feb 2011.